



**HAL**  
open science

## 2D and 3D visualization of acoustic waves by optical feedback interferometry

Patricio Fernando Urgiles Ortiz

► **To cite this version:**

Patricio Fernando Urgiles Ortiz. 2D and 3D visualization of acoustic waves by optical feedback interferometry. Optics / Photonics. Institut National Polytechnique de Toulouse - INPT, 2019. English. NNT : 2019INPT0094 . tel-02442503

**HAL Id: tel-02442503**

**<https://laas.hal.science/tel-02442503>**

Submitted on 16 Jan 2020

**HAL** is a multi-disciplinary open access archive for the deposit and dissemination of scientific research documents, whether they are published or not. The documents may come from teaching and research institutions in France or abroad, or from public or private research centers.

L'archive ouverte pluridisciplinaire **HAL**, est destinée au dépôt et à la diffusion de documents scientifiques de niveau recherche, publiés ou non, émanant des établissements d'enseignement et de recherche français ou étrangers, des laboratoires publics ou privés.



# THÈSE

## En vue de l'obtention du **DOCTORAT DE L'UNIVERSITÉ DE TOULOUSE**

Délivré par l'Institut National Polytechnique de Toulouse

---

Présentée et soutenue par  
**Patricio URGILES ORTIZ**

Le 5 novembre 2019

**Visualisation 2D et 3D des ondes acoustiques par interférométrie  
à réinjection optique**

---

Ecole doctorale : **GEET - Génie Electrique Electronique et Télécommunications :  
du système au nanosystème**

Spécialité : **Photonique et Systèmes Optoélectronique**

Unité de recherche :  
**LAAS - Laboratoire d'Analyse et d'Architecture des Systèmes**

Thèse dirigée par  
**Thierry BOSCH et Julien PERCHOUX**

Jury

**M. Pascal PICART**, Rapporteur  
**M. Sébastien GUENNEAU**, Rapporteur  
**Mme Sandrine BERNARDINI**, Examinatrice  
**M. Thierry BOSCH**, Directeur de thèse  
**M. Julien PERCHOUX**, Co-directeur de thèse



# Dedication

*To my wife Clarita and my children Joaquín, Benjamín without them, this thesis would not have been completed. And to my mother Susana to my father Manuel, my brother Ricky, P. Marcelo and my sisters Diana and Jenny my family*



# Acknowledgments

*My sincere thanks to the Universidad Politécnica Salesiana, and to Instituto de Fomento al Talento Humano (IFTH) of Ecuador, for their support to carry out the Doctorate studies. To my friends from the OSE group now OASIS group, especially Julien, to LAAS- CNRS and my friends from Toulouse.*



# Resume

Studying and understanding the phenomenon of acoustic waves has been a great challenge for researchers whose beginnings are shown in chapter one started with a historical recount of 2700 years before Christ until today, for which different methods have been developed to perform the measurement of small variations in air pressure when altered by a mechanical wave produced by a sound source, being the discovery more recognized at the moment by Ciddor and Reginald R. Hill whose discovery on the index of refraction of the air were published in different articles and accepted by Birmingham International Geodesy Association (IAG). All the information developed was presented in data analyzed in one dimension, which did not allow an adequate understanding of the propagation of the acoustic field in space, so that methods for obtaining images in 2 dimensions of sound were developed, which helps understand the spatial characteristics of a field, material and environment. Among the most used methods are the Schlieren method, Shadowgraph method, arrangements of microphones (acoustic chambers) and in this thesis we finished with an analysis of the laser Doppler vibrometry method. Thus, the method that obtains a high spatial resolution is the one used by a microphone array, this method is very useful, except for the dispersion of the wave due to the presence of the instruments in the field of measurement. Therefore the optical method overcome these problems due to its non-contact nature. In chapter two we can find a theoretical explanation about the technique based on the feedback of optical interferometry (OFI) describing the model of Fabry - Perot applying the model of three mirrors, with its formal equations of Lang and Kobayashi in which the parameter of feedback  $C$  an important role in the behavior of the laser under reinjection. With this information obtained by the OFI system, a system has been designed to acquire the signals of the propagation of an acoustic field in a point, a dimension and two dimensions. Obtaining images with variation of acoustic pressure over time and an image of acoustic pressure behavior in space. For chapter three, the tomography technique has been applied to obtain the third dimension, so that a visualization of the acoustic field in three dimensions  $f(x, y, z)$  is achieved. If you plan on time as another dimension you can see a function that represents the propagation of the acoustic field in four dimensions  $f(x, y, z, t)$ .



# Contents

<b>Dedicatoria</b>	<b>II</b>
<b>Acknowledgments</b>	<b>IV</b>
<b>Resume</b>	<b>VI</b>
<b>Introduction</b>	<b>XI</b>
<b>1 Sound field visualization</b>	<b>13</b>
1.1 Brief history of the sound . . . . .	13
1.2 Physical principles of sound . . . . .	16
1.2.1 Acoustic Pressure, Particle speed, Acoustic intensity and Acoustic power . . . . .	17
1.2.2 Definitions of the sound field . . . . .	20
1.3 Microphone based imaging of pressure waves . . . . .	21
1.4 Refractive index imaging Systems . . . . .	23
1.4.1 The interaction between sound and light . . . . .	23
1.4.2 Schlieren imaging Systems . . . . .	24
1.4.3 Shadowgraphy . . . . .	28
1.4.4 Applications of the schlieren method for acoustic images .	30
1.5 Laser Doppler vibrometer (LDV) . . . . .	32
1.5.1 Principle of LDV . . . . .	32
1.5.2 Sound field measurements using laser vibrometry . . . . .	34
1.5.3 Acoustic imaging by LDV . . . . .	35
1.6 Conclusion . . . . .	40
<b>2 Acoustic Imaging using Optical Feedback Interferometry</b>	<b>41</b>
2.1 Theory of Optical Feedback Inteferometry for opto-acoustic sensing	41
2.1.1 Laser oscillation conditions in free running state . . . . .	41
2.1.2 The laser diode under optical feedback . . . . .	43
2.1.3 Measuring changes of refractive index in the external cavity	48
2.1.4 Modeling the projection of the pressure wave in a 2D plane	49
2.2 Experimental setup for imaging acoustic pressure waves . . . . .	53
2.2.1 Design of the acoustic optical feedback interferometry setup for one point . . . . .	53

2.2.2	Acquisition of signal in one point . . . . .	54
2.2.3	Producing images of acoustic pressure waves . . . . .	56
2.3	Characterization of the radiation pattern of acoustic sources . . .	57
2.4	Characterization of the source along its propagation axis (1D) . .	59
2.4.1	Imaging acoustic propagation in two Dimension . . . . .	60
2.4.2	Estimation of the location of an Acoustic Source . . . . .	63
<b>3</b>	<b>Acoustic Tomography Imaging using Optical Feedback Interferometry</b>	<b>65</b>
3.1	Introduction . . . . .	65
3.2	Analytical Methods for Image Reconstruction in Computing Tomography . . . . .	66
3.2.1	Computation of 2D layers . . . . .	67
3.2.2	Sinogram . . . . .	69
3.3	Backprojection . . . . .	69
3.3.1	Algebraic Reconstruction Technique (ART) . . . . .	70
3.4	Setup Design . . . . .	71
3.4.1	Backprojection Reconstruction . . . . .	77
3.4.2	Backprojection Reconstruction by Matlab . . . . .	80
3.5	Acoustic tomography imaging experimentation . . . . .	82
3.5.1	Acoustic 3D imaging of a unique source . . . . .	82
3.5.2	Interferences . . . . .	86
3.5.3	Stationnary wave . . . . .	91
3.5.4	Focused wave with an acoustic concave mirror . . . . .	93
3.5.5	Huygens-Fresnel principle in acoustics . . . . .	96
3.6	Resume . . . . .	102
	<b>Conclusion</b>	<b>103</b>
	<b>Recomendaciones</b>	<b>106</b>
	<b>Bibliography</b>	<b>110</b>
	<b>A Radon Transform Properties</b>	<b>119</b>
	<b>B Publishers</b>	<b>121</b>

# Introduction

The visualization of pressure waves is a subject of major interest that researchers seek to solve for several centuries now. However, while the acoustics have been developed with a solid base in the early ages of modern physics, the optics did not have the similar solid knowledge until Maxwell's equation was revealed and later with the quantum physics that have led to the invention of lasers. Using optics to observe acoustic phenomena requires a strong interaction between the two types of waves that is achieved by the acousto-optic effect as it links the refractive index of a transparent medium to the molecular density and then to the local pressure. Thus sound will directly impact the velocity of light in the medium where it propagates, but it will also impact the light propagation direction or the phase of the electric field of the light wave. Interferometric systems in the optical domain are well fitted to address acoustic sensing as they are by nature sensitive to the phase information of the light wave.

The objective of this thesis is to investigate, develop and experiment a method to visualize acoustic waves that is based on the Optical Feedback Interferometry (OFI) which is possibly the simplest possible interferometric arrangement as it is reduced to the laser source cavity where the light source is generated but also where the interference occurs and where it is detected. The sensor system developed in this work at first to measure pressure changes at a single point, is then extended for observation of acoustic phenomena in two dimensions and eventually in three dimension using a tomographic inspired reconstruction method. Through measurements we have shown that the measurement system not only allows visualization of the propagation of a pressure wave, but that it can be extended to the determination of some parameters of the pressure waves such as the location of its origin or to a focus point when focalized.

In chapter 1, a brief history of the sound is made that pursue to discuss the works that are focused on measuring the refractive index in media that are altered by an acoustic wave. Then a brief description of the fundamental characteristics of the acoustic waves is made in order to set the definition of sound parameters. An analysis of the different visualization methods for sound fields is proposed. Among these methods, we have focused on: the microphone arrangements, which are the more traditional method to observe pressure waves in acoustics; schlieren imaging and shadowgraphy a quite ancient method that was developed with the photography; Laser Doppler Vibrometry (LDV) systems

which are the closest to the OFI system that is the subject of this PhD thesis.

Chapter 2 presents the fundamentals of the optical feedback effect in the case where the laser light interacts with the variation of the refractive index of the transparent medium in the external cavity. A derivation of the equations details the physics that supports the phenomenon. The rate equations that constitute the theory of lasers subject to external feedback are analyzed to develop a simple system that senses the variation of the refractive index. An experimental system based on an external mirror set at a fixed distance was designed to acquire the refractive index variation. It was then extended, first to realize a system which perform the characterization of acoustic source radiation pattern, then in a second time to perform 2D images of pressure waves.

In Chapter 3, we present a methodology to perform 3D images of acoustic waves. The processing methods that is based on the computed tomography technique is ruled by the inverse Radon transform. We present an experimental setup that is capable to acquire the data that will be processed to produce 3D images. This setup is then tested for different acoustic configurations with one, two and seven acoustic sources, producing various acoustic waves interferences. We have tested the capabilities of the OFI technique to acquire, measure and visualize acoustic waves. We demonstrate in this way that OFI is a suitable technique to be implemented in the measurements of variations of the refractive index with reasonable resolution. The results obtained presented in the third chapter clearly emphasize the possibilities that the OFI system presents as a new simple optical technique for sound visualization and wave characterization, becoming a powerful method of non-intrusive observation of acoustic phenomena.

# Chapter 1

## Sound field visualization

The visualization of physical phenomena is one of the challenges that researchers try to perform by the design and the implementation of different sensors providing an information close to reality through changes in the values of physical available parameters. The acquisition, processing and visualization of the variations of physical phenomena always provided a better understanding of the problem under study, and throughout history human beings have been developing visualization systems as for example with the development of photography since 1880 in which the cameras, and what they capture, changed our perception of the world and of ourselves forever.

A variety of methods to understand sound propagation through a visual representation or image have been developed for more than 300 years. Scientists have sought to visualize an audible phenomenon in particular, to develop a visual representation of sound waves helping understanding the phenomenon [1]. The common method uses transducers capable of detecting the two fundamental components that are the acoustic pressure and the particle medium velocity, or in other words, the kinetic energy and the potential. There is a close relationship between the vectors that carry directional information of particle velocity (*id est* kinetic energy) and the scalar magnitudes of sound pressure and potential energy. These quantities provide information about the physical phenomenon evaluated in a given position, and a representation of the distribution of the acoustic field in space is achieved by means of a map of levels.

In this chapter we will discuss the nature of the sound and then present the main methods of visualization of the acoustic field that are: arrays of microphones, the schlieren and shadowgraph method, and laser visualization doppler vibrometer .

### 1.1 Brief history of the sound

Pythagoras (570-497 BC) observed that the movement of air generated by a vibrating body that sounds a single musical note is also vibratory and of the

same frequency as the body. Aristotle (384-322 BC) stated that vibrating objects emitted sounds, and these vibrations hit the air around it and make it vibrate which in turn makes the surrounding air to vibrate and so on. Vitruvius (90-20 BC) explained that true sound waves travel in a three-dimensional world not as circles, but rather as spherical waves that extend outward from the source.

Leonardo da Vinci (1452-1519) mentions that if there is no percussion or movement of air there can be no sound, in his experiments he correlated the waves generated by a stone thrown into the water with sound waves as similar phenomena. Marin Mersenne (1588-1648), French philosopher of the community of Franciscan friars, made the first scientific description of an audible frequency of 84 Hz, his publication is entitled "En Harmonie universelle".

Pierre Gassendi (1582-1655), tried to demonstrate that the speed of sound was independent of tone. Robert Boyle (1626-1691) assisted by Robert Hooke (1635-1703) showed that air as a medium is necessary for the production and propagation of sound. Joseph Sauveur (1653-1713), proposes the term acoustic (sound in Greek) for the science that studies sound. He additionally defined the following terms: fundamental, harmonics, node and ventral segment. Narciso Marsh (1683), bishop of Ferns and Leighlin, used the term "acoustics" to define direct sound differentiating it from the sound produced by a reflection or a diffraction. Franciscus Mario Grimaldi (1613-1663) published his experimental diffraction studies, which were used for both acoustics and light. Isaac Newton (1642-1726) and Gottfried W. Leibniz (1646-1716), developed a series of experimental measurements including the theoretical derivation of Newton's sound velocity. Hooke (1678) announced his law about deformation, which was the basis of theories of vibration and elasticity. Christiaan Huygens (1690), Dutch astronomer, physicist and mathematician, presented his works entitled "Treatise of light" giving a complete explanation of the phenomena of light and sound, finding a close relationship between these two phenomena. Count Giovanni L. Bianconi (1717-1781) of Bologna and Charles M. de la Condamine (1701-1773) discovered the influence of temperature on the speed of sound. Ernst Florens Friedrich Chladni (1756-1827), German physicist and musician, was able to make the measurements of the speed of sound through a method based on torsional vibrations and with the help of vibrating rods and resonant tubes.

Thomas Young (1773-1829) and Augustin Jean Fresnel (1788-1817) independently explained the principle of interference.

Lord Rayleigh (1842-1919) presents his work on modern acoustics, whose research is included in his work "The theory of sound" in two volumes, being a new procedure for measurements of acoustic vibrations.

In 1916, Langevin and Chilowsky echoed the bottom of the ocean and a shield plate at a depth of 200 m. Reginald A. Fessenden (1866-1932), developed a mobile coil that operates at frequencies in the range of 500-1000 Hz which is a transducer that generate signals underwater.

In 1922 Leon Brillouin French physicist was the first person to observe the interaction between light and sound [2]. Debye and Sears in America and independently Lucas and Biquard in France measured the diffraction patterns of

light driven by high frequency sound waves [3, 4]. Between 1935 and 1936 Raman and Nath proposed a general model to describe the diffraction of light using ultrasonic waves capable of determining the angle and intensity, when the incident light was normal or oblique to the acoustic waves [5]-[9]. In 1939 H. Barrell and J. E. Sears presents a breakthrough in the accuracy of the determination of refractive indices of air. The work was the basis for other investigations in this field. Currently, Barrell and Sears equations are widely used [10].

In 1953 B. Edlén evaluated several experiments by different authors, including Barrell and JE Sears and in 1966 Edlén published the dispersion equation for standard air [11], analyzing the dependence of refractive index of air under atmospheric conditions and using the Lorenz-Lorentz air density equations, these equations are used in geodesy and metrology. In 1963, at Berkeley, the resolution of the International Union of Geodesy and Geodynamics IUGG recommended the procedures of Barrell and J. E. Sears and Edlén. IUGG also introduced the simplified Barrell-Sears procedure equations. In 1967 the year after the publication of Edlén, Owens published an article [12], in which he examined the dependence of the refractive index on air density. Achieving better results with high temperatures and humidity.

In 1972, Peck and Reader carried out in its research work the measurement of 8 different wavelengths in the infrared spectrum and discovered in its experimentation some differences with the formula of Edlén of 1966 and error in the data of Peck and Khanna that Edlén used. In this year the dispersion equation was published which was valid for a very wide range of 230-1690 nm wavelength [13]. The simplified two-term dispersion formula looks as:

$$(n - 1) \cdot 10^8 = \frac{5791817}{238.0185 - \sigma^2} + \frac{167909}{57.362 - \sigma^2} \quad (1.1)$$

where:  $\sigma$  is the wavenumber computed as  $\sigma = 1/\lambda$ .

In 1993, Birch and Downs presented a new formula for air density, the refractivity of water vapors, the change in CO<sub>2</sub> concentration and also the change in the temperature scale, thus questioning the Edlén equations [14].

The limitations in the uncertainties of pressure, temperature and humidity measurement, etc. . . result in 3  $\sigma$  of uncertainty of  $\pm 3 \times 10^{-8}$  for the revision of the Edlén equation. However, when the equation is used in practice, the total uncertainty associated with the calculated value of the air refractive index could be increased to approximately  $\pm 1 \times 10^{-7}$ .

In 1999, the Birmingham International Geodesy Association (IAG) published a resolution regarding the refractive index of air, correcting the 1963 equations recommended by IUGG for standard geodetic purposes up to 1 ppm:

In 1996, 1999 and 2002 E. Ciddor and Reginald R. Hill, published a series of articles [15]-[17] that dealt with the refractive index of the phase. Their 1999 paper was an update of 1996 with small modifications while in 2002, additional research on CO<sub>2</sub> and dispersion equations are presented, although the authors did not observe significant effects on their results, with differences lower than  $3 \cdot 10^{-9}$ .

Given the complexity of the set of equations developed by Ciddor and Hill, a matlab code has been developed and published [18] with which the air pressure and the refractive index have been simulated as shown in the figure 1.1.

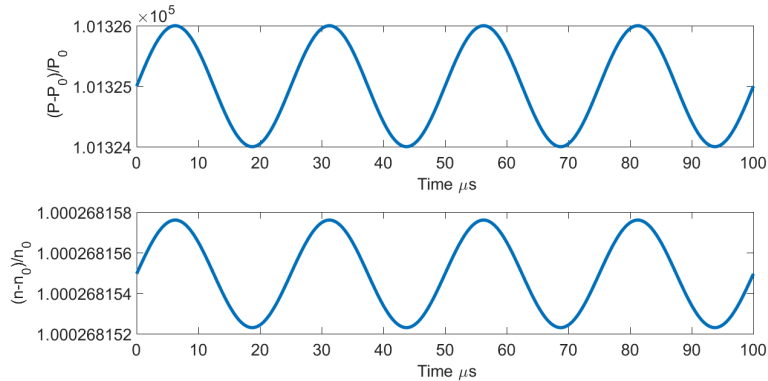


Figure 1.1: Refractive index simulated

Simulation of the refractive index (bottom figure) using Muelaner implementation of Ciddor equations for a sinusoidal modulation of the pressure the air pressure (top figure) with  $(P - P_0)/P_0$  with  $P_0$  being  $1.013 \cdot 10^5$  Pa and  $(n - n_0)/n_0$  with  $n_0$  the first value on vertical axis (bottom figure)

## 1.2 Physical principles of sound

Sound is a form of energy whose wave propagates as a vibration of the molecules (or particles) that constitute the medium around their positions of equilibrium (or state of rest). Under small variations of pressure (acoustic pressure) collision of the molecules (or particles) leads to the transmission of the deformation induced by this micro-displacement.

The molecules return to their original resting position, once the disturbance has ceased, so that it could be said that the sound is a propagation of energy in a material medium without transport of matter. Thus to propagate an acoustic wave, a medium such as air, water, etc., whose particles have a liberty of movement in the propagation direction while the waves are of the longitudinal type. Therefore the sound can not propagate in a vacuum.

However, when the sound propagates in solid elements, shear forces arise due to the microscopic structure of these elements, producing transverse waves that are added to the longitudinal waves.



Figure 1.2: (a)longitudinal waves (b)Transverse waves

When the acoustic field evolves in a homogeneous, isotropic and unobstructed medium, the wave of an ideal source propagates identically in all directions as a spherical wave.

However, when the distance from the sound source to the receiver is large regarding the dimension of the receiver, the acoustic wave is considered as a flat wave.

### 1.2.1 Acoustic Pressure, Particle speed, Acoustic intensity and Acoustic power

#### Acoustic pressure

Sound pressure is defined as the fluctuations, above or below the normal or static value of medium pressure, which occur when a sound wave propagates through it. The human ear is capable of detecting sounds whose amplitude is between a minimum of 20  $\mu\text{Pa}$ , and a maximum of about 20 Pa, where the pain threshold is located. While defining the static pressure as  $P_0$  we have:

$$P_{\text{total}} = P_0 + p(t), \quad (1.2)$$

where:  $p(t)$  is the acoustic pressure which is sensed by our ears.

$$p(t) = P_{\text{max}} \cos(\omega t + \varphi) \quad (1.3)$$

with  $\omega = 2\pi f$  is the angular frequency

The magnitude of  $P_0$  and  $p(t)$  are very different, under conventional atmospheric conditions the static pressure  $P_0$  is equal to 1013 hPa, while fluctuations acoustics rarely exceeds a few tens of Pa. The effective pressure  $p_{\text{eff}}$  between two instant  $t_1$  and  $t_2$  is defined by:

$$p_{\text{eff}}^2 = \frac{1}{t_2 - t_1} \int_{t_1}^{t_2} p^2(t) dt \quad (1.4)$$

The effective pressure for the case of a purely monochromatic sound (a single frequency) is

$$p_{\text{rms}} = \frac{P_{\text{max}}}{\sqrt{2}} \quad (1.5)$$

According to the International System of Units, the density of the sound propagation medium,  $\rho$ , is equal to the mass per unit volume of the medium in  $\text{kg/m}^3$ . The air density at standard temperature and pressure (20°C and 1 atm)  $\rho_0$  is approximately  $1.21 \text{ kg/m}^3$ . The density of the gases increases when the pressure increases and decreases when the temperature increases.

### The speed of sound

The speed of sound, usually indicated as  $c_s$ , depends on the medium of propagation, as well as the state of the medium. In the case where a sound propagates in a perfect gas, its velocity will depend on its molar mass  $M$  and its temperature  $T$ :

$$c_s = \sqrt{\frac{\gamma RT}{M}}, \quad (1.6)$$

where  $\gamma = C_p / C_v$  is the heat-capacity ratio for the perfect gas at constant pressure ( $C_p$ ) to heat capacity at constant volume ( $C_v$ ), and the universal constant of perfect gases  $R = 8.315 \text{ J}\cdot\text{K}^{-1}\cdot\text{mol}^{-1}$ . The speed of sound propagation,  $c_s$ , the frequency  $f$ , and the wavelength  $\Lambda$ , are related by the following equation:

$$c_s = f \cdot \Lambda \quad (1.7)$$

The propagation speed of sound  $c_s$  in air is 343 m/s, at 20°C and 1 atm. At other temperatures it can be calculated using:

$$c_s = 332 + 0.6T_c \quad (1.8)$$

where  $T_c$  is the temperature expressed in Celsius.

### The acoustic intensity

The acoustic intensity is the acoustic energy that passes through a unit of surface per unit of time:  $\text{W/m}^2$ . In general, it is defined in a given direction.

$$\vec{I} = p \cdot \vec{u} \quad (1.9)$$

In a free-field environment, *id est* without reflected sound waves and away from any another disturbance, the sound intensity is related to the quadratic mean square acoustic pressure as in (1.10).

$$\vec{I} = \frac{p_{\text{rms}}^2}{\rho c_s} \quad (1.10)$$

with  $\rho$  the density of air ( $\text{kg/m}^3$ ) and  $c_s$  the speed of sound (m/s).

The quantity,  $\rho c_s$  is the "acoustic impedance" and is equal to  $414 \text{ N}\cdot\text{s/m}^3$  at 20°C and 1 atm.

### The acoustic power

The acoustic power  $W_s$  is obtained by integrating the sound intensity of an imaginary surface surrounding a source. Therefore the power, radiated by an acoustic source is:

$$W_s = \int_S (\vec{I} \cdot \vec{n}) dS, \quad (1.11)$$

where  $\vec{n}$  is the normal vector to the surface.

For a sound source that produces uniformly spherical waves (or that radiate in all directions), the most convenient way to calculate  $W_s$  is 1.11:

$$W_s = 4\pi r^2 I, \quad (1.12)$$

where  $r$  is the distance from the source.

### Sound pressure level (SPL)

The range of sound pressures that the human ear can hear is wide. The minimum audible sound pressure for the young human ear that is considered healthy and immaculate from excessive exposure to excessively loud music is approximately  $20 \cdot 10^{-6}$  Pa.

A sound wave with a frequency of 40 Hz is at the limit of the minimum audible level due to molecular motion. At this frequency the sound pressure level will be affected by the thermal noise due to the movement of the molecules in air. In normal human hearing, pain is experienced with sound pressures of the order of 60 Pa or  $6 \cdot 10^{-4}$  atm.

A linear scale for sound pressure would require  $10^{13}$  unit divisions to cover the range of human audition so a logarithm scale is used, and the sound pressure level  $L_p$  [19] in decibel (dB) is defined with regard to a pressure of reference  $p_{\text{ref}}$  as:

$$L_p = 10 \log_{10} \left( \frac{p_{\text{rms}}^2}{p_{\text{ref}}^2} \right) \quad (1.13)$$

The reference pressure corresponds to the lowest sound pressure that can be detected by the young normal ear. The acoustic pressure value is a measured according to international regulation in rms with  $p_{\text{ref}} = 2 \cdot 10^{-5}$  N·m<sup>-2</sup> that corresponds to 20 μPa [20].

### Sound Intensity Level

The sound intensity level,  $L_I$ , can be defined similarly to the SPL in dB as:

$$L_I = 10 \log_{10} \frac{I}{I_{\text{ref}}} \quad (1.14)$$

where  $I_{\text{ref}}$  is an internationally agreed reference intensity of  $10^{-12}$  W/m<sup>2</sup>. The relationship between the acoustic intensity and the pressure in the far field of a source is:

$$L_I = L_p + 10 \log_{10} \frac{100}{\rho c_s} = L_p + 26 - 10 \log_{10}(\rho c_s) \quad (1.15)$$

The values at 1 atm and 20°C of the characteristic impedance  $\rho c_s$  is 414 kg·m<sup>-2</sup>·s<sup>-1</sup> so that

$$L_I = L_p - 0.2 \quad (1.16)$$

### Sound Power Level

The sound power level,  $L_w$  (or PWL), can be expressed as

$$L_w = 10 \log_{10} \frac{W}{W_{\text{ref}}} \quad (1.17)$$

Where the reference power  $W_{\text{ref}}$  is  $10^{-12}$  W.

## 1.2.2 Definitions of the sound field

### Near and Far field

In the region near a sound source there is a particular phenomenon in which sound waves have a complex behavior without a fixed relationship between pressure and distance. In this region the acoustic pressure and the speed of the acoustic particle are not in phase and the energy of the sound circulates back and forth with the vibrating surface of the source, without escaping or propagating.

The extension of the near field region where these interferences occur is determined by the ratio of the oscillator diameter  $D$  to its wavelength  $\Lambda$ .

$$z = \frac{D^2 - \Lambda^2}{4\Lambda} \quad (1.18)$$

In most practical cases the diameter is much larger than the wavelength and we can simplify as:

$$z \approx \frac{D^2}{4\Lambda} = N \quad (1.19)$$

$N$  is called the near-field length, and is an important characteristic of the sound field, since most of the experiments and simulations are conducted in the far field region where the acoustic wave have a well-defined behavior.

### Direct field

The direct field of a sound source is defined as the part of the sound field that has not suffered any reflection of any surface or obstacle in the propagation region.

## Reverberant field

The reverberant field of a source is defined as the part of the sound field radiated by a source that has experienced at least one reflection from an obstacle.

### 1.3 Microphone based imaging of pressure waves

The most traditional method to measure pressure waves remains the one that uses mechanical microphones. It is simply based on the detection of the displacement of membranes that are subject to pressure fluctuations. The detection of the membrane vibration can be done by inductive, capacitive, piezo-electricity based or even optical methods. By default, it is a localized measurement but well-established techniques can be used to reconstruct the image of the wave that propagates.

The principle of the reconstruction requires a minimum of 4 microphones which location in the network of microphones is perfectly known and for each of them, the amplitude and the phase of the detected pressure variations is recorded. Thus, depending on the geometry of the microphone array, processing algorithms are developed which in most of the cases are designed to locate individual sound sources and estimate their emitted SPL.

At the end of the 80's, AT & T Bell Lab carried out several experiments applying a great variety of microphones in their designs [21].

The design started with a matrix of microphones arranged in 9 columns and 7 rows in an area of 1 square meter, the second system included 400 microphones [22] and was implemented in an auditorium for the capture of directional audio to support remote conferences in conditions of noise and reverberation. The matrix consisting of 512 microphones was designed by the Brown University [23], by the group of Laboratories for Human / Machine Engineers (LEMS) and was called Huge Microphone Array (HMA).

Meanwhile a matrix with 1020 microphones was built by the Massachusetts Institute of Technology (MIT), this project called the Large Academic Data Set (LOUD, for its acronym in English) of the Laboratory of Artificial Intelligence and Computer Science (CSAIL, for its acronym in Spanish). English) holds the world record for the largest number of microphones in a single matrix [24]. The LOUD design consisted of a series of rectangular panels of microphones 180 cm wide and 50 cm high.



Figure 1.3: LOUD 1020-node microphone array.[24]

The imaging of acoustic wave based on localized microphone has then taken a great advantage in using Micro-Electro-Mechanical Systems (MEMs) to replace the traditional microphones. As compared to the traditional microphone, the MEMs provide higher compactness and accuracy in the phase detection (see for example Fig. 1.4 [25]).



Figure 1.4: MEMS array board.[25]

Thanks to the high resolution image they can provide, the array of MEMs are nowadays the standard in use both in research institution and in industrial

applications [26]-[30]. Nevertheless, they remain intrusive methods and the high resolution comes with a high number of microphones and thus with an important cost. In these conditions, non-intrusive methods such as optical sensing may be of great interest in certain applications.

## 1.4 Refractive index imaging Systems

### 1.4.1 The interaction between sound and light

Sir William Henry Bragg and Sir William Lawrence Bragg demonstrated that diffraction patterns could be explained by means of the so-called Bragg law that was formulated for the study of x-rays in 1913 [31] linking the light and sound for certain angles of incidence. Between 1935 and 1936 Raman and Nath proposed a general model to describe the diffraction of light by ultrasonic waves [5]-[9],[32]. With the advent of laser technology in the 1950s, several studies reviewed the acousto-optic effect in the high frequency ultrasonic range [33]-[35].

The existence of an interaction between light and pressure was predicted by Brillouin [36] in 1922. Experimental verification followed in 1932, by Lucas and Biquard [37] in France, and Debye and Sears [38] in the USA. The original theory predicted a phenomenon similar to the X-ray diffraction in crystals where, in the latter, the atomic planes cause multiple reflections of an incident electromagnetic plane wave. These reflections constructively interfere for certain critical angles of incidence, thus causing a general reflection. In acoustic, the role of the atomic planes is assumed by the compression and rarefaction planes.

For a propagating acoustic wave, in the regions where the medium is compressed the density is higher and so is the refractive index while where the medium is dispersed, its density and the refractive index are lower.

The refractive index variations caused by the acousto-optic effect correspond to the product of the piezo-optic coefficient multiplied by the acoustic pressure, and this product is much larger in water than in air. The typical ultrasonic pressures in underwater measurements range from a few kilopascals to a few megapascals, while in the air they are usually below a few hundred pascals.

Since optical frequencies are much greater than acoustic frequencies, the variations of the refractive index in a medium perturbed by sound are usually very slow in comparison with an optical period. There are therefore two significantly different time scales for light and sound. Therefore, an adiabatic approach can be used in which the problem of optical propagation is solved separately at each instant of time during the relatively slow cycle of the acoustic cycle, always treating the material as if it were a non-homogeneous static medium (frozen). In this quasi-stationary approximation, the acousto-optic, becomes the optics of an inhomogeneous medium (usually periodic) controlled by sound.

The change of the refractive index is proportional to the square root of the acoustic intensity.

$$\Delta n_0 = \sqrt{1/2MI_s}, \quad (1.20)$$

where  $M = (\vartheta^2 n^6)/(\zeta c_s^3)$  is a parameter of the medium that represents the effectiveness of sound in altering the refractive index, with  $\vartheta$  the mass density of the medium, and  $\zeta$  the photoelastic constant (or strain-optic coefficient).

The simplest form of interaction of light and sound is the partial reflection of an optical wave by the stratified parallel planes that represent the variations of the refractive index created by an acoustic plane wave (see Fig. 1.5) thus possibly resulting in a Bragg diffraction effect.

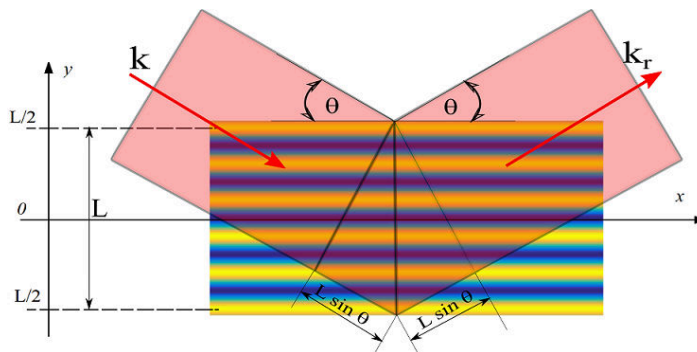


Figure 1.5: Reflections in homogeneous medium

### 1.4.2 Schlieren imaging Systems

The schlieren imaging system has been widely used to image fluid flows but its principle is efficient also in acoustic studies. The word schlieren is derived from the german word *schliere* and refers to the stripe appearance of the fluid flow that is shown through the schlieren imaging system [39, 40]. Schlieren's rudimentary techniques have been implemented for much longer than scientists have cited, before being used as a fluid dynamics tool, they have also been applied to optical components in telescopes and microscopes. This method allows a dynamic and direct visualization of the phenomenon and its analysis is based on qualitative visual studies [41]. It has been initially carried out initially by Hooke, Huygens and Foucault [40].

During the 20th century, techniques proposed by Toepler and Schardin in the study of aircraft shock waves, the mixture of liquids and gases and color filters were implemented to obtain quantifiable data [42]-[45].

Currently, the development of new digital cameras and computers with high performances has allowed the possibility of quantifying and qualifying the investigations that determine the field density through integrations of gradient measurements in the field [42]. This Schlieren image processing method relieve the problem of focus discrepancies and allows encoding spatial and angular information [46] which allows operation in fields such as biology, physics and environmental engineering [47, 48].

The schlieren image are result of Snell's law, which states that light slows

down after interaction with matter. The light that travels in homogeneous media at a constant speed and direction then meet with inhomogeneous media (like fluids in movement, pressure waves,...) where the light rays are refracted and deviate from their initial trajectory.

The method is based the observation of the intensity pattern of light obtained on a screen or a camera sensor that is determined by the Lorentz-Lorenz formula:

$$\frac{n^2 - 1}{\rho(n^2 + 2)} = \text{constant} \quad (1.21)$$

where:

$n$  is the refractive index

$\rho$  the density

If the analysis is carried out in gases, the value of the refractive index is close to unity, while the density of the pure fluids will depend on the pressure and temperature. In some applications involving gases, the pressure is substantially constant and the density changes with temperature. It is known that liquids such as water are practically incompressible and their density will vary only with temperature. this variation can be considered linear only in certain limits. it is so that the refractive index will scale linearly with the temperature. For a process that involves mass transfer, the Lorentz-Lorenz applied formula in a solute-solvent system takes the form:

$$\frac{n^2 - 1}{n^2 + 2} = \frac{4}{3}\pi(\alpha_A N_A + \alpha_B N_B) \quad (1.22)$$

Where:

$n$  is the refractive index of the solution.

$\alpha$  and  $N$  are respectively the polarizability and the mole fraction.

The path of the light beam in a medium whose refractive index varies in the vertical direction  $y$ -axis Consider two wave fronts sometimes  $\tau$  and  $\tau + \delta\tau$ , separated by a small time difference  $\delta\tau$ . At time  $\tau$  the ray is in a position  $z$ . After an interval  $\delta\tau$ , the light has moved a distance of  $\delta\tau$  times the speed of light  $c$ . Since  $c$  depends on the refractive index, it is a function of  $y$ . In addition, the wave front rotates at an angle  $\delta\alpha$ . The local light velocity is  $c_0 / n$ , where  $c_0$  is the speed of light in vacuum and  $n$  is the local refractive index of the medium. Therefore, the distance  $\delta z$  that the light beam travels during the time interval  $\delta\tau$  is:

$$\delta z = \delta\tau \frac{C_0}{n} \quad (1.23)$$

The gradient in the refractive index "n" along the "z" axis results in the flexing of the wavefront.  $\delta\alpha$  represents the angle of inclination at a location on the z-axis, a small increase  $\delta\alpha$  at the angle  $\alpha$  can be expressed as

$$\delta\alpha \approx \tan(\delta\alpha) = \frac{\delta^2 z}{\delta y} \quad (1.24)$$

Therefore, the accumulated angle through which the light beam has rotated over the length  $L$  of the test region is

$$\alpha = \int_0^L \frac{\partial(\ln(n))}{\partial y} \quad (1.25)$$

where the integration is made over the entire length of the test section. The angle  $\alpha$  being a function of the x and y coordinates, to the plane output of the test cell. If the refractive index within the test section is different from ambient air ( $n_a$ ), the angle  $\alpha''$  of the light beam emerging from the test cell is given by Snell's law

$$n_a \sin\alpha'' = n \sin\alpha \quad (1.26)$$

Assuming  $\alpha$  and  $\alpha''$  to be small angles, then:  $\alpha'' = n \alpha / n_a$ , since:

$$\alpha'' = \frac{n}{n_a} \int_0^L \frac{1}{n} \frac{\partial n}{\partial y} dz \quad (1.27)$$

If the factor  $1 / n$  does not undergo large changes through the test section then:

$$\alpha'' = \frac{1}{n_a} \int_0^L \frac{1}{n} \frac{\partial n}{\partial y} dz \quad (1.28)$$

Since  $n_a \approx 1$  the cumulative angle of refraction of the beam of light, which emerges in the surrounding air is given by:

$$\alpha'' = \int_0^L \frac{\partial n}{\partial y} dz \quad (1.29)$$

The angle to be measured is quite small in the order of  $10^{-6} - 10^{-3}$  radians, and in order to properly observe them, a knife-edge method is settled.

The standard setup is depicted in figure 1.6 .

The light is generated by the source S then a collimating lens L1 transforms the optical wave into a parallel beam that travels through the analysis section, while a focusing lens L2 concentrates the beam on the knife edge as a measurement plane (screen) is set in the conjugate focus of the test section [49].

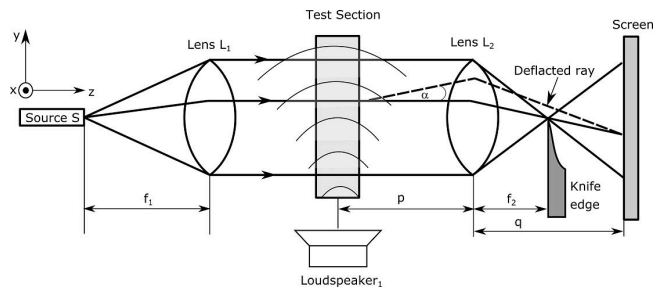


Figure 1.6: Schematic of a standard schlieren imaging system [50]

Therefore if the light beam is deflected when it crosses the test section so that it moves downwards, it is blocked by the edge of the knife and the screen darkens. If it moves up, a greater amount of light falls on the screen and illuminates correctly.

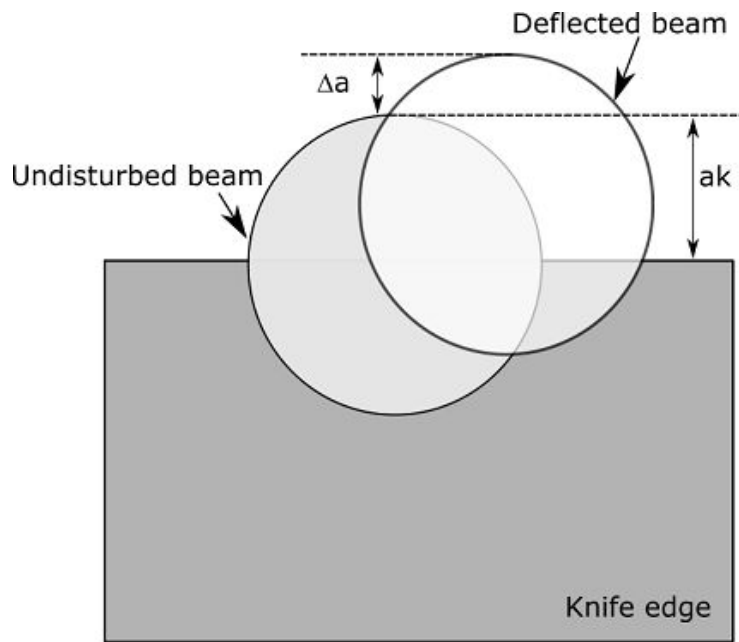


Figure 1.7: Schematic of schlieren setup [50].

The contrast would be the term used to relate the intensity change of a point with respect to the initial intensity at a given point, with the edge of the knife being the element that controls this variable. The screen would be dark if the initial beam of light (not deviated) is completely cut off by the edge of the blade

and a significant increase, however, the illumination of the screen is produced by any subsequent deflection of the beam, the displacements parallel to the edge of the blade, do not change the intensity distribution.

The air flows and shock waves are visualized in great detail using the Schlieren technique, being able to appreciate the physical properties of the air that are not easily perceived. However, if the experiment is performed with different transparent materials, such as glass, water or other media, you can see a reflected image of the environment and the distortion of the background that comes from the refraction of these transparent media. Thus, the materials studied with this technique must have very weak refractive indexes and, there must be no reflection on the optical path, which complicates the visualization of the distortions. Fig. 1.8 shows an image of schlieren representing waves and air flows.

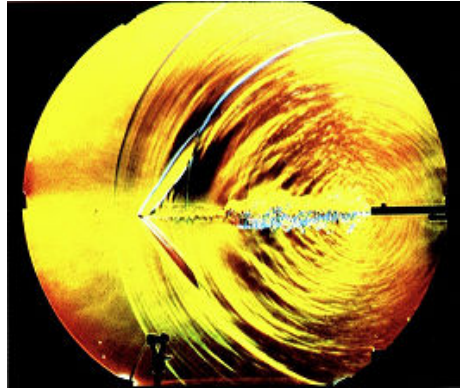


Figure 1.8: Schlieren image of a bullet fired from a gun [51].

According to Settles [40], contrast is fundamental to schlieren's sensitivity, and its digital postprocessing must be applied to highlight the characteristics of low contrast.

### 1.4.3 Shadowgraphy

Shadowgraphy is another technique to visualize the lack of homogeneity of the refractive index in a transparent medium. A typical optical system for shadowing is shown in Fig. 1.9 that consists of a point light source with a collimation lens and a screen where the transmitted light is projected through a phase object. In this case the phase object will be a pressure wave.

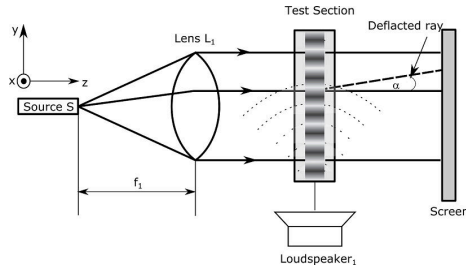


Figure 1.9: Shadowgraphy optical system with a collimated light source.

If the object has a constant refractive index ( $\partial n/\partial x = 0$ ), the light rays are transmitted directly through the object to the screen which observes a constant brightness. With a constant gradient of the refractive index ( $\partial n/\partial x = \text{const}$ ), all the rays of light will deviate with the same angle and the screen will continue to see a uniform brightness. But if the phase object has a complex distribution of refractive index, thus, intensity pattern will appear on the screen.

Figure 1.10 present simulated schlieren and shadowgraph images of a pressure field generated in the air around a sphere at a speed of Mach 3.2. Its calculation was made using a computational fluid dynamics program, and a ray tracing technique [52].

The irradiation pattern of the light in the recording plane is due to the refraction of the light in the flow field in the shadowgraph systems, and the image of the shadowgraph reflects approximately by means of the second density derivative in the test section. Schlieren systems are different from shadowgraphic systems by a knife-edge inserted in the lens focus, and only rays not intercepted by the knife-edge can reach the recording plane.

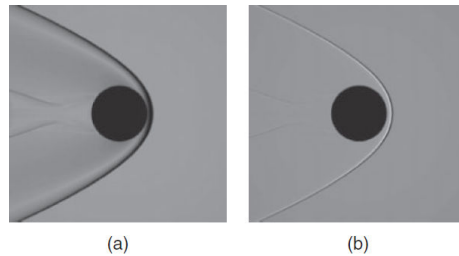


Figure 1.10: Simulation of visualization methods of the air compression induced by a sphere travelling at Mach 3.2 in air. (a) Schlieren image. (b) Shadowgraph [52].

While the schlieren technique visualizes the first derivation of a refractive index field, the shadowgraph technique visualizes the second derivation of the refractive index [53].

#### 1.4.4 Applications of the schlieren method for acoustic images

Although the Schlieren method was originally developed to visualize fluid flows [54, 55], researchers have recently focused their attention on the analysis and visualization of the acoustic field generated by a powerful ultrasonic sound whose pressure can be very high [48, 56, 57], and whose wavelength is much smaller than the audio range. Since the schlieren approach is a full field vision of the wave, observation of shorter wavelength waves is much easier. Also, as can be seen in Fig. 1.11, a higher gradient of changes in the refractive index improves the contrast of the image.

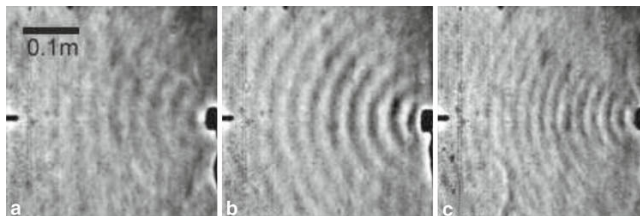


Figure 1.11: Schlieren images of acoustic waves propagating in air at various frequencies and sound pressure level (SPL) (a)  $f=10$  kHz, SPL=109.2 dB (b)  $f=10$  kHz, SPL=119.8 dB and (c)  $f=15$  kHz, SPL=102.5 dB [58]

However, by using space-time filters to extract sound information and to eliminate noise, the visualization of the audible sound fields of Schlieren videos is improved [59]. An implementation of acoustic image processing with very explicit results has been detailed by Chitanont *et al* [60]. The results are presented in Fig. 1.12.

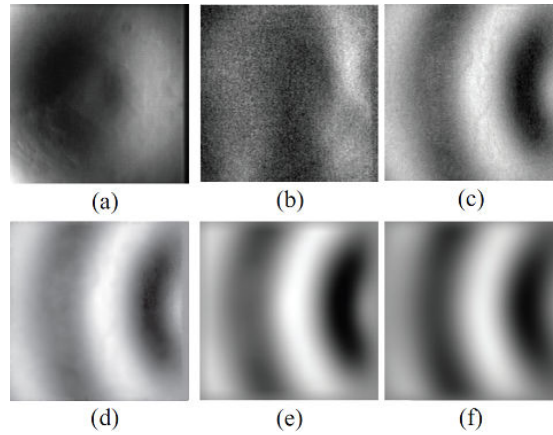


Figure 1.12: 10 kHz sinusoidal sound field. (a) Measured data, (b) data without DC component, (c) time directional filtering by bandpass filter, (d) spatio-temporal filtering by bandpass and Wiener filter, (e) spatio-temporal filtering by bandpass and Gaussian filter, (f) spatio-temporal filtering by 3D Gabor filter[60].

In order to improve the quality of the images of a conventional schlieren optical system, Kudo *et al* [61] proposed a system that uses a short pulse laser, a CCD camera with a wide dynamic range and a dedicated image processing. In this setup, the extraction of the light diffracted by ultrasound waves is performed by subtracting images captured with and without exposure to ultrasound (see Fig. 1.13).

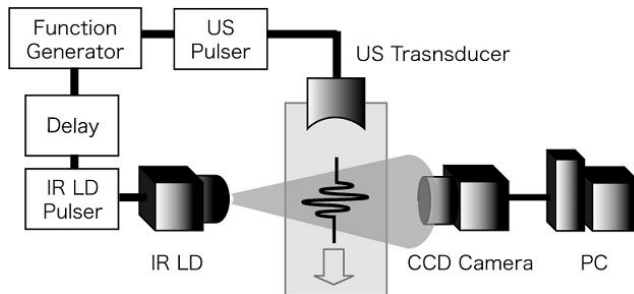


Figure 1.13: A block diagram of optical system with CCD camera [61]

The utility of the developed system was confirmed by an experiment in which the acoustic fields of a transducer focused at 5 MHz were visualized as in Fig 1.14. The images of Fig 1.14 (a). show acoustic fields near the focal point of the transducer, while the images of Fig 1.14 (b) is a two-dimensional simulation. The

difference in the focus effect was visualized in these images.

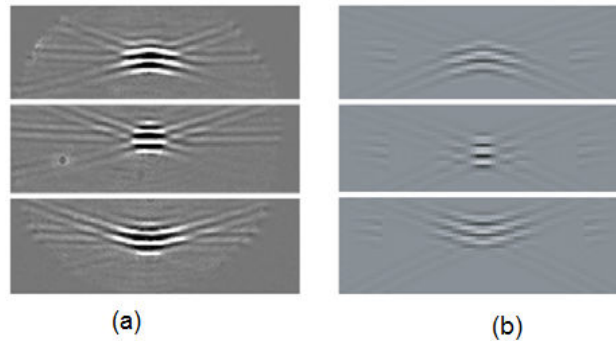


Figure 1.14: Visualized acoustic fields of the focused transducer.[61]

## 1.5 Laser Doppler vibrometer (LDV)

### 1.5.1 Principle of LDV

Laser Doppler velocimetry (LDV) is a technique used to measure the instantaneous velocity of a distant object, usually in a flow. Its principle is based on sending a coherent monochromatic light towards the target where due to the Doppler effect, the reflected radiation is subject to a frequency (wavelength) shift which magnitude is relative to the target velocity. Thus, the velocity of the object is computed by measuring the change in the wavelength of the reflected laser light, into an interferometer (in most of the usual cases a Michelson) where interference fringes frequency is the Doppler shift frequency.

When applied to vibration measurement, the V of velocimetry becomes Vibrometry and the reflected beam returning from the target causes a Doppler shift that corresponds to the vibration velocity of the object under measurement. The reflected beam interferes with the reference beam which is modulated in frequency by means of an acoustic optical modulator (AOM) [62]-[64].

The block diagram of a basic LDV configuration is shown in Figure 1.15.

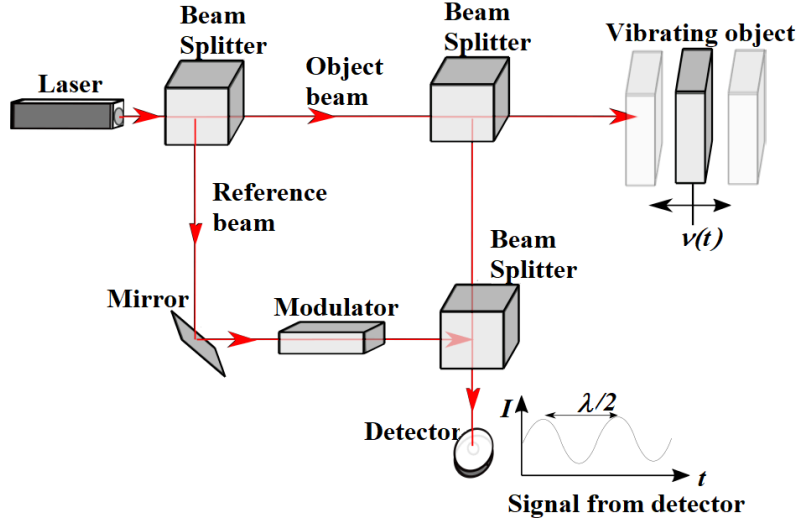


Figure 1.15: Schematic block diagram of an LDV system [65]

First ignoring the AOM modulation, the resulting intensity in the detector will be equal to:

$$I = I_r + I_0 + 2\sqrt{I_r I_0} \cos(\Delta\beta), \quad (1.30)$$

where,  $I_0$  and  $I_r$  are the intensities of the backscattered beam and the reference beam respectively,  $\Delta\beta$  is the phase difference between the two waves that is:

$$\Delta\beta = \frac{2\pi}{\lambda}(l_r - l_0), \quad (1.31)$$

Where  $\lambda$  is the vacuum wavelength of the light  $l_r$  is the path length for a constant reference beam, therefore the intensity in the detector will depend only on the optical path length of the target beam  $l_0$ . This optical path length can be described by the integral

$$l_0 = \int n(x, y, z, t) dl \quad (1.32)$$

where  $n(x, y, z, t)$  is the refractive index along the beam path of the target.

If the target moves with a constant speed the photodetector will produce a current with a sinusoid shape in time, however it is not possible to discriminate the direction of displacement. The acousto-optic modulator frequency shift is equivalent to a fixed velocity of the target. In this way, a movement of the object in the direction of the LDV produces an optical beat with a frequency less than the modulation frequency while a movement away from the sensor produces an optical beat with a higher frequency. It is important to note that by nature the LDV is a point measurement system and in order to produce images, it is

necessary to scan surfaces of a vibrating area which requires that the vibratory phenomenon is periodic and repeatable.

### 1.5.2 Sound field measurements using laser vibrometry

The principle for measuring the acoustic field with a vibrometry laser is similar to the one described above with the only difference that the target remains as a rigid reflector so the distance of the path of the beam LDV and the reflector remains constant.

Figure 1.16 presents a schematic setup, the LDV scanning system is pointing on a rigid reflector, which in this case is a concrete block painted white, and a sound field is propagates through the volume between the sensor and the reflector.

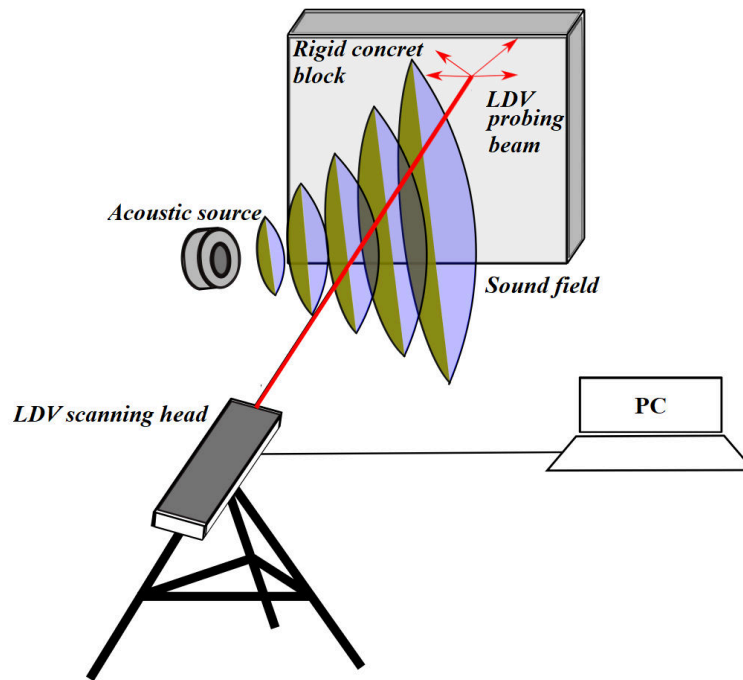


Figure 1.16: Principle of LDV for acoustic imaging

The relation between the change in the optical path and the refractive index change being defined by (1.32), changes in the refractive index will directly impact the interferometer exactly as if the target was moving with a periodic movement at the acoustic frequency.

The ratio of change in acoustic pressure to the refractive index is given by the following adiabatic conditions between pressure and density [65].

$$\frac{p_0 + p}{p_0} = \left[ \frac{\rho_0 + \rho}{\rho_0} \right]^\gamma \quad (1.33)$$

where  $p_0$  and  $\rho_0$  are the pressure and density without disturbances,  $p$  and  $\rho$  are the acoustic contributions to the pressure and density fields and  $\gamma$  defines the specific-heat ratio.

The relationship between the density and the refractive index can be coupled using the Gladstone-Dale equation.

$$n - 1 = K\rho, \quad (1.34)$$

where  $K$  is the Gladstone-Dale constant.

Combining Eqs (1.33) and (1.34), and deriving the expression of refractive index change, The relationship between the rate of change in the refractive index and the rate of variations in the pressure with acoustic pressure much lower than atmospheric pressure is as follows:

$$\frac{dn}{dt} = \frac{(n_0 - 1)}{\gamma} \frac{1}{p_0} \frac{dp}{dt} \quad (1.35)$$

The equation that relates the measured speed and the rate of change caused by the sound field corresponds to the sum of all the fluctuations along the trajectory of the laser beam therefore with this technique it is not possible to perform the measurement in a point.

$$\frac{dl_0}{dt} = 2 \frac{(n_0 - 1)}{\gamma p_0} \int_0^d \frac{d}{dt} p(x, y, z, t) dl \quad (1.36)$$

The measured sound field is, therefore, a two-dimensional projection of a three-dimensional sound field [65]

### 1.5.3 Acoustic imaging by LDV

In the recent years, several publication using LDV for imaging acoustic fields have been published. In 2005, Frank and Schell used LDV to image the acoustic field from a loudspeaker then compare it to the one simulated based on vibration measurement on the speaker membrane using the same LDV system [66]. Later, Oikawa have described a complete methodology for 2D imaging with Polytec systems commercial LDV interferometer [67, 68]. Images of acoustic fields produced by a standard loudspeaker and a flat panel one are reported in Fig. 1.17.

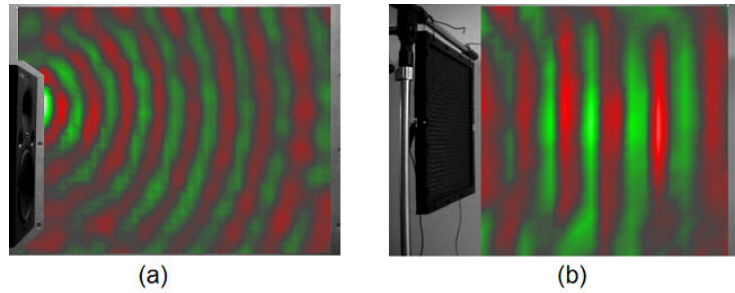


Figure 1.17: Images of acoustic fields produced by (a) an ordinary loudspeaker, (b) a flat panel loudspeaker [67]

Malkin *et al* [69] have proposed to improve the imaging method by taking into consideration the changes in the projection of the refractive index changes while the scanning system changes the propagation direction of the laser beam. They also used a Polytec system which realizes the scanning by deflecting the laser beam on a mobile mirror that induces the orthogonality of the laser and acoustic propagation not to be satisfied in all points of the resulting image. The plots of Fig. 1.18 present the simulations made to highlight this orthogonality issues for both a usual speaker producing a spherical wave and a plane type speakers which acoustic wave is almost a plane one from the origin.

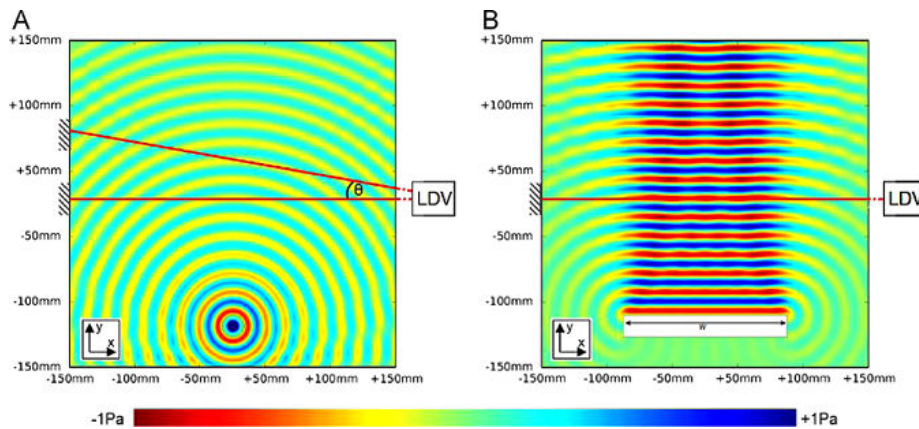


Figure 1.18: Simulated of instantaneous sound fields at 20 kHz showing the position of the LDV system and the rigid reflector [69]

Kentaro Nakamura measured the sound pressure with a laser Doppler vibrometer (LDV) through optical phase modulation due to the acoustic-optical effect of the air, which conducted a study of the acoustic-optical coefficient of

the air giving a quantitative relationship between sound pressure and LDV output. He managed to obtain two-dimensional measurements for a standing wave and a radiated field [70](see Fig. 1.19).

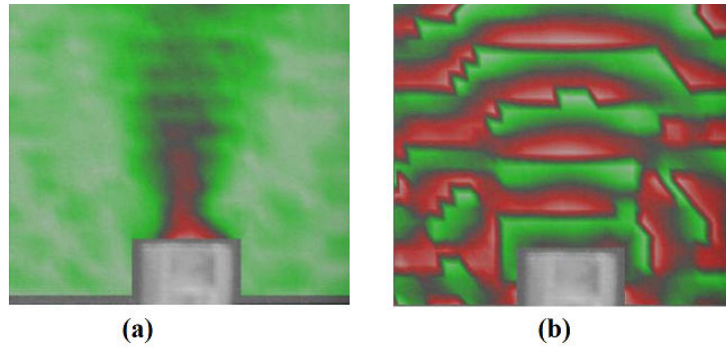


Figure 1.19: Image of an ultrasonic pressure wave with LDV system (a) amplitude(b) phase [70]

Oikawa first proposed to apply LDV combined to tomography which is the first step to realize 3D images of acoustic fields [67]. In this work, tests were performed with an ordinary loudspeaker stimulated by a 4 kHz sinusoidal signal, located on a table with emission direction towards the ceiling in an anechoic chamber. The speaker was rotated manually after each 1D scan and 36 laser projections were taken for the reconstruction that was done using classical computed tomography approach [67, 71, 72].

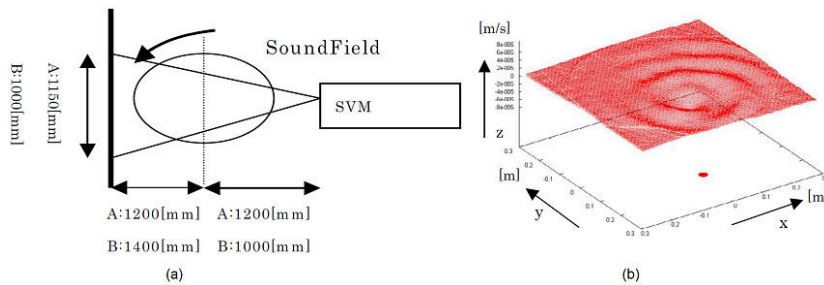


Figure 1.20: Reconstruction of an acoustic wave in a plane by LDV measurement projection (a)Measurement Conditions, (b)Reconstruction from 36 projections.[67]

In other tests, both the real and the imaginary parts were reconstructed separately, and then recombined to obtain a complete image of the 3D sound field. In Fig. 1.21, the real part of the sound field is plotted for different planes.

In this case, 3 transducers were placed, which are located in the  $xy$  plane and  $z = 0$  mm. In (a) the sound field is plotted for the planes  $(x, y)$  at different distances from the source plane. In (b) the sound field is plotted for the planes  $(x, z)$ . In Fig. 1.21(a) it is possible to see that the sound source in the middle seems to be a little out of phase compared to the other two. In Figure Fig. 1.21(b) the propagation of the sound wave is displayed more clearly. In the plotted plane  $Y$ , it can be seen that the sound is stronger in the  $z$  direction.

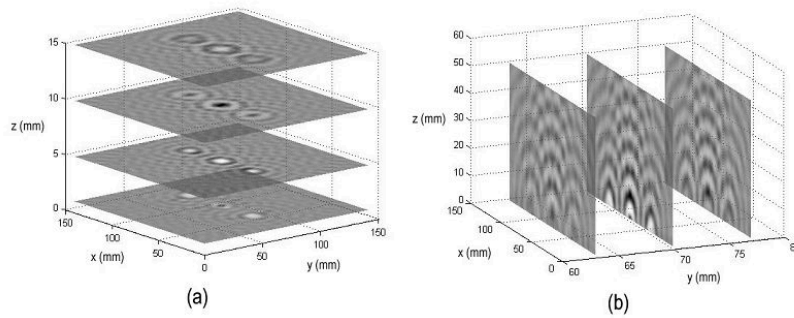


Figure 1.21: The real part of the measured sound field reconstructed using LDV and CT methods (a)  $(x, y)$  - planes (b)  $(x, z)$  - planes [64]

Torras-Rosel *et al* [73] have produced the best images of audio range acoustic 3D measurements using acousto-optic LDV sensing and tomographic imaging approach. The measurements were carried out with a commercial LDV device (Polytech) in an anechoic room of approximately  $1000 m^3$  and the sound field was generated by a speaker powered with a pure tone of 2 kHz. The signal emitted by the loudspeaker was synchronized with the data acquisition system, which allowed the reconstruction of the instantaneous sound field. As seen in Fig. 1.22, the measurement plane was located 12 cm above the speaker. A turntable that ensures the required rotation of the source with regards to the sensor was remotely controlled. It was then translated manually along the perpendicular direction of the light beam allowing scanning in parallel lines. In addition, an accelerometer was added at the top of the reflection target to control that its acceleration induced by the acoustic pressure was insignificant and, therefore, to ensure that the LDV speed output was essentially caused by the acoustic-optical effect.

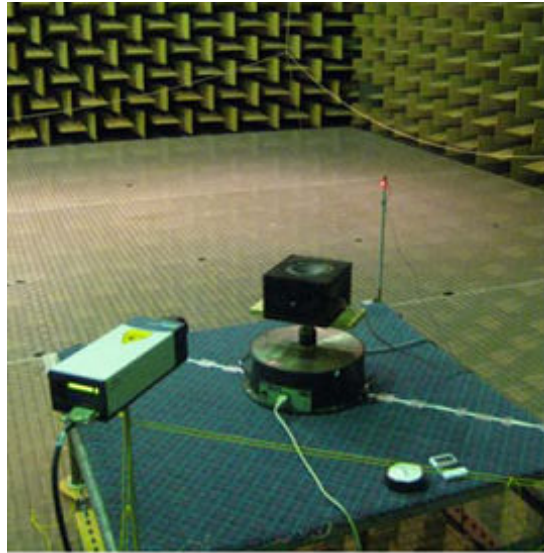


Figure 1.22: LDV setup for 3D images using the tomographic method in the audio range. [73]

The result obtained by using a spatial resolution of 2 cm and an angular resolution of 10 cm is shown in Fig. 1.23. As expected, the resulting sound field is spherically symmetric and exhibits the periodicities of a pure 2 kHz tone.

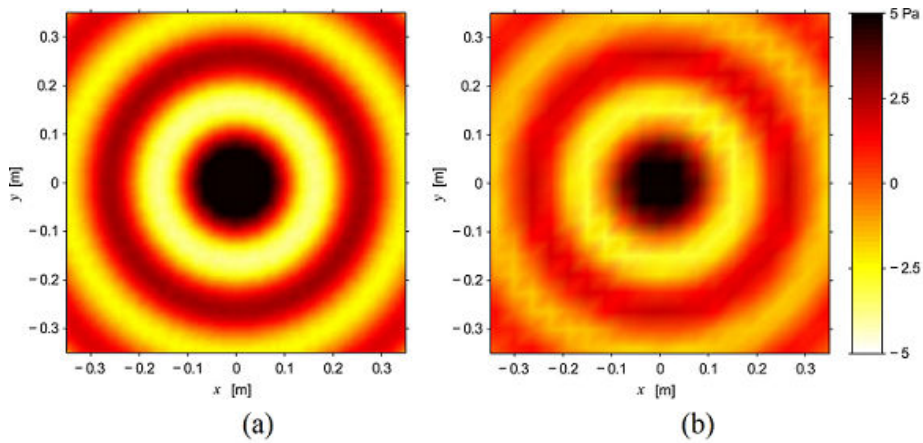


Figure 1.23: Reconstruction of a 2 kHz acoustic wave measured at 16 cm from the speaker surface (a) Spatial resolution 1 cm, angular resolution 1 degree, (b) Spatial resolution 4cm, angular resolution 10 degree. [73]

Complementary measurements were made with a matrix of microphones consisting of sixty 1/4-inch microphones. The general amplitudes and the pressure distribution are quite in accordance with the reconstructed fields.

Scanning the sound field in parallel lines and projecting it in different directions is an inverse problem that can be solved by the inverse Radon transform. In addition, the use of light as a sensor element makes the acoustic-optical effect a non-invasive technique.

## 1.6 Conclusion

The most common methods to obtain images of acoustic waves have been treated throughout this chapter, among them images obtained through an array of microphones that are the actual standard in acoustic imaging systems. But these solutions are limited because the sensor element is placed in the field of propagation of the acoustic wave and thus becomes an invasive element while its resolution is limited to the number of microphones displayed leading to a large sized device or a high cost. Another technique to visualize a sound image is to apply an advanced technique of photography that allows capturing sound or heat called schlieren photography, with which it is possible to capture the variations in the density of a fluid, but this technique that requires fast cameras is limited in uses to laboratory environment due to the complexity of the optical system.

The state of the art of the chapter is completed by the Laser Doppler Vibrometry (LDV) approach that is based on optical interferences. This method is perfectly non-intrusive for the acoustic field. Moreover, it allows to obtain quantifiable images of the sound field. However, with usual interferometric systems, the equipment is too large and highly sensitive to mechanical disturbances and thus, it requires a very controlled environment with most of the time mechanically damped tables that are unlikely to be found in any industrial context.

In a seminal paper Bertling *et al* proposed to use a compact interferometer to replace usual interferometric systems. This interferometer based on the principle of Optical Feedback Interferometry (OFI) has proven its ability to detect the variation of local pressure and the purpose of the present manuscript is to expose the study that have been made in the development of an acoustic imager based on OFI which solves most of the issues encountered with the actual LDV systems.

## Chapter 2

# Acoustic Imaging using Optical Feedback Interferometry

### 2.1 Theory of Optical Feedback Inteferometry for opto-acoustic sensing

Optical feedback interferometry is almost exclusively based on a unique component : the laser, which in most of the cases is a semiconductor laser. The interferometric phenomenon is then tightly linked to the laser physics and a proper description of an OFI sensor can not spare a solid description of the laser itself. In this first section, the oscillation conditions for semiconductor lasers is briefly described, then the case where the laser experiences optical feedback is detailed. In a second section, the opto-acoustic effect and its impact on the laser emission parameters is presented. In the last section, the experimental arrangement for 2D imaging of acoustic waves based on self-mixing is depicted and several results obtained with this method are presented.

#### 2.1.1 Laser oscillation conditions in free running state

For the general description of the dynamics in a semiconductor laser, we must employ the rate equations for the complex amplitude of the electric field (the amplitude and the phase of the field) instead of the photon number since , as in any interferometric system, the phase of the electric field plays a major role. There are several ways to derive the field rate equation, we decided to use a combination of Petermann's approach [74] and Lang and Kobayashi formalism [75].

The model of a Fabry-Pérot resonator is shown in Fig. 2.1. Assuming a cavity length  $l$ , which laser diode's facets are the semiconductor-air interfaces

and are located at  $z=0$  and  $z=l$  with reflectivities  $r_1$  and  $r_2$  respectively.

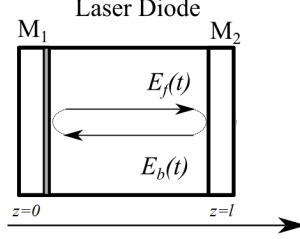


Figure 2.1: Model of Fabry-Pérot laser cavity

The forward travelling complex electric field  $E_f$  can be expressed as

$$E_f(z) = E_{f0} \exp \left[ -j\beta z + \frac{1}{2}(g - \alpha_s)z \right], \quad (2.1)$$

where  $g$  and  $\alpha_s$  are the gain and the absorption in the active area respectively,  $\beta$  is the wavenumber and  $E_{f0}$  is the field amplitude.

The backward travelling wave amplitude is described similarly as

$$E_b(z) = E_{b0} \exp \left[ -j\beta(l - z) + \frac{1}{2}(g - \alpha_s)(l - z) \right]. \quad (2.2)$$

From the boundary conditions,  $E_f$  and  $E_b$  are related to each other by the reflection coefficients,  $r_1$  and  $r_2$  at the laser facets so that  $E_f(z=0) = (E_{f0}) = r_1 * E_b(z=0)$  and  $E_b(z=l) = (E_{b0}) = r_2 E_f(z=l)$ .

Multiplying equation 2.1 and equation 2.2 gives

$$E_{f0} E_{b0} = r_1 r_2 E_{f0} E_{b0} \exp [-2j\beta l + (g - \alpha_s)l]. \quad (2.3)$$

Thus, the steady-state condition for the laser oscillation is

$$r_1 r_2 \exp(-2j\beta l) \exp[(g - \alpha_s)l] = 1. \quad (2.4)$$

The required gain, denoted as  $g_{th}$ , can be calculated from the real part of the above equation

$$g_{th} = \alpha_s + \frac{1}{l} \ln \left( \frac{1}{r_1 r_2} \right), \quad (2.5)$$

while the imaginary part of (2.4) leads to

$$\exp(-2j\beta l) = 1 \quad (2.6)$$

that implies

$$\beta l = m\pi \quad (2.7)$$

where  $m$  is a natural integer.

With an effective refractive index,  $n_e$ , for the lasing mode,

$$n_e = c \frac{\beta}{\omega} = c \frac{\beta}{2\pi\nu} \quad (2.8)$$

where  $c$  is the light velocity in vacuum,  $\nu$  is the optical frequency at free-running state and  $\omega = 2\pi\nu$  the angular frequency. Possible frequencies of the laser modes are given by

$$\nu = \frac{mc}{2ln_e}. \quad (2.9)$$

In the following, we will consider that the laser under study is either a pure singlemode emission device (DFB, DBR or VCSEL) or that it is a Fabry-Pérot operating in singlemode conditions.

### 2.1.2 The laser diode under optical feedback

The schematic model of a laser with optical feedback is shown in Figure 2.2. The light emitted from the front facet of the laser is reflected (or back-scattered) from an external mirror (or scattering surface) and is re-entering the laser cavity with its induced phase shift.

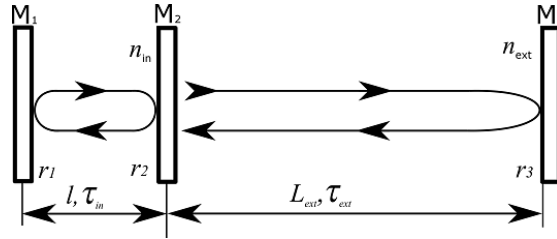


Figure 2.2: Diagram of the three-mirror model

Assuming the mirror (or the scattering surface) is placed within the coherence length of the laser, the double cavity can be reduced to a two-mirrors standard cavity of length  $l$  but with an equivalent reflection coefficient  $r_{eq}$  (see Fig. 2.3).

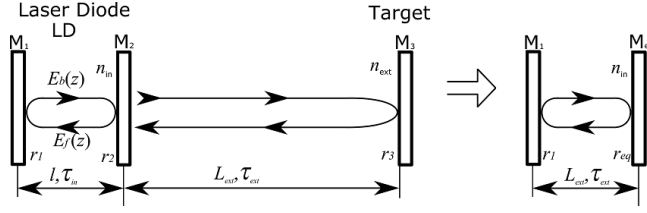


Figure 2.3: Schematic arrangement of a laser diode cavity with external optical feedback.

The equivalent reflectivity coefficient  $r_{eq}$  can be calculated while considering the multiple reflections effects and the delay induced by the round-trip time of flight in the external cavity as

$$r_{eq} = r_2 + (1 - r_2^2)r_{ext} \exp(-j2\pi\nu\tau_{ext}) \quad (2.10)$$

with  $|r_{ext}|$  the ratio of the reinjected field amplitude over the emitted field amplitude. This complex reflectivity can be expressed as

$$r_{eq}(\nu) = |r_{eq}(\nu)| \exp(-j\phi_r), \quad (2.11)$$

where  $|r_{eq}|$  and  $\phi_r$  are respectively the amplitude and the phase of the equivalent reflectivity. In most of the sensing applications,  $r_{ext} \ll |r_2|$  thus

$$|r_{eq}(\nu)| = r_2 [1 + \kappa \cos(2\pi\nu\tau_{ext})] \quad (2.12)$$

while

$$\phi_r = \kappa \sin(2\pi\nu\tau_{ext}). \quad (2.13)$$

The coupling coefficient  $\kappa$  in (2.12)-(2.13) is defined as

$$\kappa = (1 - r_2^2) \frac{r_{ext}}{r_2}. \quad (2.14)$$

Considering only one single longitudinal mode of operation, the amplitude condition for lasing with the equivalent mirror is written as

$$r_1 |r_{eq}| \exp[(g - \alpha_s)l] = 1, \quad (2.15)$$

and from Eq. (2.7), the round trip phase inside the laser diode leads to

$$2\beta l + \phi_r = 2\pi m. \quad (2.16)$$

Thus, the phase condition becomes

$$\frac{4\pi\nu n_e l}{c} + \phi_r = 2\pi m. \quad (2.17)$$

In (2.17), both the refractive index  $n_e$  and the laser frequency are affected by the optical reinjection so that the phase shift of the compound cavity  $\Delta\phi = \phi - \phi_0$  requires further development step to be explicated considering

$$\phi_0 = \frac{4\pi\nu_0 n_{e0} l}{c} \quad (2.18)$$

and

$$\phi = \frac{4\pi\nu n_e l}{c} + \phi_r, \quad (2.19)$$

so that

$$\Delta\phi = \frac{4\pi l}{c} (\nu n_e - \nu_0 n_{e0}) + \phi_r \quad (2.20)$$

where the variation of  $n_e\nu$  can be linearized as

$$\Delta(n_e\nu) = \nu_0 \Delta n_e + (\nu - \nu_0) n_{e0}. \quad (2.21)$$

At first, from (2.15), the threshold gain with optical feedback can be calculated as:

$$g = \alpha_s + \frac{1}{l} \ln\left(\frac{1}{r_1 r_2 [1 + \kappa \cos(2\pi\nu\tau_{\text{ext}})]}\right), \quad (2.22)$$

and the shift of threshold gain under optical feedback is:

$$\Delta g_{\text{th}} = (g - g_0) = -\frac{1}{l} \ln[1 + \kappa \cos(2\pi\nu\tau_{\text{ext}})] \quad (2.23)$$

However, the condition  $|r_{\text{eq}}| \ll r_2$  leading to  $\kappa \ll 1$ , the variation in Eq. 2.23 can be rewritten as

$$\Delta g_{\text{th}} = -\frac{\kappa}{l} \cos(2\pi\nu\tau_{\text{ext}}). \quad (2.24)$$

The changes induced by the optical feedback on the threshold gain  $g$  and the laser frequency  $\nu$  have a direct impact on the effective refractive index of the laser cavity  $n_e$ . The change in refractive index can be linearized as

$$\Delta n_e = \frac{\partial n_e}{\partial N} (N - N_{\text{th}}) + \frac{\partial n_e}{\partial \nu} (\nu - \nu_0), \quad (2.25)$$

where  $\nu_{th}$  is the optical frequency at threshold,  $N$  the carrier density in the laser cavity and  $N_{\text{th}}$  the carrier density at threshold. The relationship between the carrier density variation and the gain in the active layer of the laser introduces the linewidth enhancement factor  $\alpha$ :

$$\frac{\partial n_e}{\partial N} (N - N_{\text{th}}) = -\frac{\alpha c}{4\pi\nu_0} \Delta g_{\text{th}}. \quad (2.26)$$

From Eqs. (2.20), (2.21), (2.25) and (2.26), the variation of the phase can be expressed as :

$$\Delta\phi = \frac{4\pi l}{c} \left[ -\frac{\alpha c}{4\pi} \Delta g_{\text{th}} + \nu_0 \frac{\partial n_e}{\partial \nu} (\nu - \nu_0) + n_e (\nu - \nu_0) \right] + \phi_r. \quad (2.27)$$

Then, introducing the group refractive index  $n_g$  as

$$n_g = n_e + \nu \frac{\partial n_e}{\partial \nu}, \quad (2.28)$$

and using (2.13) and (2.24), we obtain

$$\Delta\phi = \frac{4\pi n_g l}{c}(\nu - \nu_0) + \kappa[\sin(2\pi\nu\tau_{\text{ext}}) + \alpha \cos(2\pi\nu\tau_{\text{ext}})]. \quad (2.29)$$

The round trip delay inside the laser cavity,  $\tau_{\text{in}}$  being

$$\tau_{\text{in}} = \frac{2ln_g}{c}, \quad (2.30)$$

the the Eq. (2.29) becomes

$$\Delta\phi = 2\pi\tau_{\text{in}}(\nu - \nu_0) + \sqrt{1 + \alpha^2} \sin[2\pi\nu\tau_{\text{ext}} + \arctan(\alpha)]. \quad (2.31)$$

Thus considering that  $\Delta\phi = 0$  as it is required to respect the condition of (2.17) and introducing the feedback parameter  $C$ , which describes the strength of change due to optical feedback [76]

$$C = \frac{\tau_{\text{ext}}}{\tau_{\text{in}}} \kappa \sqrt{1 + \alpha^2}, \quad (2.32)$$

the phase condition of a laser under feedback can be written:

$$(\nu - \nu_0) + \frac{C}{2\pi\tau_{\text{ext}}} \sin[2\pi\nu\tau_{\text{ext}} + \arctan(\alpha)] = 0 \quad (2.33)$$

Equation (2.33), that is called excess phase equation and that can be found in literature under the following formalism [77]

$$\phi - \phi_0 + C \sin[\phi + \arctan(\alpha)] = 0, \quad (2.34)$$

is the core of the optical feedback interferometry phenomenon.

The feedback parameter  $C$  plays here a major role since by its value it defines the behavior of the laser under reinjection. For  $C < 1$ , Eq. (2.33) accepts only one solution, while for  $C > 1$ , several solutions or external cavity modes around the emission frequency  $\nu_0$  may satisfy the phase equation.

It is useful to consider the term  $\phi_0$  as a phase stimulus symbolically corresponding to the phase accumulated on transmission through the internal cavity if the laser has not experienced optical feedback and  $\phi$  as a phase response, corresponding to the actual phase accumulated on transmission through the external cavity [78, 79]. The feedback level  $C$  dictates the degree of nonlinear coupling between phase stimulus and response, while the linewidth enhancement factor  $\alpha$  governs the asymmetry of the phase transfer function induced by (2.33). The phase  $\phi$  evolution against variations of  $\phi_0$  is plotted for three values of  $C$  on Fig. 2.4.

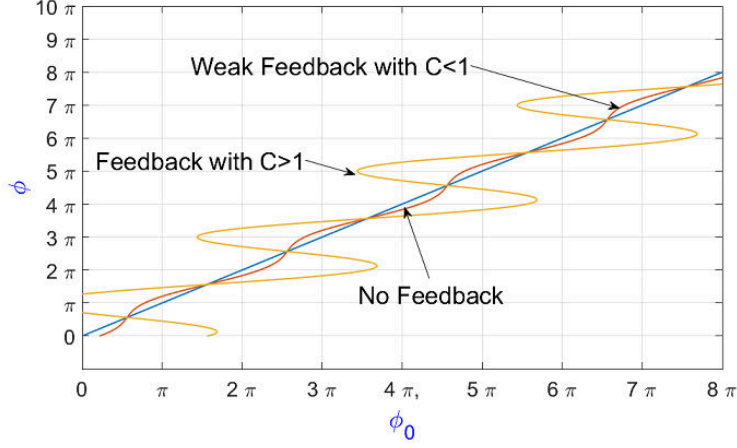


Figure 2.4: Solution of Eq. (2.34) for  $C < 1$  (red line),  $C > 1$  (yellow line) and no feedback (blue line).

Solving Eq. (2.33) is trivial under the weak feedback regime ( $C < 1$ ) while it becomes more complicated in moderate/strong feedback regime where stability of solutions as well as determination of the selected solution must be addressed.

After solving the phase response, linearization of the propagation equation in the cavities leads to the description of the laser through its rate equations

$$\frac{dE(t)}{dt} = \frac{1}{2}(1 - i\alpha)G_n [N(t) - N_{\text{th}}] E(t) + \frac{\kappa}{\tau_{\text{in}}} E(t - \tau_{\text{ext}}) \exp(i\omega\tau_{\text{ext}}) \quad (2.35)$$

and

$$\frac{dN(t)}{dt} = \frac{\eta_i I}{qV} - G_n [N(t) - N_{\text{th}}] S(t) - \frac{N(t)}{\tau_n} \quad (2.36)$$

where  $I$  is the laser injection current,  $V$  is the volume of the laser active layer and  $\tau_n$  the carrier lifetime in the cavity. The gain term  $G_n$  is defined from the group velocity  $v_g$  and the differential gain

$$G_n = v_g \frac{dg}{dN}. \quad (2.37)$$

$S$  stands for the photon density in the cavity that is directly related to the electric field amplitude by

$$S(t) = |E(t)|^2 \quad (2.38)$$

Solving this set of equation leads to express the optical power of the laser diode under reinjection as,

$$P_F = P_0[1 + m \cos(2\pi\nu\tau_{\text{ext}})], \quad (2.39)$$

where  $m$  is the modulation index defined by

$$m = \frac{4n_{\text{ext}}\tau_s}{\tau_{\text{in}}}\kappa, \quad (2.40)$$

where  $\tau_s$  is the photon life time in the laser cavity and  $n_{\text{ext}}$  is the refractive index in the external cavity.

Considering  $\phi = 2\pi\nu\tau_{\text{ext}}$ , Eq. (2.39) becomes

$$P_F = P_0[1 + m \cos(\phi)], \quad (2.41)$$

thus highlighting the importance of the phase excess equation in the determination of the optical feedback sensor signal.

### 2.1.3 Measuring changes of refractive index in the external cavity

The sound is the propagation of a compression wave in a medium which molecular structure becomes denser. In transparent medium such as air or water, the refractive index is increased with molecular density. Therefore, the acoustic wave propagating between the laser and the distant reflector changes the index within the external cavity. In the following, we will consider only the case of acoustic compression of the air in the audio range (20 to 120 decibels) where the changes of the refractive index is extremely small and leads to variations of the round-trip time that is very limited. In the case of a plane wave propagating perpendicular to the laser beam propagation direction, the variation of the refractive index is uniform along the light path and can be written as

$$n_{\text{ext}}(t) = n_0 + \delta n_{\text{ext}} \sin(2\pi ft) \quad (2.42)$$

with  $n_0$  the refractive index of the transparent medium without pressure changes and  $\Delta n_{\text{ext}}$  the amplitude of the variation of refractive index. The small variation of the refractive index criteria is  $\delta n_{\text{ext}} L_{\text{ext}} \ll \lambda/2$ . Under this condition, the induced variation of the phase term  $\phi$  is

$$\delta\phi = 2\pi\nu \frac{2\delta n_{\text{ext}} L_{\text{ext}}}{c} \ll 2\pi. \quad (2.43)$$

Under this condition, by linearization of equation (2.34), it can be shown that

$$\tau_0 \delta\nu \sim (\nu_0 - \nu) \delta\tau \ll \nu \delta\tau \quad (2.44)$$

where  $\delta\nu$  is the change of laser frequency induced by the change of  $n_{\text{ext}}$  and the round-trip time of flight in the external cavity  $\tau_{\text{ext}} = \tau_0 + \delta\tau$ . Thus, the laser frequency  $\nu$  is not significantly modified by the refractive index changes in the external cavity and in first approximation it can be considered as constant leading to transform equation 2.45 as

$$P_F = P_0[1 + m \cos(2\pi\nu(\tau_0 + \delta\tau))], \quad (2.45)$$

Figure 2.5 shows the computation of the electric field phase and the laser power for a sinusoidal change of refractive index in time for a coupling coefficient  $C = 5$ , a distance  $L_{\text{ext}} = 30$  cm and for a variation of  $n_{\text{ext}}$  of  $3.33 \cdot 10^{-7}$ , thus corresponding to an equivalent displacement of 100 nm.

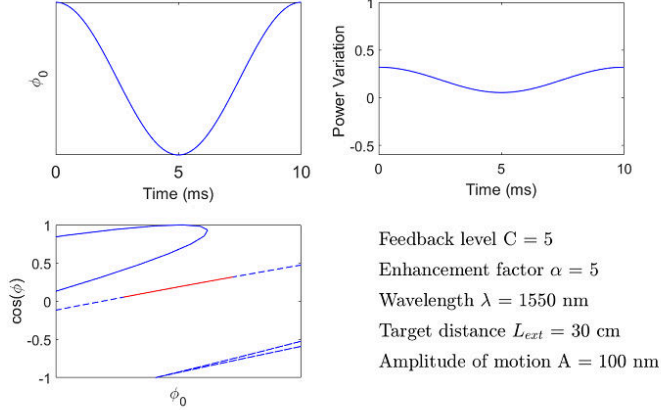


Figure 2.5: Computation of the power variation for  $C=5$ ,  $L_{\text{ext}}=30$  cm and  $\delta n_{\text{ext}} = 3.33 \cdot 10^{-7}$ .

In the general case, where the acoustic wave does not propagate perpendicularly to the laser axis with an ideal flat front wave, the difference in external roundtrip time  $\delta\tau$  must consider the integration of the refractive index change over the full round-trip [80]

$$\delta\tau = 2 \int_0^{L_{\text{ext}}} \frac{\delta n(z)}{c} dz \quad (2.46)$$

The refractive index of air, in turn, depends on the local pressure in a linear fashion [81], whose subject was analyzed in the first chapter of this thesis.

#### 2.1.4 Modeling the projection of the pressure wave in a 2D plane

According to (3.2), the sensor signal is very sensitive to the shape of refractive index variation along the  $z$  axis. In order to model the signal, considering that acoustic pressure waves that will be imaged are spherical waves (and not plane waves), it is required to simulate their propagation in the sensing volume. For the simulation of the acoustic wave, we used the Huygens-Fresnel principle extend to acoustics [82],[83], [84] where we defined the piezo vibrating surface as an array of punctual sources (Fig. 2.6).

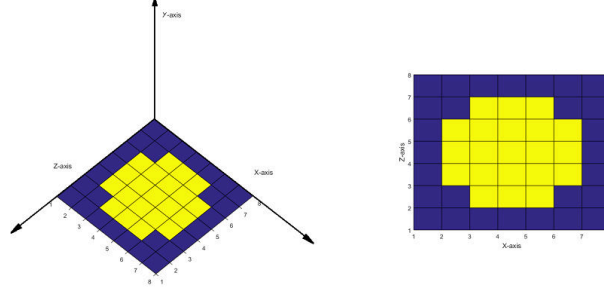


Figure 2.6: Position of the source in plane (X,Z)

The coordinates defining the location of each source  $S_i(x'_i, z'_i)$  in the (X,Z) plane are expressed from the coordinates  $(x_c, z_c)$  of the center of the vibrating surface as

$$\begin{aligned} x'_i &= x_c + r_i \cos(\varphi_i) \\ z'_i &= z_c + r_i \sin(\varphi_i), \end{aligned} \quad (2.47)$$

with  $r_i$  ranging from 0 to  $r_p$  the radius of the piezo-actuator surface and  $\varphi_i \in [0, 2\pi]$ .

Each source  $S_i(x'_i, z'_i)$  emits a spherical wave defined by

$$P_i(x; y; z; r'; t) = \Re \left[ \frac{P_0}{N} A(r') \exp^{j(\omega_p t - k_p r')} \right] \quad (2.48)$$

where  $P_0$  is the total pressure variation amplitude of the source,  $N$  is the number of sources,  $\omega_p$  and  $k_p$  are the angular frequency and wavenumber of the pressure wave.

$r'$  is the distance from the point source  $i$  located at  $(x'_i, y'_i, z'_i)$  to the field point  $(x, y, z)$ .

$$r' = \sqrt{(x - x'_i)^2 + (y - y'_i)^2 + (z - z'_i)^2} \quad (2.49)$$

$A(r')$  that takes into account the weakening of the pressure amplitude due to dispersion over a larger surface can be approximated by an exponential decay

$$A(r') = e^{\frac{-(r')^2}{\sigma^2}} \quad (2.50)$$

The parameter  $\sigma$  has been fitted from measurements that are presented further in the document,  $P_0$  has been set to 1 arbitrarily and  $N$  has been set to 28 as can be seen in Fig. 2.6.

The total pressure field  $P_T$  emitted by the piezo-actuator is the the sum of each localized contribution

$$P_T(x; y; z; t) = P_0 \sum_{i=1}^N A(r'_i) P_i(x; y; z; r'_i; t) \quad (2.51)$$

The simulation results are plotted in Fig. 2.7 both in the (X,Y) plane for  $z = z_c$  and the (X,Z) plane for  $x = \lambda_s$ ,  $\lambda_s$  being the acoustic wavelength. The first image represents an ideal image of what should be an exact representation of the pressure wave, and in the second case the reason why the image measured by the OFI sensor will be a distorted version of the first.

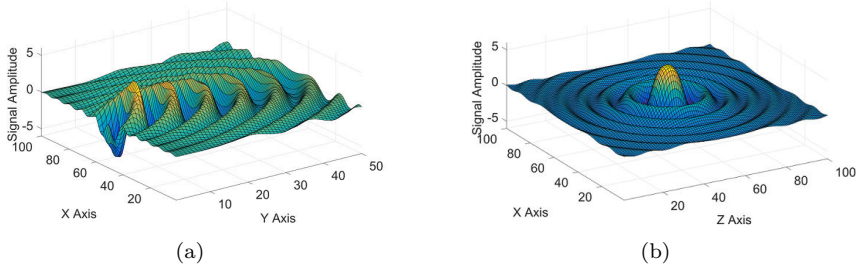


Figure 2.7: Simulation of the pressure wave (a) in the (X,Y) plane for  $z = z_c$  and (b) in the (X,Z) plane for  $y = \lambda_s$

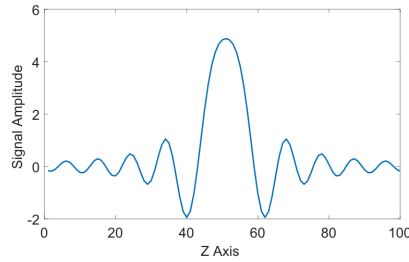


Figure 2.8: Simulation of the pressure wave along the Z axis at  $y = \lambda_s$

Indeed, as can be observed in Fig. 2.8, the integration along the Z axis where the laser is propagating results in integrating a complex function which depends on the distance to the center of emission :

$$P_{T,OFI}(x, y) = \int_0^{L_{\text{ext}}} P_T(x; y; z) dz \quad (2.52)$$

The result of such integration along the Z axis produces the image plotted in Figs. 2.9 and 2.10.

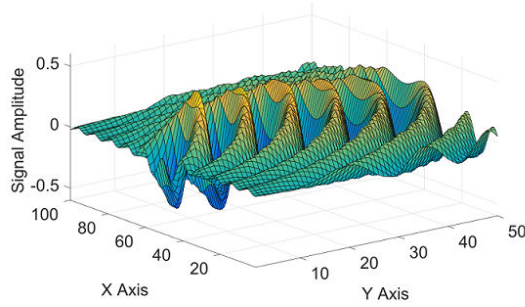
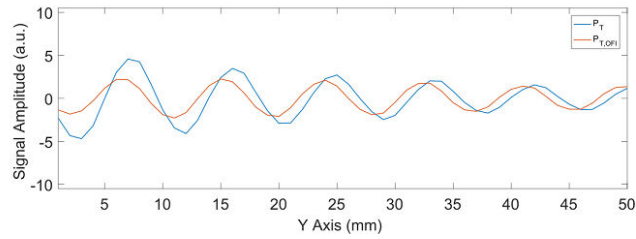
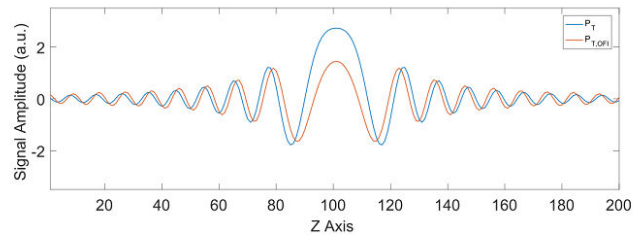


Figure 2.9: Simulation of the pressure wave in the (X,Y) plane as observed by the OFI sensor



(a)



(b)

Figure 2.10: Comparison of the simulated pressure wave and simulated as viewed by the OFI sensor (a) along the Y axis for  $z = z_c, x = x_c$  and (b) along the Z axis for  $y = 25$  mm,  $x = x_c$

The comparison between the projected wave ( $P_{T,OFI}$ ) and the pure simulation of the wave  $P_T$  shows that both are very resembling although they are slightly spatially shifted.

For the pressure wave considered in this study, the differences between the actual pressure wave and the projection realized by the OFI sensing scheme are not a major issue and the induced distortion is limited. However, this could become a major issue in the case of more complex propagation where the integration of the pressure wave along the laser axis will not anymore properly render information on the actual acoustic.

## 2.2 Experimental setup for imaging acoustic pressure waves

### 2.2.1 Design of the acoustic optical feedback interferometry setup for one point

The general principle for imaging of the acoustic pressure wave implies that it propagates between the laser source and the reflector that realize the external cavity. Ideally, the pressure wave propagation axis is perpendicular to the light wave one, and the acoustic source is located at equal distance from the laser and the reflector as depicted in Fig. 2.11.

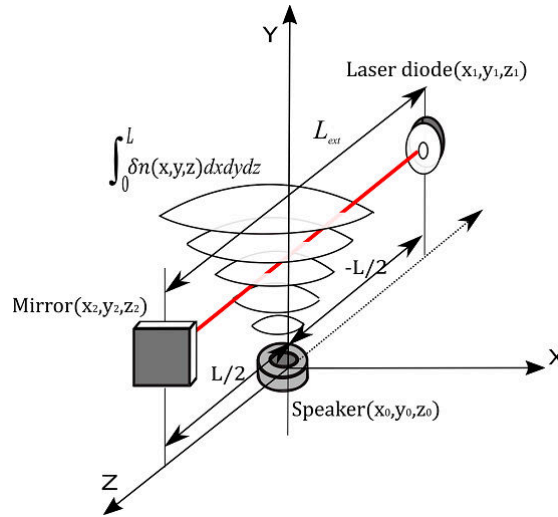


Figure 2.11: Design of the acoustic setup by optical feedback interferometry

The optical feedback interferometer consists of a laser diode L1320P5DFB with a single-mode transverse and longitudinal emission at  $\lambda = 1310$  nm. The laser is radiating on a 25.4 mm diameter enhanced Aluminum mirror (Thorlabs PF10-03-F01) through a collimation lens (Thorlabs C240TME-C). The length of the external cavity  $L_{ext}$  between the laser and the mirror is set to 200 mm and both are mounted with the support of optomechanical holders over micrometric

translation stages. The mirror alignment can be corrected with two angular degrees of freedom (Fig. 2.12).

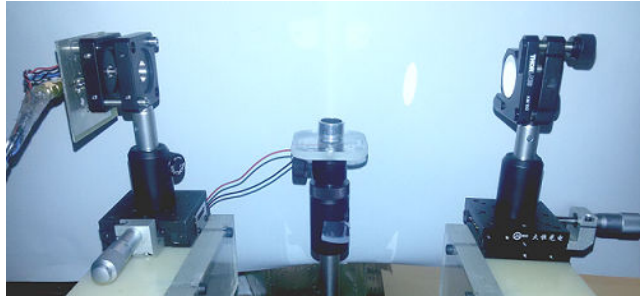


Figure 2.12: Photography of the experimental setup for measurement in one point

The acoustic source is an ultrasonic piezoelectric transmitter (KPUS-40T-16T-K768) of diameter 12 mm, driven by a sinusoidal voltage of 10 V peak-to-peak amplitude at 40 kHz. This signal is produced by a simple function generator and the acoustic power is expected to reach 117 dB according to the manufacturer's datasheet, although it was not possible to verify experimentally this parameter.

The electronics associated to the sensors consists of a custom made laser driver that delivers a controlled DC current, and a transimpedance amplifier that collect the current variation of the monitoring photodiode that is embedded in the laser diode package. The multi-stage amplifier has a total gain of  $100 \text{ dB}_{V/A}$  and it is connected to a National Instrument 16 bits acquisition card with a sampling frequency of 1 MS/s.

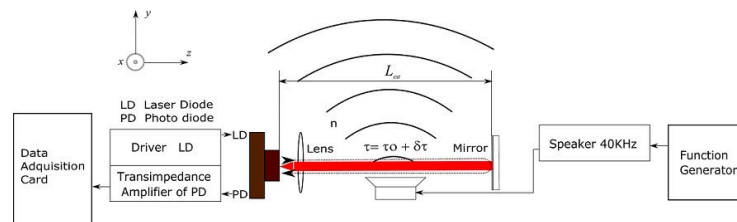


Figure 2.13: Design of acoustic optical feedback interferometry setup

## 2.2.2 Acquisition of signal in one point

The laser power variations acquired through the monitoring photodiode are collected and processed through a Labview program developed for this application. The acquisition consist in 1000 samples of the amplified photodiode

current as plotted in Fig. 2.14(a) as well as the computed Matlab's FFT algorithm (Fig. 2.14(b)).

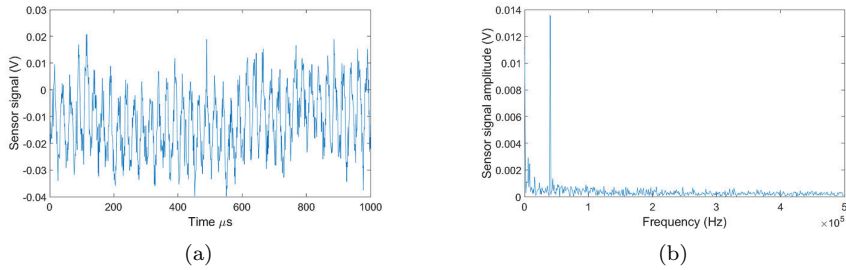


Figure 2.14: Unprocessed sensor signal at X mm of the speaker. (a) in time domain and (b) in spectral domain after computation of Matlab's FFT.

Observing the signal in the frequency domain, we can see a fundamental frequency that coincides with the frequency of the signal that is fed to the sound source (40 kHz in this case). In order to remove the noise of the signal that can be observed in figure 2.14(a), a second order Butterworth bandpass filter can further be applied. In the case of an excitation at 40 kHz, the low cut-off frequency is set at 38 kHz, while the high cut-off frequency is 42 kHz.

The filter is designed using the Matlab Signal Processing Toolbox, leading to an impulse response (Fig. 2.15) where it can be deduced that the filter settling time requires roughly 250 samples.

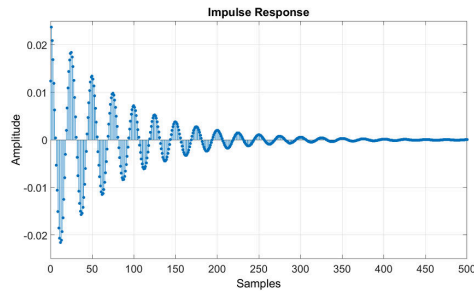


Figure 2.15: Impulse response

Therefore, the analysis of the filtered signal (Fig. 2.16(a)) will be carried out after elimination of the first 250 samples. Applying the FFT algorithm to the filtered signal, we can see the filtered a much cleaner signal with no major impact on the fundamental amplitude (Fig. 2.16(b)).

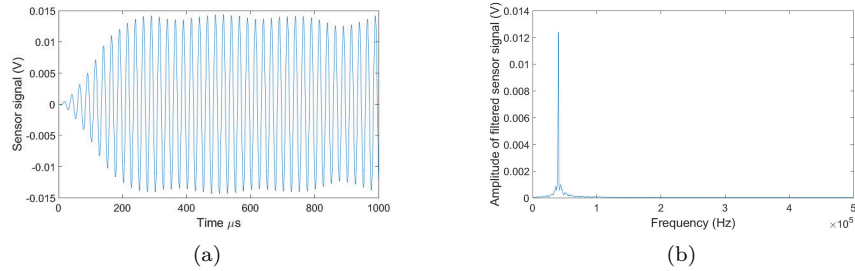


Figure 2.16: Filtered sensor signal at X mm of the speaker. (a) in time domain and (b) in spectral domain after computation of Matlab's FFT.

### 2.2.3 Producing images of acoustic pressure waves

The data acquired so far represent the variation of the refractive index and thus the pressure at a random point in the acoustic field. In order to realize an image of this field or even a movie of the field propagation, we need to acquire several signals at different positions and different distances from the sound source. It naturally results in a phase shift of the variation in time that differs for any position in space and a synchronization of the acquisition with the excitation signal is required to take this effect into account. The displacement of the measuring point can be performed by two different methods : either by a displacement of the source or by the displacement of both the laser and the reflector. Although the first option is the most convenient in laboratory environment, it is often complex in real-life application. Thus, the approach we choosed in this work is to move the sensor (ie. the laser and the reflector). We have built a U-shaped holder (Fig. 2.17) on which the laser and focusing lens on one side and the reflector on the other side are fixed. The holder is mounted on displacement axis (in one, two or later three dimensions) which positions are controlled through the Labview VI.

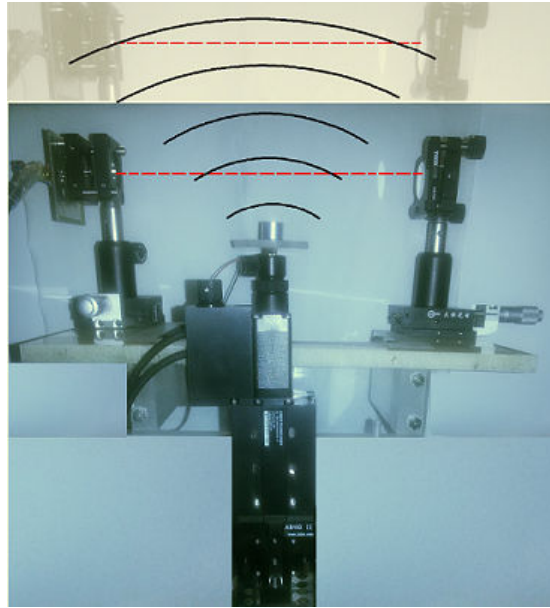


Figure 2.17: Picture of the imaging setup for 2D scanning of the acoustic wave.

## 2.3 Characterization of the radiation pattern of acoustic sources

One of the simplest arrangement of great interest in acoustic sensing is to evaluate the radiation pattern of acoustic sources. Based on the OFI sensing scheme, we propose a simple setup that allows a non-intrusive measurement of this major feature of acoustic systems. The acoustic source (here an ultrasonic piezoelectric transmitter (MA40B8S) driven by a 40 kHz sinusoidal voltage) is mounted on a rotating stage controlled by a step motor. The optical feedback interferometer consists of a ML725B11F laser diode that emits at 1310 nm and a reflective microsphere tape stiched to a bulky metal plate as the distant reflector. The external cavity has a length of 200 mm and the acoustic field propagates in a plane that is perpendicular to the propagation axis of the laser (Fig.2.18(a)). The distance between the laser beam and the acoustic source is set to 100 mm which represents roughly 12.5 times the pressure wavelength.

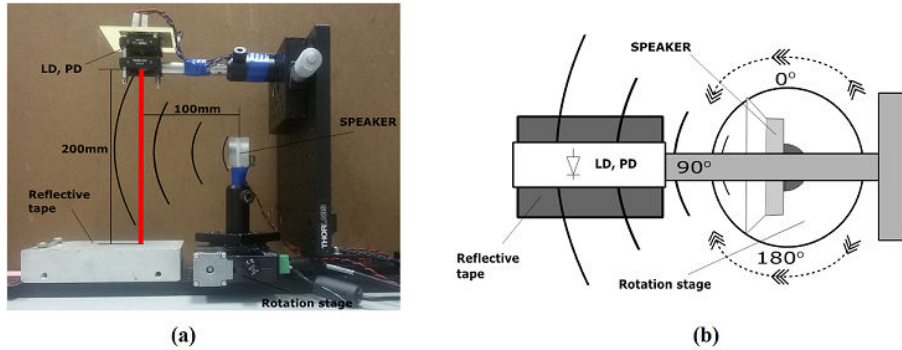


Figure 2.18: (a) Side view of the set-up including an ultrasonic piezoelectric transmitter (MA40B8S) driven by a 40 kHz, 10 V<sub>pp</sub> sinusoidal voltage and the optical feedback interferometer. (b) Top view of the configuration, showing the position of the rotating platform from 0° to + 180° with movement in a clockwise and counterclockwise direction.

A Labview program controls the acquisition, as well as the position of the rotating stage from 0° to + 180° with a step of 1 degree. In each angular position, 4096 samples of the amplified photodiode current are obtained, then the Fast Fourier Transform is computed.

Figure 2.19(a) shows the OFI sensor signal for 0, 90 and 180° and it can be seen that, as expected, the sound pressure is much stronger in the normal direction of propagation (90°) than in the lateral directions. Figure 2.19(b) shows the FFT of the sensor signal at a position corresponding to 90° in the sketch of Fig.2.19(b) and the peak at the excitation frequency of the loudspeaker rises 30 dB from the noise floor.

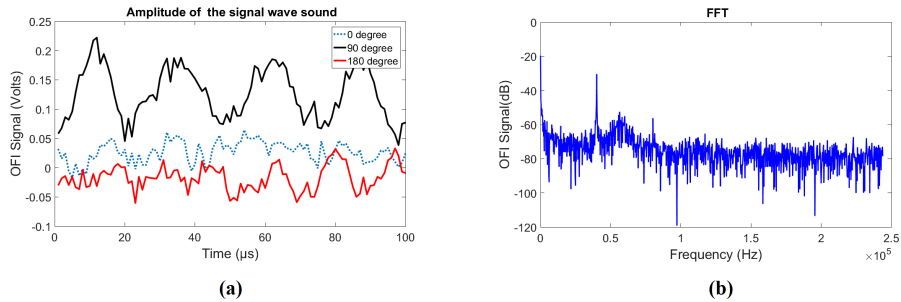


Figure 2.19: Measurement results. (a) Time domain signals at 0° (blue dotted line), 90° (black line) and 180° (red line) (b) Frequency domain signal when the propagation of the sound is made to the laser beam ( corresponding to 90°).

The amplitude of the 40 kHz peak in the FFT is stored and a polar graph

representing the pressure radiation pattern of the acoustic source is generated as shown in Fig. 2.20 .

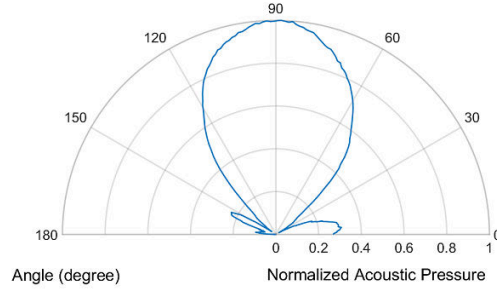


Figure 2.20: Standard acoustic pressure radiation pattern.

As expected the piezo actuator produces an almost Lambertian type radiation with weak directivity in the central axis. The lateral lobes are most likely due to the reflection on the room walls.

With this method we have developed a simple and reliable instrument that can be used for the characterization of acoustic sources such as loudspeakers with a very simple arrangement.

## 2.4 Charaterization of the source along its propagation axis (1D)

One of the parameter of (2.51), the attenuation term as a function of the distance to the source can easily be determined by a characterization of the decrepency of the signal amplitude along the Y axis from the center of the vibrating surface. In order to perform this characterization, a displacement stage on the  $y$  axis has been assembled using a T-LSM050A motorized linear stage, 50 mm stroke, encoder and integrated motor controller.

The position of the  $x$  axis is fixed to  $x_c$ , and the signal is acquired after each dispalcement of 1 mm in the range [1-50 mm]. The trigger of the acquisition is ensured by the function generator which drives the piezo actuator thus ensuring an evaluation of the phase of the acquired signal with regards to the excitation signal.

The FFT is computed and the amplitude of the signals at each location along the Y axis produces the curve of Fig. 2.21.

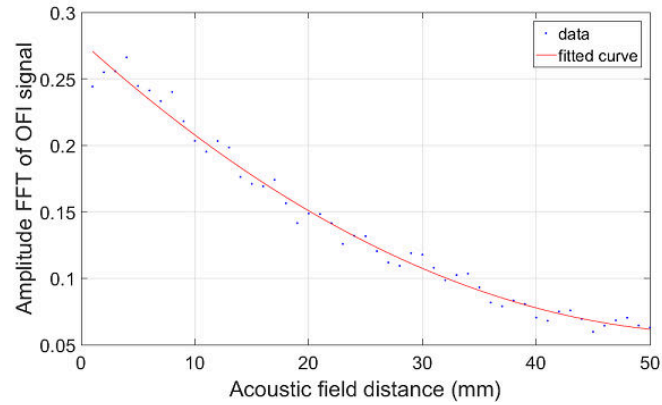


Figure 2.21: Estimation of the  $A(r)$  attenuation function of the acoustic wave as function of the distance to the vibrating surface center

For a given time (here  $t=350\mu\text{s}$ ), the image of the pressure wave is presented in Fig. 2.22 where it is compare to the simulation computed based on 2.51.

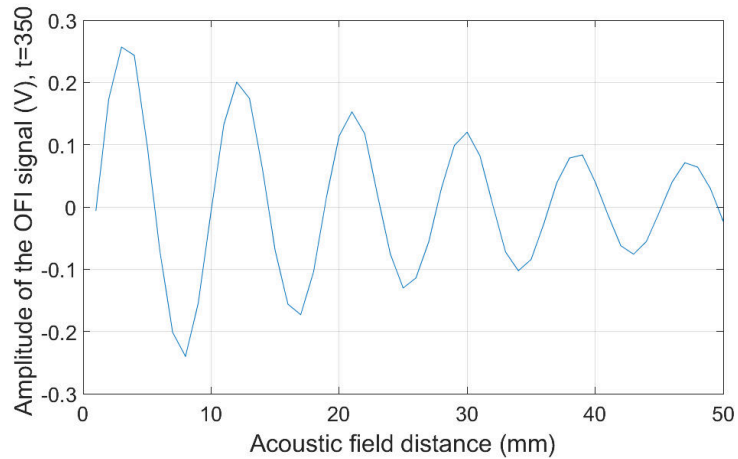


Figure 2.22: Measurement of the acoustic field, 50 points separated each 1 mm.

### 2.4.1 Imaging acoustic propagation in two Dimension

The next step is the measurement of signals by modifying the positions along both the X axis and the Y axis. An additional motorized linear stage is added to the previous setup allowing for X axis translation. The original setup (Fig.2.13)

is conserved so the synchronized OFI signal will be acquired in different positions in the plane (X,Y) with a displacement step of 1 mm on both axis.

The additional translation stage is a T-LSM100A motorized linear stage with 100 mm stroke, encoder and integrated motor controller. the whole assembly is represented in Fig. 2.23.

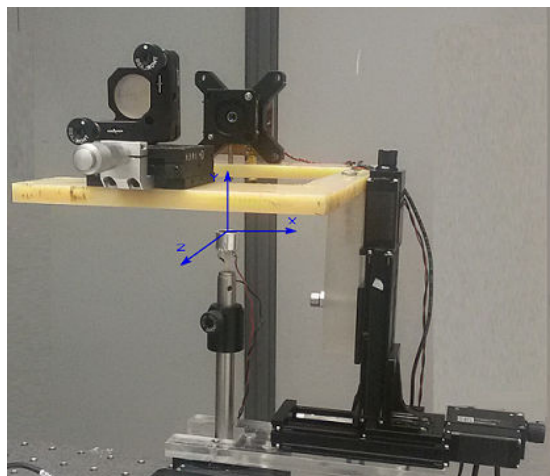


Figure 2.23: Picture of the OFI setup for 2D imaging

Figures 2.24 and 2.25 present the raw image of the acoustic wave produced by the the piezo-actuator as measured by the OFI sensor and for a fixed time, while the Figs. 2.26 and 2.27 present the same acquisition but with filtered signals.

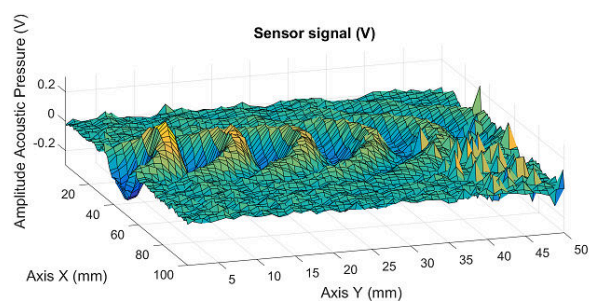


Figure 2.24: Image of the Acoustic wave in two dimensions from the setup

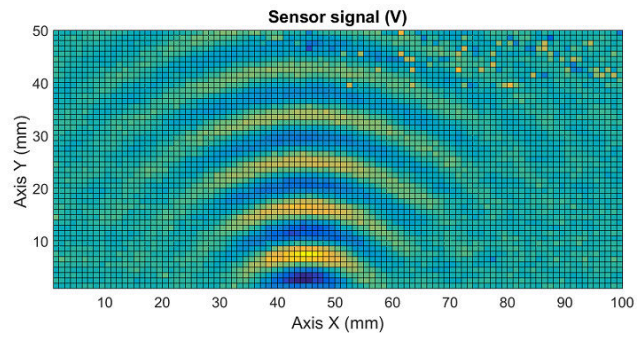


Figure 2.25: Image of the acoustic wave in the (X,Y) plane from the setup

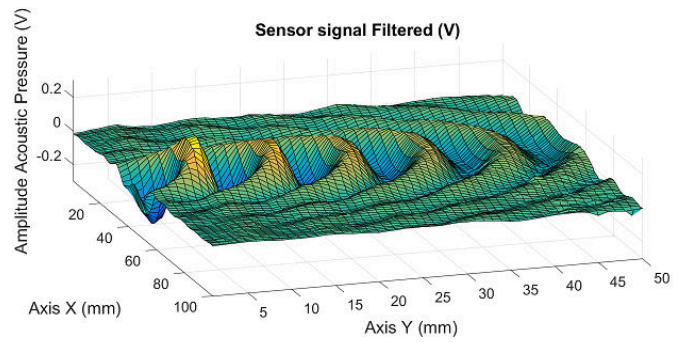


Figure 2.26: Filtered image of the acoustic wave

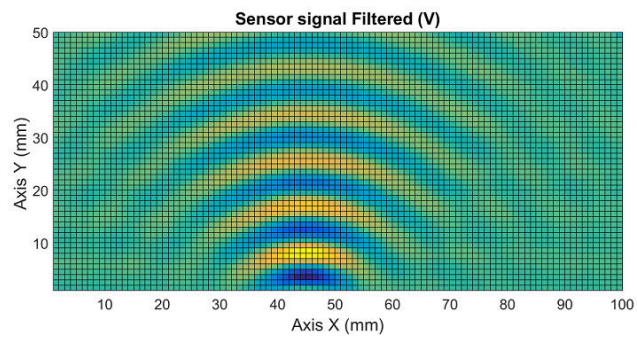
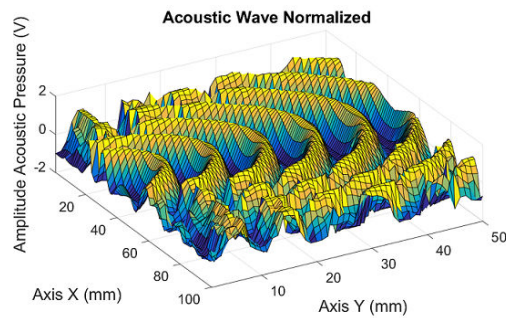


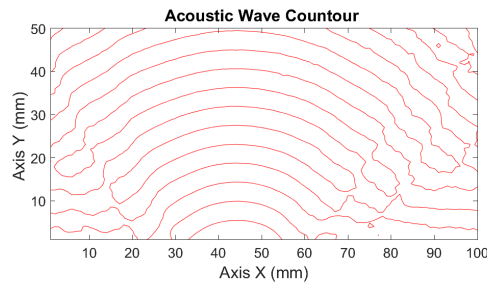
Figure 2.27: Filtered image of the acoustic wave in the (X,Y) plane

## 2.4.2 Estimation of the location of an Acoustic Source

We propose here a reflexion on how the 2D imaging of a pressure could be used to determine the location of the acoustic source that generated it. The first step consists in normalizing the amplitudes of the maxima of the wave (Fig. 2.28(a)) from which the wave contour can be automatically determined (Fig. 2.28(b)).



(a)



(b)

Figure 2.28: Step towards determination of the source of pressure wave : (a) Normalized amplitude image (b) Pressure wave contour

Thus, using Matlab's algorithm `Circle Fit` [85], we find the coordinates of the center for each of the circles that are fitted to a wavefront (Fig. 2.29). The center of the circles correspond to the position of the equivalent punctual source that would have produced the pressure wave. This one is expected to be beyond the actual vibrating surface.

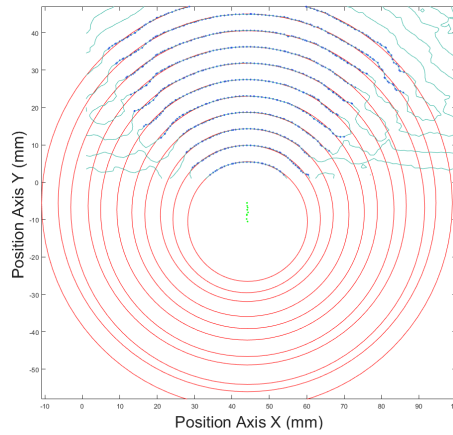


Figure 2.29: Determination of the fitting circle and their associated center (gray dots) using Circle Fit algorithm

As can be observed in Fig. 2.29, the X axis position remains pretty stable whatever the wavefront is fitted, while the Y axis position is very unstable especially for the low wavefront indexes. This can be interpreted as a consequence of the near-field to far-field transition of the acoustic wave, this one becoming actually circular only in the established far field. Looking at the evolution of the circles center with the wavefront index plotted in Fig. 2.30, we can observe an evolution towards a stable value (roughly -6 mm). This phenomenon has been observed in two consecutive measurement with different images dimension in the X axis. In Fig. 2.30, the red curve correspond to the wavefront plotted in Fig. 2.29 and it clearly shows a convergence towards the -6 mm position on the Y axis.

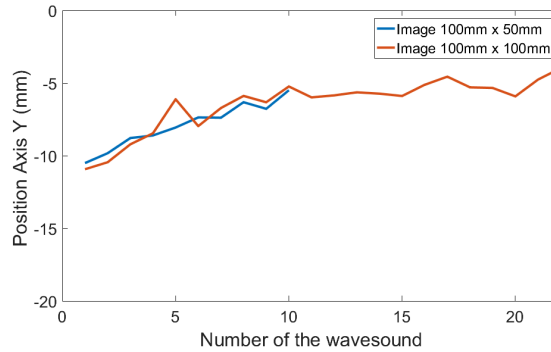


Figure 2.30: Estimated position of the acoustic origin in the Y axis

## Chapter 3

# Acoustic Tomography Imaging using Optical Feedback Interferometry

### 3.1 Introduction

The Austrian mathematician Johann Radon (1887-1956) wrote in 1917 about the determination of the integral's functions along variations in the values of their trajectory. This work was the basis of what is today known as the Radon Transform (RT) which is the principle for reconstruction and visualization of a function  $f(x, y)$  from the information obtained by the line integrals in 2D planes, or for the visualization of a function  $f(x, y, z)$  from integrals in 3D that is called Computed Tomography (CT). X-ray CT is widely used in the medical field to observe the interior of the body without contact or destruction.

Nowadays RT mathematical process is widely known in experimental sciences for different fields such as biomedical imaging, astronomy, crystallography, electron microscopy, geophysics, optics, material sciences and recently in the field of acoustics [68]-[64].

With the method described in chapter 2, it is possible to measure the integral of the refractive index change along the laser path and the refractive index is directly related to the change of pressure. With the collection of data from different directions in a same plane, we propose to image the pressure changes in this plane using a signal processing method based on the reconstruction from projections as it would be done in CT. This measurement that provides an image in the plane can lead using perpendicular translation of the sensing system to the reconstruction of acoustic fields in 3D.

In this chapter, we present a new approach for imaging pressure waves in three dimension by use of the OFI sensing scheme associated to tomographic methods. The mathematics underlying the Radon transform applied to OFI are

detailed and different experimental results are discussed.

### 3.2 Analytical Methods for Image Reconstruction in Computing Tomography

The imaging methodology proposed is a synthesis of the works of Kak and Slantay [87] who have conducted pioneering research in several areas of information processing and Dean [88], which describes the methods of reconstruction as the technique of algebraic reconstruction (ART), being a leading authority in the RT and its applications.

The method consist in the computation of 2D images from the projection along a measurement line (from the laser diode to the mirror). The superposition of these images (or slices) at different levels will result in the generation of a 3D image. Each of the 2D images are the result of a set of projections whose data are obtained under the principle of optical feedback interferometry explained in chapter two of this thesis, which we will call integral line or Line of Response (LOR), to which the CT technique has been applied. Figure 3.1(a) describes the acoustic propagation field and the scanning plane of an OFI system, while Fig 3.1(b) is the image of the slice as it should be computed using CT methods.

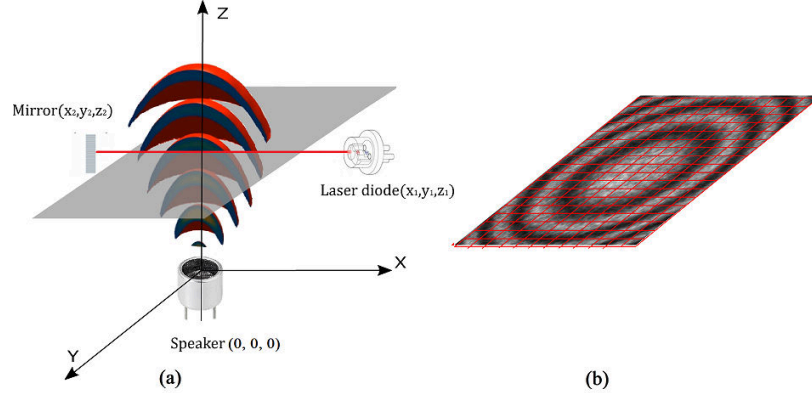


Figure 3.1: Description of the scanning principle of the 3D acoustic imaging method (a) The acoustic propagation field and the scanning plane of an OFI system. (b) The expected image of the slice.

The reconstruction of the whole 3D acoustic field  $f(x, y, z)$  is achieved by moving the scanning plane along the  $z$  axis obtaining a three-dimensional arrangement, with which all the information regarding the propagation of sound is obtained.

### 3.2.1 Computation of 2D layers

The principle of the analytical reconstruction method (the Radon Transform) requires the collection of line integrals, also called Lines of Response (LOR). In our case, the LOR are obtained by means of the optical feedback interferometry sensing and the integration of the quantity measured, the optical path difference is done along the laser beam.

As it has been detailed in the previous chapter, the expression of the laser power in the OFI acoustic imaging arrangement is

$$P_F = P_0[1 + m \cos(2\pi\nu(\tau_0 + \delta\tau))], \quad (3.1)$$

with

$$\delta\tau = 2 \int_0^{L_{\text{ext}}} \frac{\delta n(l)}{c} dl \quad (3.2)$$

Thus at each acquisition, considering the variation of  $2\pi\nu\delta\tau$  is very small compared to  $2\pi$ , after linearization of 3.1, the laser power varies of a quantity  $p$  defined as

$$p \propto \int_{\mathcal{L}} \delta n(l) dl, \quad (3.3)$$

where  $\mathcal{L}$  represents the LOR path.

Thus, the optical part of the sensing system (*id est* the laser and the mirror) are moved in both a linear translation and a rotation around the Y axis so that each LOR acquired correspond to a position  $r$  in the translation axis and an angle  $\theta$  as depicted in figure 3.2 and is then annotated  $\mathcal{L}_{r,\theta}$ .

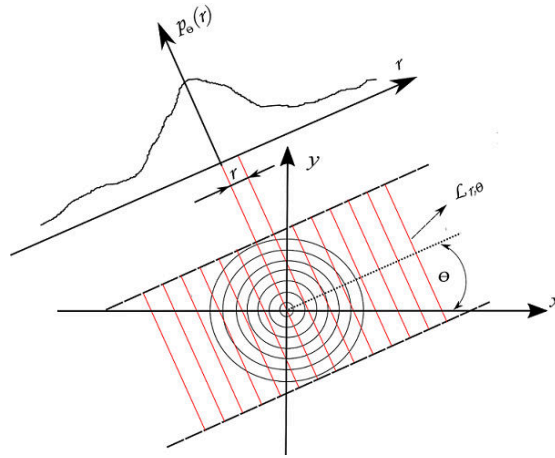


Figure 3.2: A layer in the plane  $f(x, y)$  is scanned along the angle  $\theta$  and the transmitted intensity is stored.

The variation in laser power calculated for each position of the system defined by  $\theta$  and  $r$  is :

$$p(r, \theta) \propto \int_{\mathcal{L}_{r, \theta}} n(x, y) dl, \quad (3.4)$$

where each position  $x$  and  $y$  can be defined respectively by

$$x = r \cos \theta - l \sin \theta \text{ and } z = r \sin \theta + l \cos \theta, \quad (3.5)$$

so that

$$dl = \frac{dx}{\sin \theta}, \quad (3.6)$$

and

$$y = \frac{r}{\sin \theta} - x \frac{\cos \theta}{\sin \theta}. \quad (3.7)$$

Thus, considering the LOR is much larger than the object to be imaged, equation (3.4) can be written as

$$p(r, \theta) \propto \frac{1}{\sin \theta} \int_{-\infty}^{+\infty} n(x, \frac{r}{\sin \theta} - x \frac{\cos \theta}{\sin \theta}) dx. \quad (3.8)$$

Considering the properties of the Dirac function

$$f(x, y') = \int_{-\infty}^{+\infty} f(x, y) \delta y - y' dz, \quad (3.9)$$

and

$$\delta\left(\frac{x}{b}\right) = b\delta(x), \quad (3.10)$$

the equation (3.8) becomes

$$p(r, \theta) \propto \iint_{-\infty}^{+\infty} n(x, y) \delta(x \cos \theta + y \sin \theta - r) dx dy. \quad (3.11)$$

Considering a complete collection of line integrals  $p(r, \theta)$  computed from a function  $n(x, y)$ , the RT is the mathematical transformation allowing to go from  $n(x, y)$  to  $p(r, \theta)$  as

$$n(x, y) \text{ with } x, y \in (-\infty, +\infty) \xrightarrow{\text{Radon}} p(r, \theta) \text{ with } \theta \in [0, \pi] \text{ and } r \in (-\infty, \infty). \quad (3.12)$$

Therefore, the problem of reconstructing 2D images is to recover  $n(x, y)$  through the acquired projections  $p(r, \theta)$ .

### 3.2.2 Sinogram

If the function  $p(r, \theta)$  is plotted over a two axis referential (one in  $r$  and the other in  $\theta$ ), the figure that is produced is called sinogram. For example, the sinogram of two 2D Dirac ( $\delta(x_0, y_0)$  and  $\delta(x_0, 0)$ ) are plotted in Fig. 3.3.

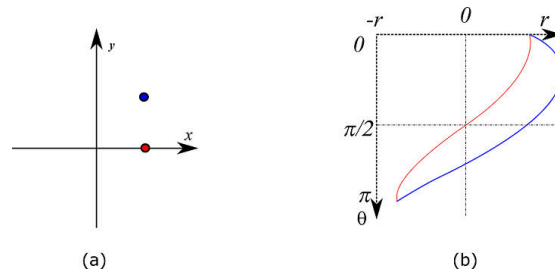


Figure 3.3: Principle of the sinogram (a) Cross-section of 2D Diracs (blue and red) (b) Corresponding sinogram.

Thus graphically, the RT consist in transforming figure 3.3(a) into figure 3.3(b) while the inverse RT is the reciprocal operation. The latest transformation is performed using differnt methods and algorithms amongst which the backprojection approach with the ART algorithm is the most common.

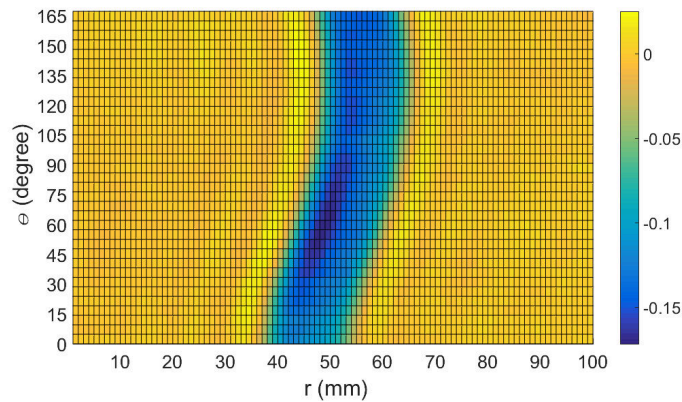


Figure 3.4: Sinogram for one circular wave.

### 3.3 Backprojection

Among the various method that perform the reverse of the RT we choose to use the one known as Backprojection. This type of operation is widely used

in the reconstruction of tomographic images. As every discretized system to its simplest form loses information, this procedure does not recover the original image  $n(x, y)$ , but produces instead a fuzzy or approximate version,  $n_b(x, y)$  that is called the Laminogram or Layergram as described in (3.13)

$$n_b(x, y) = \int_0^\pi p(r, \theta) \cdot (x \cos \theta + y \sin \theta) d\theta. \quad (3.13)$$

Under ideal conditions (without any attenuations), the projections that are acquired at angles between  $\pi$  and  $2\pi$  radians do not provide new information, since the acquired projections are symmetric with those at angles between 0 and  $\pi$ .

The fact that the laminogram is not the exact image of the original object is due to the discontinuities in the object or at the object surfaces. However, dealing with pressure waves, there are no possible discontinuities at the scale of the laser wavelength, thus in our case,  $n_b(x, y)$  will resemble to  $n(x, y)$  without further signal processing.

### 3.3.1 Algebraic Reconstruction Technique (ART)

In the experimental acquisition of the projections, the number of point  $r_j$  is limited as well as the number of projection angles  $\theta_k$ . Thus, for a given point  $p_{\theta_k}(r_j)$  in (3.13), the backprojection operation is called the summation algorithm as the integral is replaced by a sum :

$$n_b(x, y) = \sum_{k=1}^{N_p} p_{\theta_k}(r_j) \cdot (x \cos \theta_k + y \sin \theta_k). \quad (3.14)$$

Where  $N_p$  is the number of projections angles from 0 to  $\pi$  radians , and  $r_j = x \cos \theta_k + y \sin \theta_k$ .

For a better imaging, we use a constant step  $\pi/N_p$  with  $\theta_k \in \left[0, \frac{N_p-1}{N_p}\pi\right]$ .

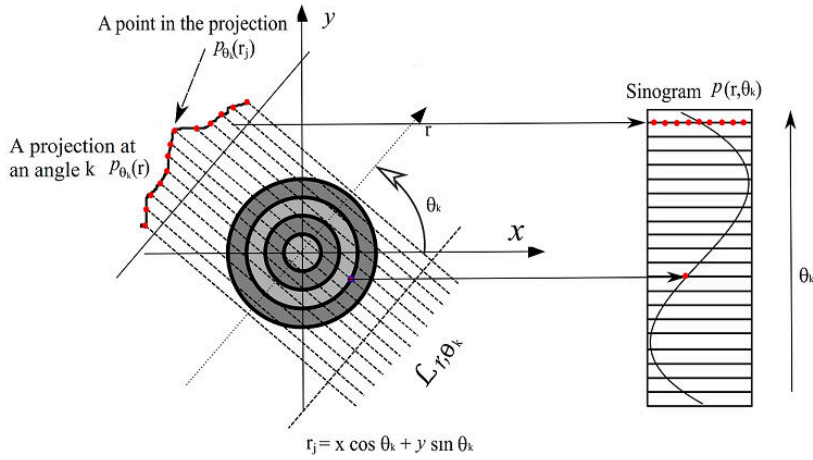


Figure 3.5: Radon Transform schematic.

Therefore, an infinite number of projections are theoretically required to perfectly reconstruct an object. If the number of projections is small the reconstructed image will be poor as can be observed in the simulated plot of Fig. 3.6 [89].

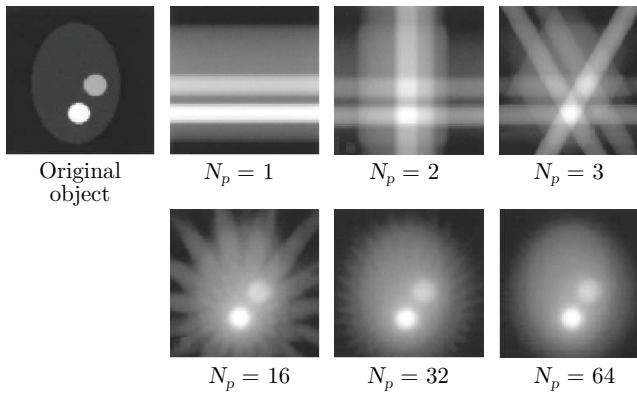


Figure 3.6: Reconstructed slice of two circular objects computed from 1 to 64 projection angles [89]

### 3.4 Setup Design

The experimental acquisition of the lines of response (LOR)  $\mathcal{L}_{r, \theta}$  was carried out through a modification of the design of the setup used in chapter 2 as a rotational system is added to control the projection angle  $\theta$  while the two existing translation axes were used to achieve the displacement along the parameter

$r$  and eventually the  $z$  axis.

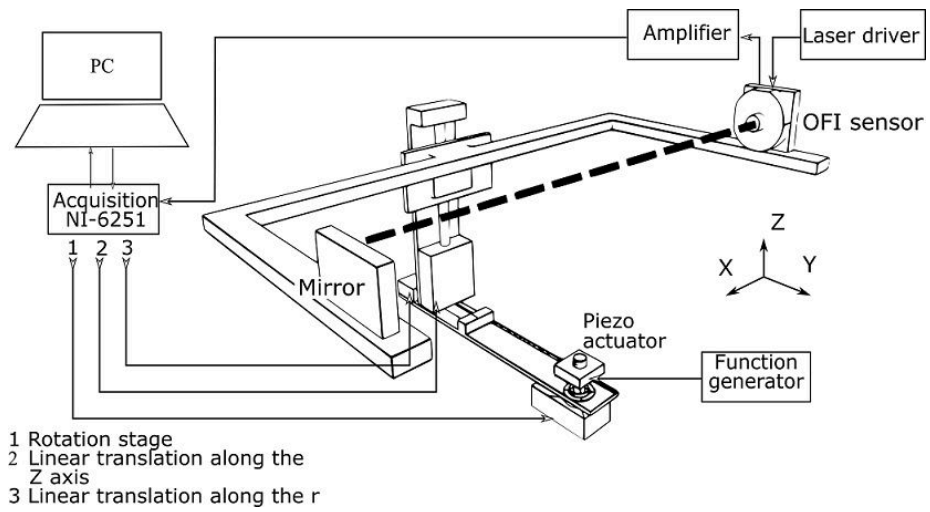


Figure 3.7: Design of the Acoustic 3D imaging system by Optical Feedback Interferometry.

Both translation and rotation stages were Zaber products (T-LSR300A-KT03). A dedicated control software was developed using Labview.

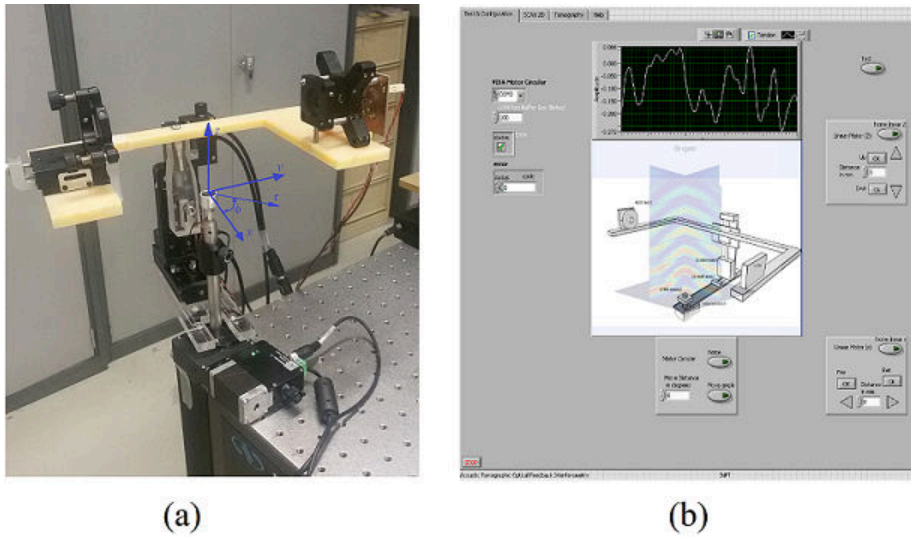


Figure 3.8: Actual experimental setup (a) Photography of the experimental setup (b) GUI of the control software

A calibration is performed to ensure that at mid course, the translation axis along  $r$  passes through the rotation axis of the system (see Fig 3.9). A rotation every 45 degrees is sufficient to validate the good alignment that is mandatory to obtain a realistic image of the acoustic wave.

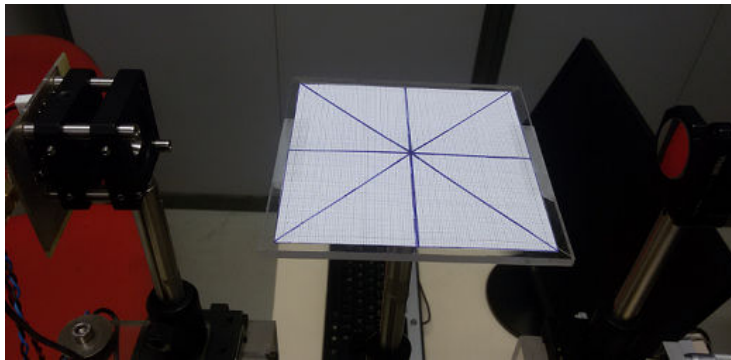


Figure 3.9: Calibration of the rotation centre.

Furthermore, the next step is to align the mirror with the laser in order to obtain the better feedback signal. This procedure was discussed in chapter 2. The acquisition and the data processing for each LOR are the same that were

exposed in section 2.2.2 of chapter 2.

In its standard configuration, the system is developed with the intention of visualizing acoustic pressure in a scanning area of 100 mm by 100 mm with a step of 1 mm between each LOR. Therefore, each projection at angle  $\theta$  is composed by 100 points while the increment of  $\theta$  is done with a step of  $5^\circ$  from 0 to  $175^\circ$ .

The following figures (Fig. 3.10 - 3.13) show the projection  $p_{\theta_k}(r)$  induced by the variation of the acoustic pressure produced by two similar piezo-actuators (KPUS-40T-16T-K768) driven by the same electrical signal. The projection were acquired respectively at 0, 45, 90 and  $135^\circ$  at the same reference time with respect to the electrical signal period, while the laser scanning plane was roughly 1 mm above the acoustic sources.

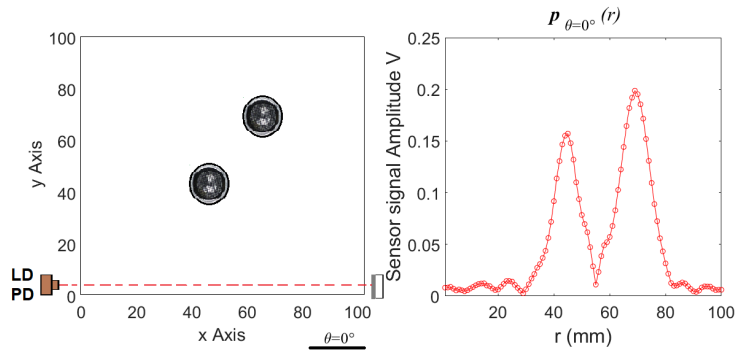


Figure 3.10: Projection at  $\theta = 0^\circ$  acquired with 2 piezo-actuators (a) Relative position of the LOR with the speakers , (b) projection function  $p_{\theta=0^\circ}(r)$

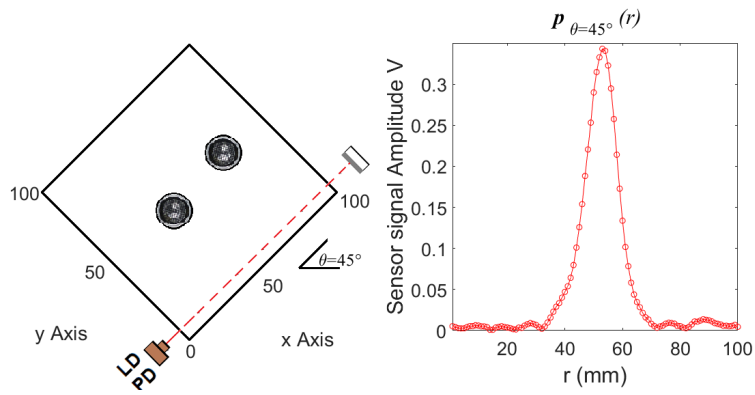


Figure 3.11: Projection at  $\theta = 45^\circ$  acquired with 2 piezo-actuators (a) Relative position of the LOR with the speakers , (b) projection function  $p_{\theta=45^\circ}(r)$

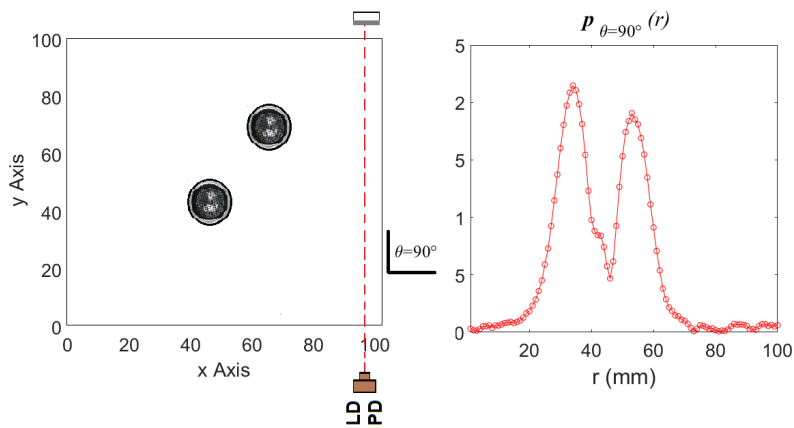


Figure 3.12: Projection at  $\theta = 90^\circ$  acquired with 2 piezo-actuators (a) Relative position of the LOR with the speakers , (b) projection function  $p_{\theta=90^\circ}(r)$

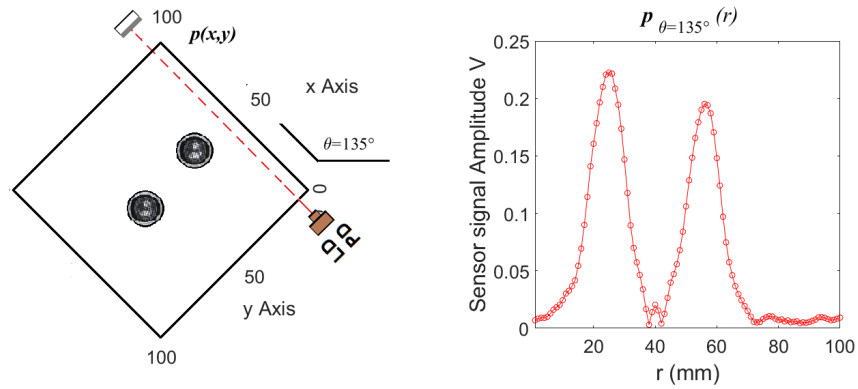


Figure 3.13: Projection at  $\theta = 135^\circ$  acquired with 2 piezo-actuators (a) Relative position of the LOR with the speakers , (b) projection function  $p_{\theta=135^\circ}(r)$

With the 36 projection functions acquired by the system, the Sinogram is created. In this case, the resolution of the image is 36 lines ( $\theta$ ) per 100 columns ( $r$ ).

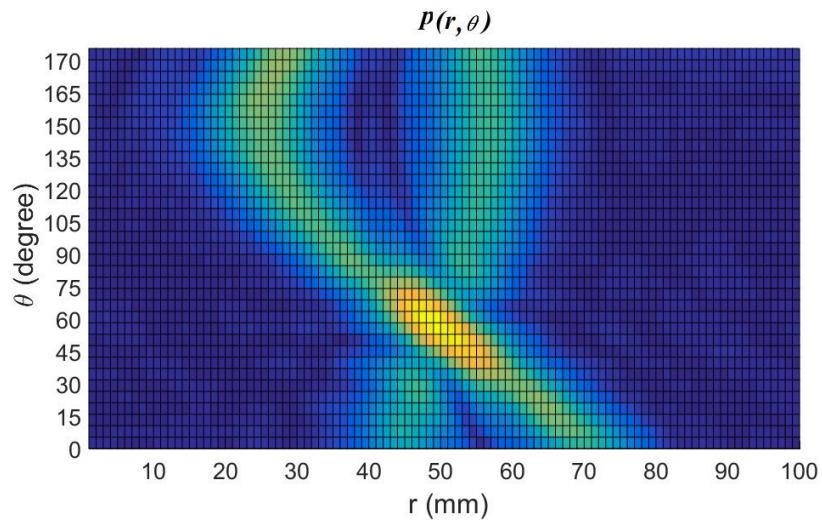


Figure 3.14: Sinogram acquired for the two speakers

In Fig. 3.14, we observe the quasi sinusoidal shape for each of the speaker as expected from theory (see Fig. 3.3). However, as the central speaker is almost aligned with the rotation axis, it does not have much variation in the sinogram, while the other speaker, as it is excentered show a stronger shift.

### 3.4.1 Backprojection Reconstruction

In order to detail the process of image reconstruction using the backprojection algorithm as it has been developed in Matlab, we present here step by step a basic reconstruction from the 4 projection angles as depicted in figures Fig. 3.10 to 3.13.

$$n_b(x, y) = \frac{1}{N_p} \sum_{k=1}^{N_p} n_{(b, \theta_k)}(x, y) \quad (3.15)$$

and since in this first case  $N_p = 1$ , Fig. 3.15 (c1) present the same image as Fig.3.15 (b1). The coefficient  $1/N_p$  is added here so that all figures represent a similar amplitude.

Figure 3.15 (a2) presents the projection that is acquired with an angle  $\theta = \frac{\pi}{4}$  while the reconstruction is done in Fig. 3.15 (b2) with this single projection. As one can see, with comparison to the previous reconstruction at  $\theta = 0$ , the reconstruction is tilted by  $\frac{\pi}{4}$ . Fig. 3.15(c2) shows the sum of reconstructions as described in (3.15) for  $N_p = 2$ .

Similar methodology is applied for  $\theta = \frac{\pi}{2}$  and  $\theta = \frac{3\pi}{4}$  in Fig. 3.15 (a3) and Fig. 3.15 (a4) with  $N_p = 3$  and  $N_p = 4$  respectively.

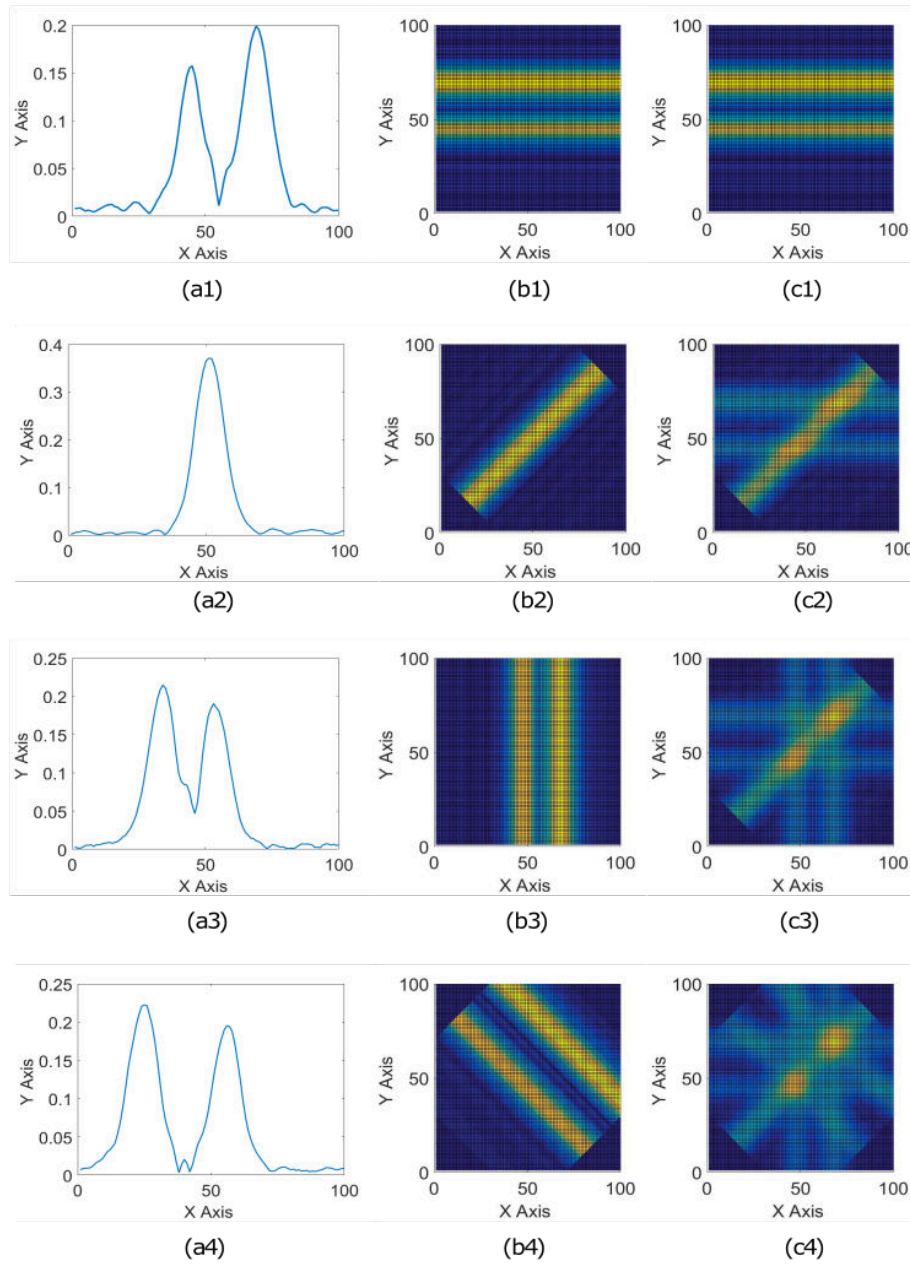


Figure 3.15: Backprojection reconstruction in 4 steps for 4 projections, (a1) Projection at  $\theta = 0$ , (a2) Projection at  $\theta = \frac{\pi}{4}$ , (a3) Projection at  $\theta = \pi$ , (a4) Projection at  $\theta = \frac{3\pi}{4}$ , (b1) to (b4) reconstruction of the unique projection for each angle, (c1) sum of  $N_p = 1$  reconstructions, (c2) sum of  $N_p = 2$  reconstructions, (c3) sum of  $N_p = 3$  reconstructions, (c4) sum of  $N_p = 4$  reconstructions.

As can be observed in Fig. 3.15(c4) the reconstruction from 4 different projection angles distributed over  $\pi$  provides an already resembling image of what can be expected to be the pressure change at the vicinity of the speakers. A 3D visualisation with perspective offers an even better appreciation of the reconstruction (Fig. 3.16).

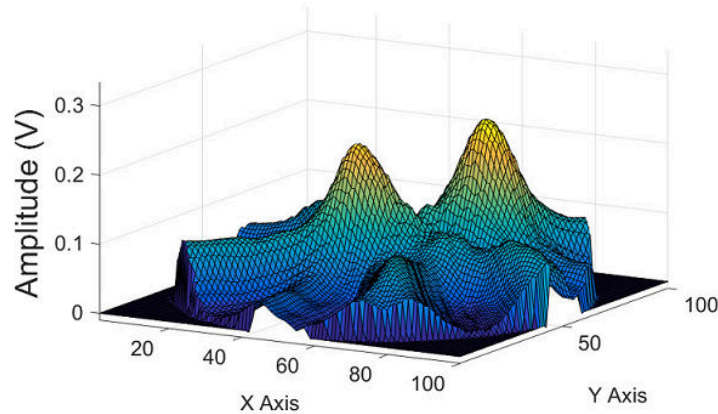


Figure 3.16: Reconstructed image  $n(x,y)$  with 4 projection (view with perspective)

Thus to improve the image, it is necessary to increase the number of projection angles. In the following figures, the result of image Fig. 3.17 (a), (b), (c) with 9, 18 and 36 projections respectively are shown.

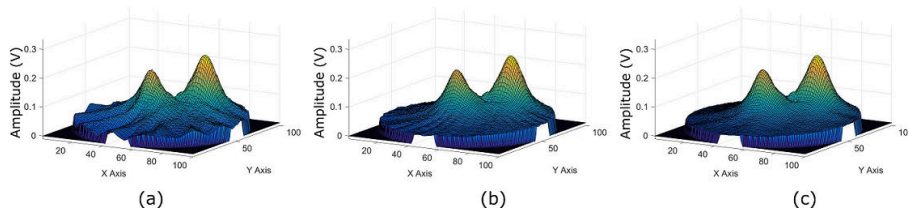


Figure 3.17: Reconstructed image  $n(x,y)$  with (a) 9 projections, (b) 18 projections and (c) 36 projections

Similarly to what was done in chapter 2, a band-pass filter (38-42 kHz) is implemented in Matlab in order to obtain an even smoother image. the comparison between raw data and filtered data image reconstruction is presented in Fig.3.18 where we can indeed observe a smoother image once the filter is applied.

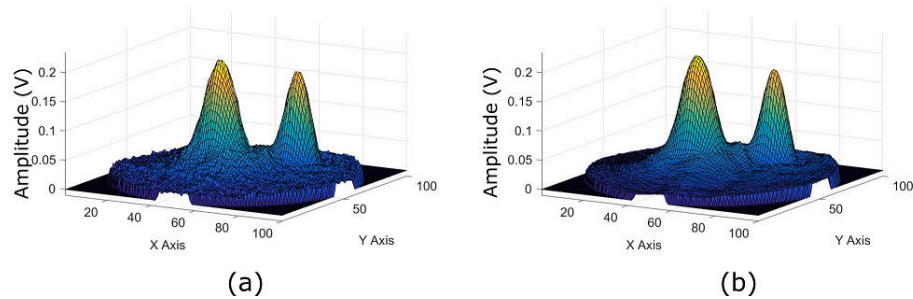


Figure 3.18: Reconstructed image  $n(x, y)$  from 36 projections with (a) raw data and (b) filtered data

### 3.4.2 Backprojection Reconstruction by Matlab

In the late period of this PhD we discovered that Matlab is proposing a complete Inverse Radon transform called "*Iradon*". This method assumes that the center of rotation is the centre point of the projections and that the variable  $\theta$  describes the angles (in degrees) at which the projections were taken. It can be either a vector containing the angles or a scalar specifying the incremental angle between projections. *Iradon* uses the filtered backprojection algorithm to perform the Inverse Radon Transform. The filter is designed directly in the frequency domain and then applied to the FFT of the projections. Since our own algorithm was already designed we decided to test-bench it against Matlab's reference.

In addition to the inverse Radon transform Matlab *Iradon* proposes several types of filters:

- Ram-Lak - The cropped Ram-Lak or ramp filter (default).
- Shepp-Logan - The Shepp-Logan filter multiplies the Ram-Lak filter by a sinc function.
- Cosine - The cosine filter multiplies the Ram-Lak filter by a cosine function.
- Hamming - The Hamming filter multiplies the Ram-Lak filter by a Hamming window.
- Hann - The Hann filter multiplies the Ram-Lak filter by a Hann window.
- none - No filtering is performed.

Figure 3.19, the reconstruction from the very same 36 projections raw data (*id est* without the bandpass filter) acquired with the two piezo-actuators (see Fig. 3.17) with each type of filter are plotted.

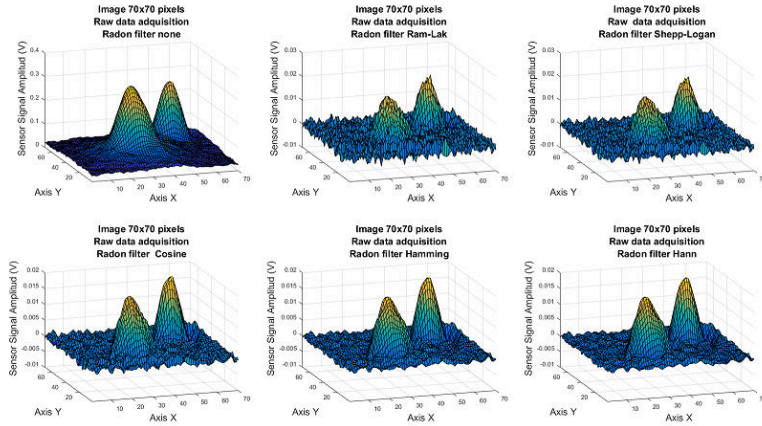


Figure 3.19: Image reconstructed from acquired data projection b Matlab *Iraddon* function.

As we can see in these images, the reconstruction done by Matlab is limited to a 70x70 size image, while the reconstructed image with our algorithm is 100x100 pixels. In our algorithm, in order to avoid the edge effects, a circular mask was added to the figures 3.17 so that any pixel outside the mask has a value of zero. Matlab *Iraddon* applies a stronger limitation as it keeps only the square image that would fit in our circular mask. In order to compare Matlab *Iraddon* to our algorithm, we had to truncate the previous plotted data thus to obtain a similar size 70x70 pixels as can be observed in Fig. 3.20(b).

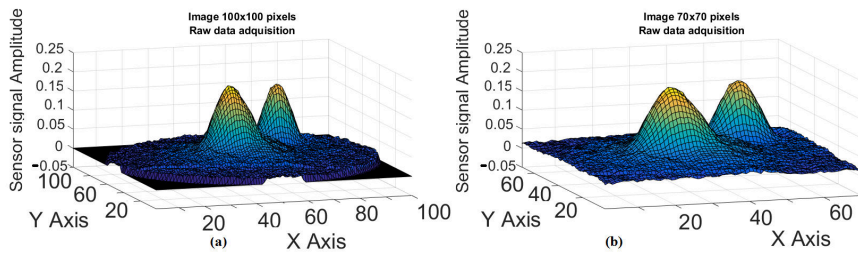


Figure 3.20: Image reconstructed from acquired projections with our own algorithm (a) original image 100x100, (b) truncated image 70x70.

In order to compare our image we applied a calculation of the mean square error (MSE) between our matrix of pixels  $s(x,y)$  and those computed from

Matlab *Iraddon*  $\tilde{s}(x, y)$

$$\text{MSE} = \frac{1}{mn} \sum_{x=1}^m \sum_{y=1}^n [s(x, y) - \tilde{s}(x, y)]^2. \quad (3.16)$$

All reconstructed images have a MSE of 0.262% , apart, as could be expected from the plots of Fig. 3.19, for the one with no filter (none) for which the MSE is even lower at 0.093%. It is not very clear to us why the introduction of the filtering to the *Iraddon* function induces a visible degradation of the reconstruction from our measurements. However, since these filters are designed to reduce the effect of brutal step at the interface of the imaged objects and as our object (the acoustic wave) does not have any discontinuity it is not very surprising that the filter does not lead to any improvement of the reconstructed image.

The comparison between Matlab *Iraddon* and our own algorithm has been performed for band-pass filtered data showing even better MSE and no further benefits of the reconstruction filters.

### 3.5 Acoustic tomography imaging experimentation

In this section we present a set of experiments that have been designed to highlight the performances and limits of the novel imaging system that we have labelled ATOFI (Acoustic Tomography by OFI). In addition to what has been presented so far, multiples slices at different altitudes have been acquired. The imaging system provides data in a volume with a voxel resolution of 1.0 x 1.0 x 1.0 mm, and contains values that represent the acoustic pressure change in time, thus leading in reality to a 4D imaging system.

The ATOFI setup with this resolution and considering the displacement range of the translation stages scans 500k pixels, representing a rectangular cuboid volume of 100x100x50 mm.

Amongst the numerous experimental arrangements that were tested in this thesis, we present here, at first the detailed results from a unique acoustic source, then the interferences between two sources in various configurations and eventually an imaging of the Huygens-Fresnel principle in acoustics showing that numerous punctual sources behave as a unique source of larger diameter.

#### 3.5.1 Acoustic 3D imaging of a unique source

The configuration of the setup developed for the acquisition of computerized tomography image has been explained throughout this chapter. In this arrangement, the sound field is generated by an ultrasonic piezoelectric KPUS-40T-16T-K768 driven by a sinusoidal voltage of 10 Vp-p at 40 kHz frequency. The setup is the same as depicted in Fig. 3.7.

Figure 3.21 (a) and (b) show the reconstruction computed for a slice located at roughly 1 mm above the sound source for a time  $t_0$  and  $t_0 + T/2$  respectively,

while Fig. 3.21(b) and (c) show for the same times the slice located roughly to 50 mm above the source.

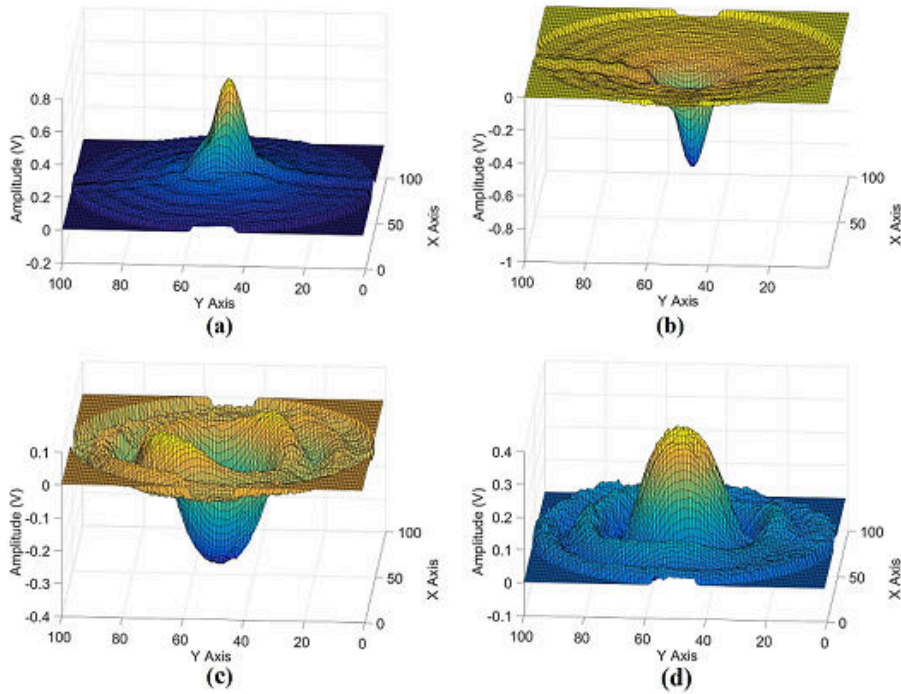


Figure 3.21: Acoustic field in the time domain of the one source at 40 kHz, (a) at an altitude of 1 mm and  $t = t_0$ , (b) at an altitude of 1 mm and  $t = t_0 + T/2$ , at an altitude of 50 mm and  $t = t_0$ , (d) at an altitude of 50 mm and  $t = t_0 + T/2$ .

While at 1 mm only one single peak is observed, at 50 mm, lateral propagation of the acoustic wave is imaged as pressure rings surrounds the main peak.

By measuring the amplitude of the bin corresponding to 40 kHz in the signal spectrum computed by FFT, we can obtain a representation of the average acoustic pressure variation distribution in space. Figure 3.22 shows the comparison of the distribution at 1 mm and 50 mm.

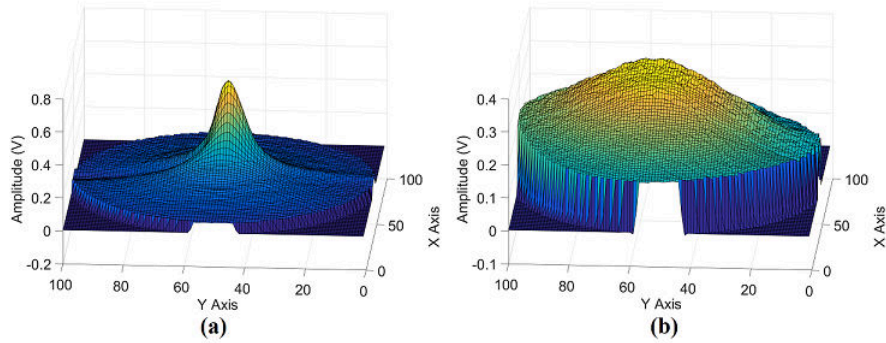


Figure 3.22: Average acoustic pressure variation distribution based on the 40 kHz bin amplitude in the signal FFT, at (a) altitude of 1 mm and (b) altitude of 50 mm.

The representation of volumes in thesis manuscripts not being an easy task we propose first to depict the 3D image by two vertical sections orthogonal one to each other. Figure 3.23 presents these 3D visualization for the reconstructed image in time ( $t = t_0$ ) and in average pressure variation through the amplitude of the 40 kHz bin.

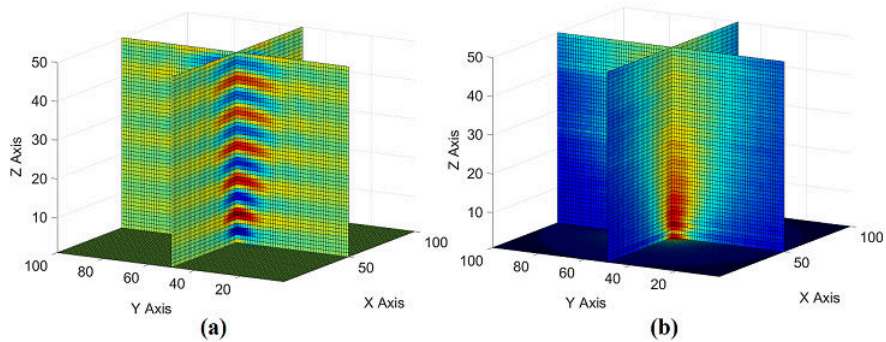


Figure 3.23: Acoustic field in 3D of the one sources at 40 kHz, (a) 3D Visual representation in time domain (b) 3D Visual representation in FFT domain.

The volume rendering (VR) representation is an alternative solution. It is a set of techniques available in Matlab that are used to display on a 2D projection a 3D data set. The VR can be seen as extracting the isosurfaces (areas of equal values) in the volume and representing them as polygonal meshes in a 3 axis plot. In Fig. 3.24, time acquisition ( $t = t_0$  and  $t = t_0 + T/2$ ) are plotted with empirical values chosen for the isosurfaces allowing for an explicit visualization of the acoustic propagation in the volume.

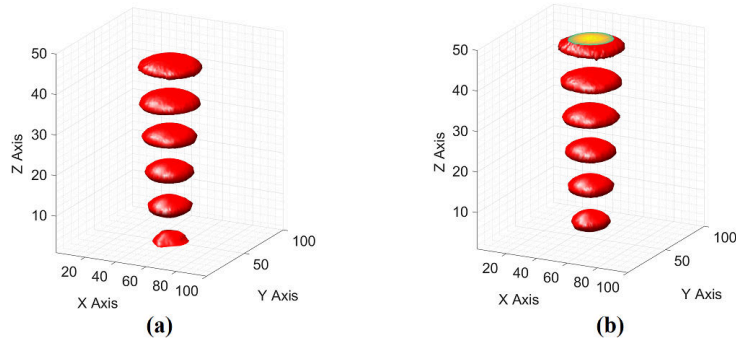


Figure 3.24: 3D visualization of the acoustic field in time domain of one acoustic source at 40 kHz using Matlab VR tool. (a)  $t = t_0$  and (b)  $t = t_0 + T/2$ .

Similar visualization approach is applied to the averaged pressure changes (40 kHz bin amplitude) in Fig. 3.25(b) together with the display of 6 slices distributed from 1 mm to 50 mm altitudes with a step of 10 mm (Fig 3.25 (a)).

As can be seen on the plots of Fig. 3.24(b) and 3.25(b), the average pressure change isosurface is larger as it is more distant from the acoustic source, which is to be expected since the pressure variation is more condensed near the source as it was already observed in chapter 2. Also, and in good agreement with the 2D plots of chapter 2, the average pressure variation distribution exhibits small variations with a spatial periodicity close to  $\lambda_s/2$ .

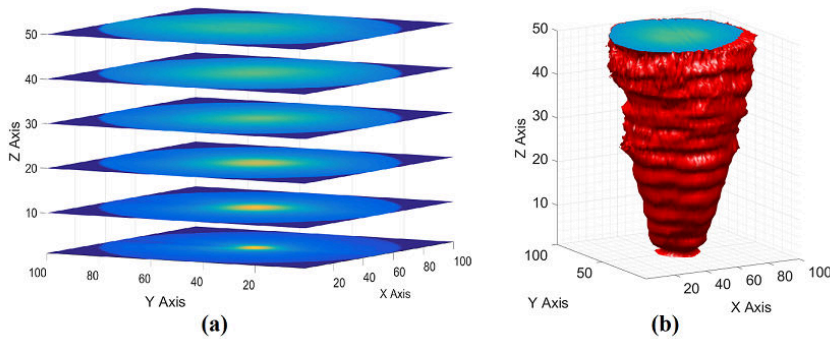


Figure 3.25: Acoustic field in the FFT domain of the four sources at 40 kHz, (a) Visual representation at 6 specific levels (1, 10, 20, 30, 40, 50 mm) (b) Volumetric representation of the acoustic pressure in a volume of 100 x 100 x 50 mm.

## 3.5.2 Interferences

### Interferences with two coplanar sources in phase

In the following arrangement, we set two KPUS-40T-16T-K768 ultrasonic piezoelectric transmitters that are displayed on the same horizontal plane. They are actuated by the same sinusoidal signal of 10 V<sub>p-p</sub> at frequency 40 kHz. The propagation axis is perpendicular to the optical propagation direction as shown in the figure 3.26. The distance between the two sources is roughly 28 mm.

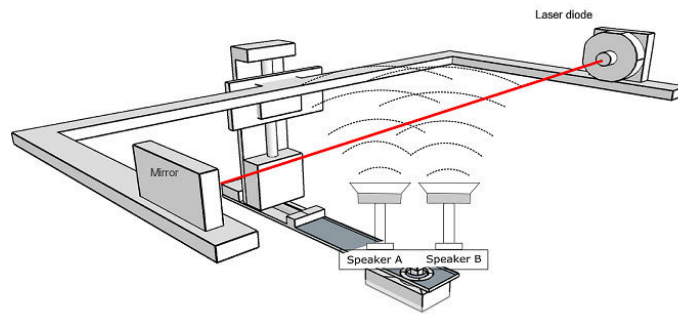


Figure 3.26: Schematic of the Acoustic Tomography Optical Feedback Interferometry (ATOFI) setup with two acoustic source speakers.

The plots of Fig. 3.27(a) and (b) show the result of the reconstruction for a slice located at 1 mm from the sources plane for  $t = t_0$  and  $t = t_0 + T/2$ . Similarly, the plots of Fig. 3.27(c) and (d) show the reconstructed slice at an altitude of 50 mm.

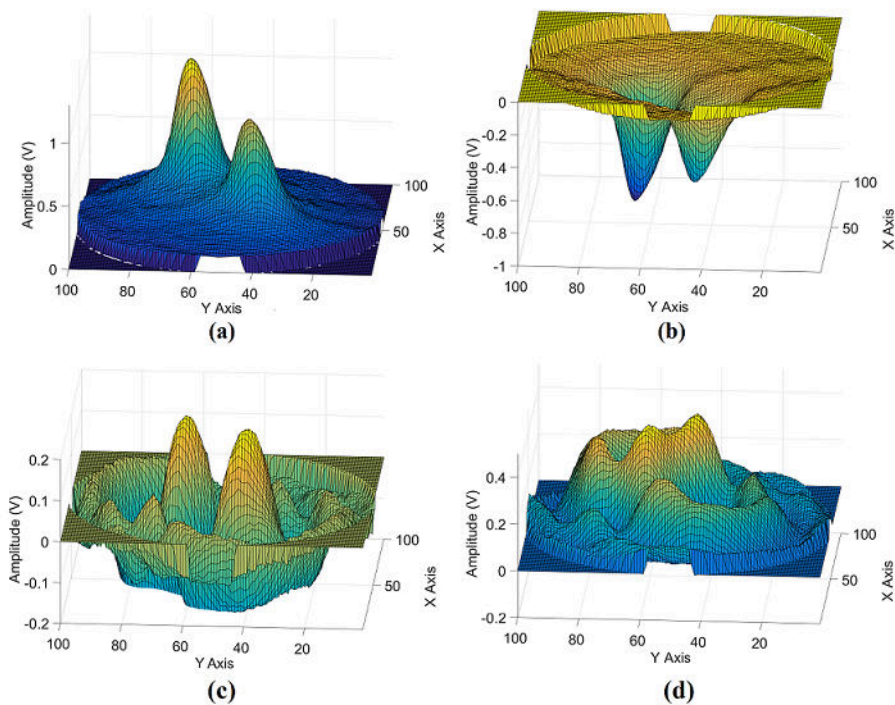


Figure 3.27: Acoustic field in time domain of the two coplanar sources in phase. (a) altitude of 1 mm and  $t = t_0$ , (b) altitude of 1 mm and  $t = t_0 + T/2$ , (c) altitude of 50 mm and  $t = t_0$ , (d) altitude of 50 mm and  $t = t_0 + T/2$ .

Displaying the reconstructed 3D image with the two orthogonal vertical planes, one can observe that the maximum of pressure wave variation is located along the vertical axis of equi-distance between the two speakers. This effect is noticeable in both the time and frequency domain (amplitude of the 40 kHz bin).

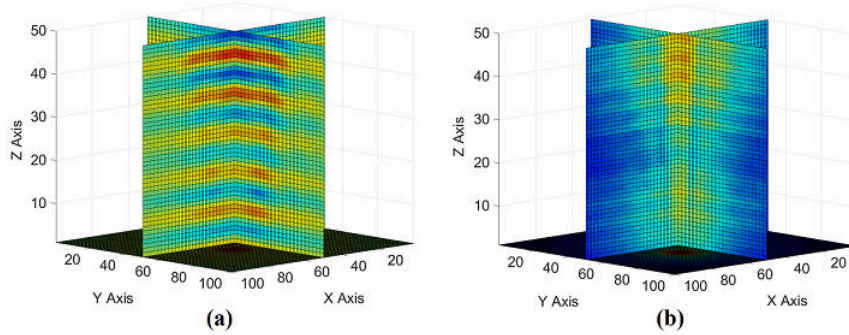


Figure 3.28: Acoustic field in 3D of the two sources at 40 kHz, (a) 3D Visual representation in time domain (b) 3D Visual representation in FFT domain.

Through the volume rendering (Fig. 3.29), we observe the same phenomenon both in time ( $t = t_0$ ) and frequency.

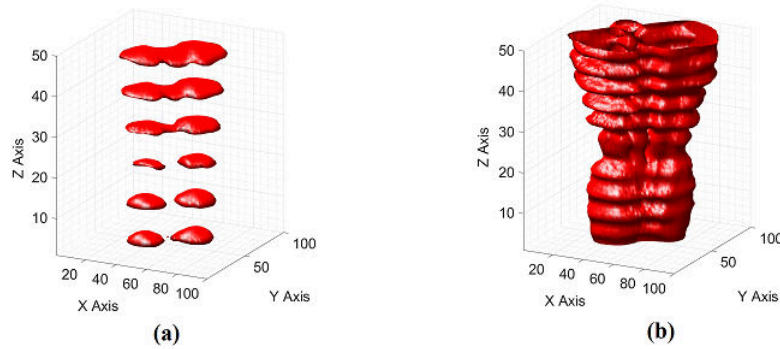


Figure 3.29: Acoustic field in the time domain of the four acoustic sources at 40 kHz, in volumetric representation, in (a)  $t = t_0$  and (b)  $t = t_0 + T/2$ .

It is interesting to observe that the constructive interference seems to occur only at altitudes higher than 20 mm and is more clearly visible at the higher altitudes. This is most likely due to the distance between the two actuators as in Fig. 3.29 (a), we clearly see that up to 20 mm of altitude, both wave do not really propagate in the same volume.

### Interferences with two coplanar sources in phase oppotisiton

With the very same arrangement than for the previous experiment, we have driven the two piezo-actuators with  $\pi$  shifted sinusoidal signals at 40 kHz as

can be shown in Fig. 3.30(a) in which the speaker A has negative pressure while the speaker B has positive pressure. The corresponding slice was acquired at an altitude of roughly 1 mm while Fig. 3.30(b) plot represents at the same  $t = t_0$  the slice at 50 mm where, due to the wave complexity, the image interpretation is very complex.

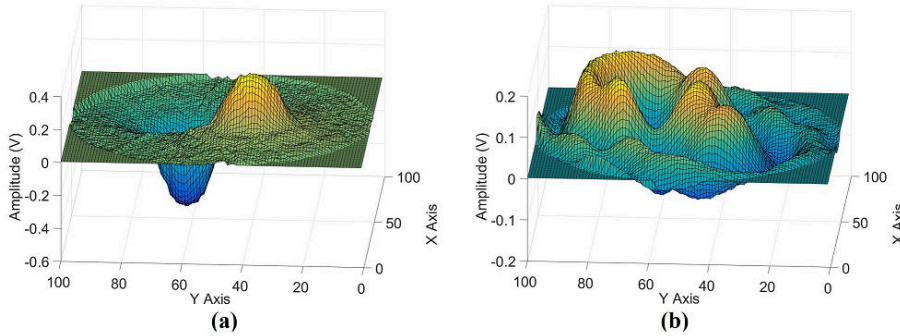


Figure 3.30: Acoustic field reconstructed slice in time domain of two sources at 40 kHz in phase opposition (a) at an altitude of 1 mm and (b) at an altitude of 50 mm.

In the actual 3D images, with the two orthogonal planes, the destructive interference that is expected to arise where the two waves meet (*id est* at the equidistant vertical line from each source), can be clearly observed both in time domain ( $t = t_0$ , Fig. 3.32(a)) or in pressure distribution (using the 40 kHz bin amplitude, Fig. 3.32(b)).

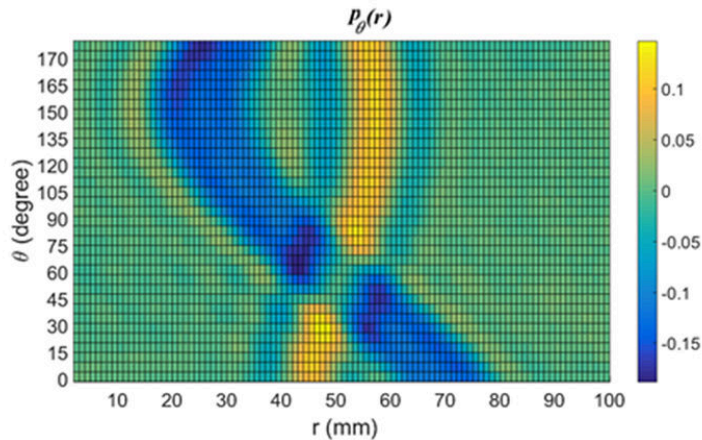


Figure 3.31: Sinogram acquired for the two speakers for destructive interference.

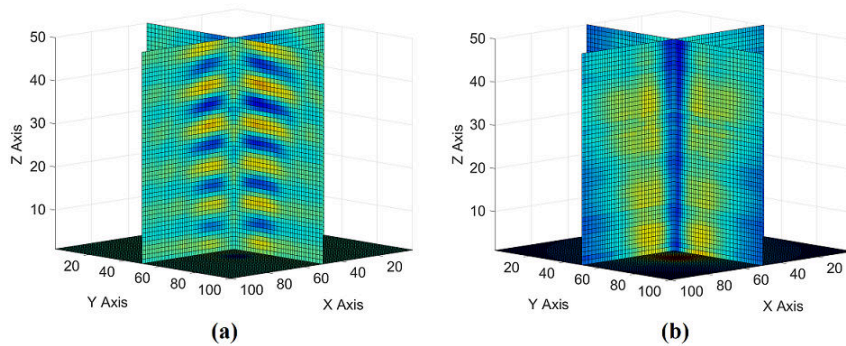


Figure 3.32: Acoustic field in 3D visualization of the two sources at 40 kHz, (a) in time domain (b) in frequency domain.

In this case, the images that would be obtained using Matlab VR rendering would be of no help to see this destructive interference effect since it would occur inside the visible mesh surface of the plot.

For that reason, we manage to open the volume created by the VR rendering. In the image of Fig. 3.33(a) we have kept only the back part of the external isosurface in order to observe the internal isosurface. As can be seen, this internal isosurface has the shape of a vertical cylinder that indicates the lower pressure variation induced by the destructive interference. As another possible visualization of the phenomenon, Fig. 3.33(b) shows the VR image cutted in two by the half while the rest of the pressure change distribution inside the isosurfaces is kept visible in the remaining half. We believe the quality of this image to be absolutely remarkable and very impressive demonstration of the ATOFI imager system performance.

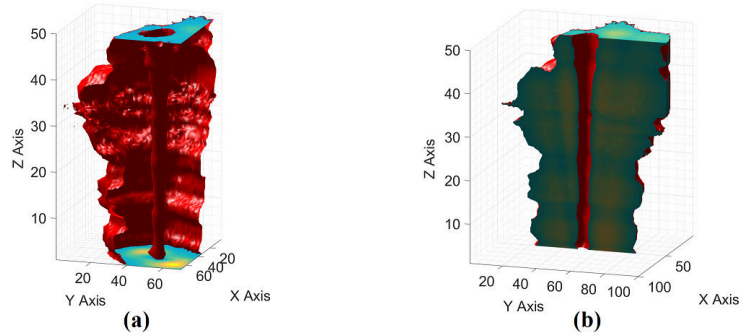


Figure 3.33: Acoustic field in the frequency domain of the two sources at frequency 40 kHz, (a) Rendering volumetric of the destructive interference (b) volumetric representation of the acoustic pressure sliced along the vertical plane.

### 3.5.3 Stationary wave

In this experiment, the stationary wave is produced by the association of two speakers emitting in opposite directions and set on the same propagation axis at a distance of 100 mm as shown in Fig. 3.34. The two speakers are the ultrasonic piezoelectric transmitter KPUS-40T-16T-K768 driven by a sinusoidal voltage of 10 V<sub>p-p</sub> amplitude at 40 kHz frequency. The observation volume is delimited by 15 slices of images of 100 x 100 pixels.

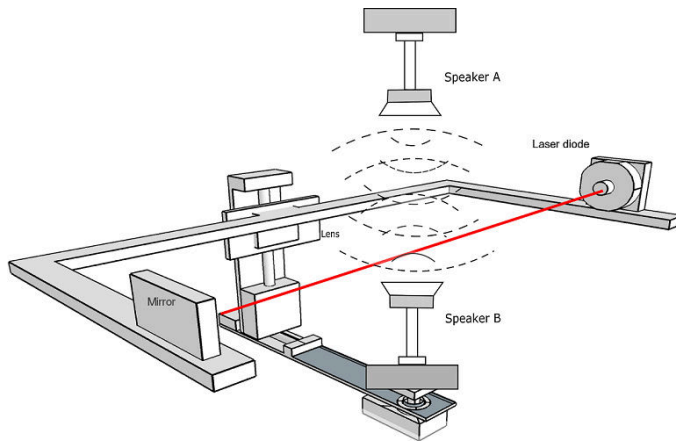


Figure 3.34: Schematic of the ATOFI experimental setup for a stationary wave produced by two identical sources in opposite direction.

In this case, the distance between the two opposing speakers was 100 mm,

however the data acquired to visualize the standing wave in this experiment was 15 mm with a resolution of 1 mm, equivalent to two times the wavelength  $\lambda_s$  of the sound.

The behavior of the standing acoustic wave in the frequency domain (FFT) is shown in two different levels that correspond to the position of a node and an antinode of the standing wave in Fig. 3.35.

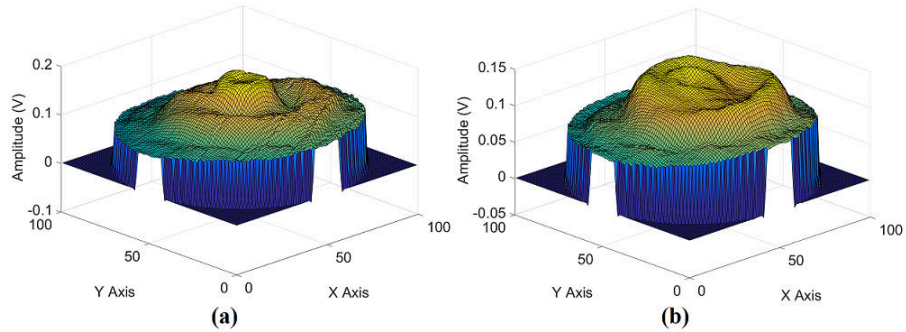


Figure 3.35: Acoustic field of the standing wave in frequency domain of the two speakers at 40 kHz, at (a) Nodo to altitude = 7 mm and (b) Antinode to altitude = 10 mm .

The 3D representation using two perpendicular planes allow both in time domain and in frequency domain to visualize the behaviour of the standing wave in 3D as shown in Fig. 3.36. As can be expected, nodes and belly are clearly visible.

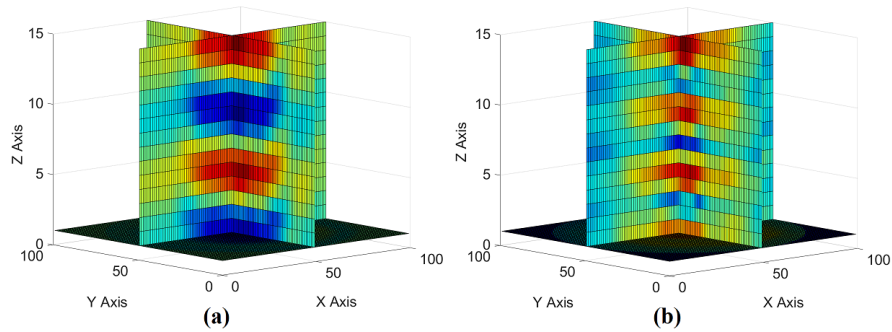


Figure 3.36: Acoustic field of the standing wave in 3D of the two speakers at 40 kHz, (a) time domain (b) frequency domain.

While using the volumetric representation with frequency domain evaluation

of the pressure density is shown in Fig. 3.37

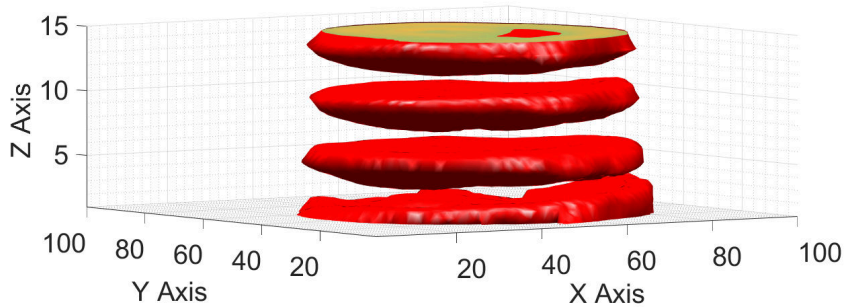


Figure 3.37: Volumetric representation of the acoustic field of the stationary wave in frequency domain of two speakers at 40 kHz facing each others. The observation volume is 100 x 100 x 15 mm.

### 3.5.4 Focused wave with an acoustic concave mirror

In this experiment, the piezoelectric MA40S4S used as the original acoustic source is coupled to a parabolic shaped acoustic reflector. The reflector has a diameter of 4 cm and a depth of 2 cm. It has been specifically manufactured for this application using 3D printing techniques at the workshop of the LAAS-CNRS. The speaker is set face down to the parabolic reflector as shown in Fig. 3.38 and along its symmetric axis thanks to thin metallic attachment which dimensions are expected to have neglectable impact on the acoustic wave propagation. The proposed experimental setup is design to obtain a focus of the acoustic wave after reflexion on the parabolic reflector. The location of the focus is visible at a distance of approximately 50 mm. The scanning volume is set to 100x100x50 mm with a step size of 1 mm, exactly as it was in previous experiments.

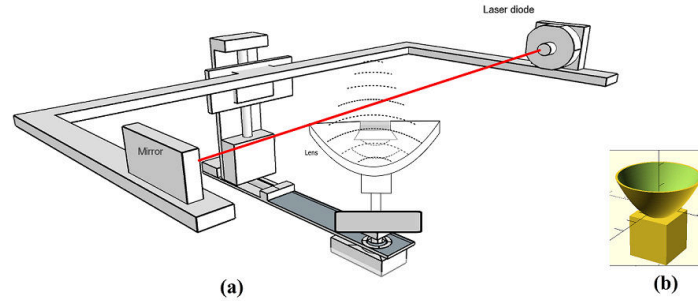


Figure 3.38: Schematic of the ATOFI setup imaging a focused wave produced by reflexion on a concave reflector. (a) Experimental setup description, (b) the parabolic reflector.

The image resulting from this experiment are shown in Fig. 3.39 for the plane located at 1 mm and for the times  $t_0$  and  $t_0 + T/2$ . As we can see in Fig. 3.39, the experimental setup proposed does not produce a similar wave than the speaker alone (see Fig. 3.21(a) and (b) for comparison at same height and  $t_0$ ). The explanation of this difference is not completely clear. It could be a shadowing effect induced by the speaker itself, but one can also imagine the interferences between the reflected wave and the one emitted on the rear side of the speaker and it can very well be a combination of both phenomena.

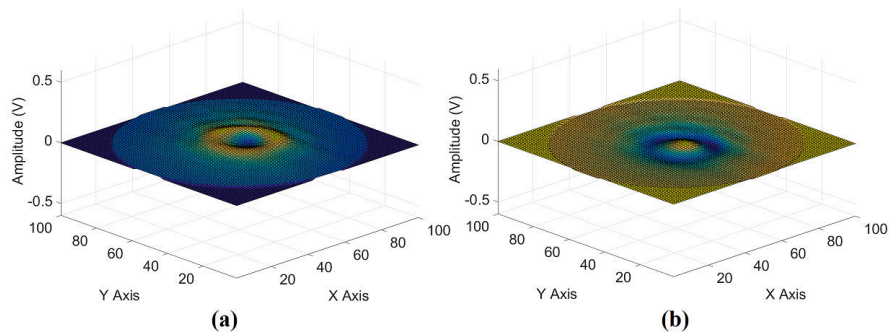


Figure 3.39: Image of the acoustic field slice at the height of 1 mm with the speaker and the parabolic reflector at (a)  $t = t_0$  and (b)  $t = t_0 + T/2$ .

In the following images (Fig. 3.40), the acoustic pressure at the altitude of 50 mm in the time domain is obtained. Again the amplitude of the pressure change in the center of the image is much less than with the speaker alone (see

Fig. 3.21(c) and (d) for comparison).

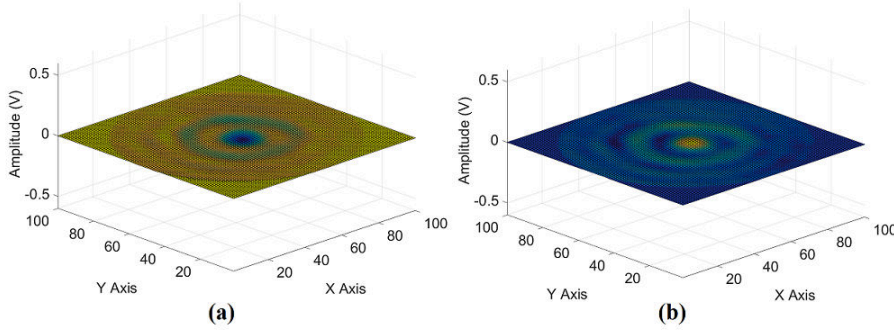


Figure 3.40: Acoustic field in time domain of the 1 speaker and the parabolic lens, at the altitude of 50 mm, at (a)  $t = t_0$  and (b)  $t = t_0 + T/2$ .

It is interesting to observe the distribution of the pressure change in space using the peak amplitude at 40 kHz in the signal spectra. The plot of Fig. 3.41(a) clearly shows an occulting effect at the center of the image at 1 mm while at the altitude of 50 mm, the acoustic pressure has been reconstructed in a coherent way. With comparison to the standalone wave of the speaker alone (Fig. 3.23(b)), one can observe at 50 mm a much better concentration of pressure change at the center of the image that is the result of the focusing effect of the reflector.

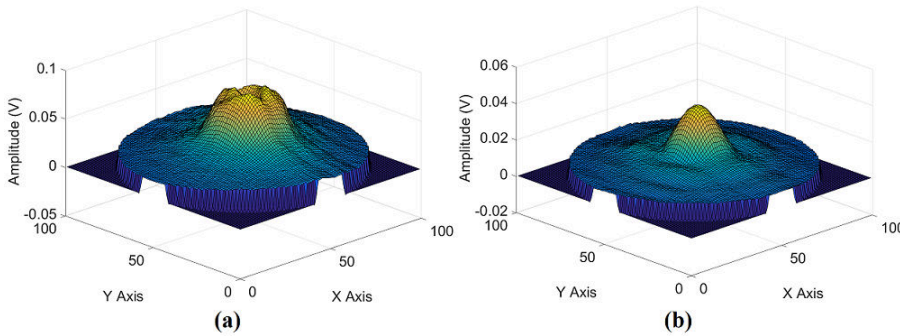


Figure 3.41: Acoustic field in frequency domain of the 1 speaker and acoustic lens, at (a) altitude = 1 mm and (b) altitude = 50 mm.

The focusing effect is very visible in the 3D visualization using orthogonal planes (Fig. 3.42) and with the isosurface based volumetric representation

(Fig. 3.43) even though, because of too short translation axis it has not been possible to observe the defocusing that shall happen at higher altitudes, nor to precisely estimate the focus location.

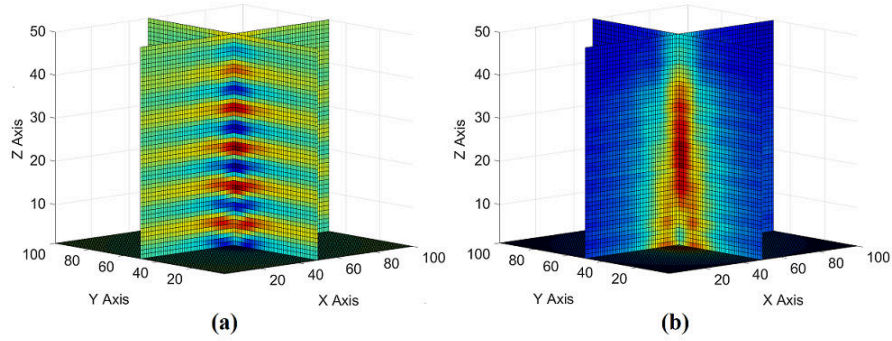


Figure 3.42: 3D representation by two orthogonal planes of the acoustic wave produced by reflexion of a piezo-actuator pressure wave reflected on a concave parabolic shaped reflector (a) time domain (b) frequency domain.

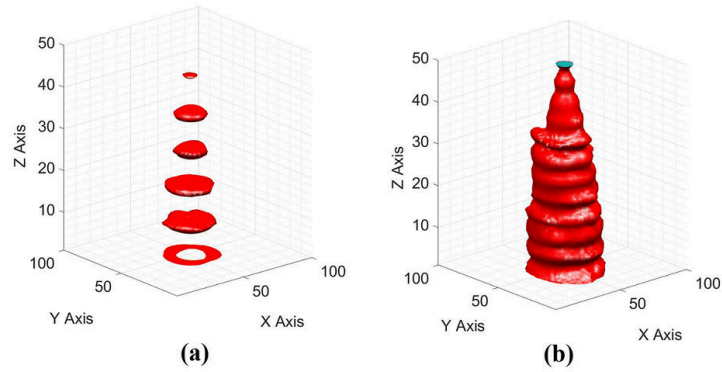


Figure 3.43: Acoustic field in frequency domain of the 1 speaker and parabolic lens, (a) Visual volumetric representation in time domain (b) volumetric representation of the acoustic pressure in a volume of 100 x 100 x 50 mm.

### 3.5.5 Huygens-Fresnel principle in acoustics

For the last experiment in this section, we have built an experimental setup that allows to illustrate the Huygens-Fresnel principle applied to acoustic waves. A large dimension acoustic source is realized by seven smaller diameter sources set in the same plane perpendicular to the acoustic propagation axis. These almost

punctual sources are similar MA40S4S piezo-actuator powered by a 10 Vp-p amplitude with the same phase and placed in a very dense hexagonal distribution as shown in Fig. 3.44. The sum of punctual sources is expected to realize a propagating wave equivalent to the one produced by a unique source with a large vibrating surface.

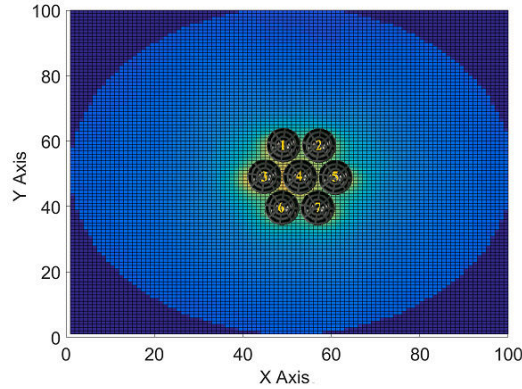


Figure 3.44: Schematic of the seven speakers in form of hexagonal.

The full imaging setup is sketched in Fig. 3.45. It is in all aspect similar to the one used in previous experiments and the imaged volume is delimited by 100x100x29 mm.

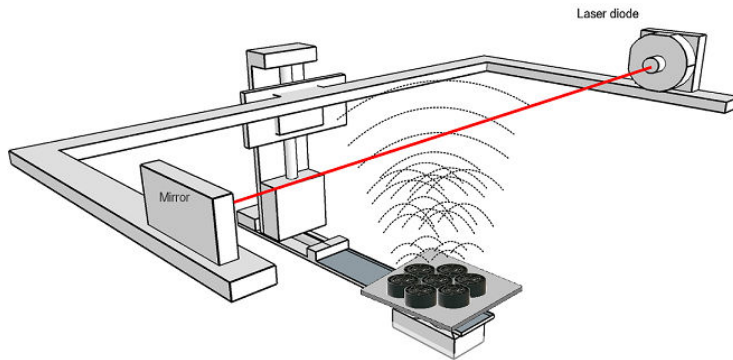


Figure 3.45: The ATOFI setup with the acoustic source of seven speaker in hexagonal form.

In the plane located roughly 1 mm above the speakers, we observe a pressure variation corresponding to the shape of each acoustic pressure. It is plotted in time domain for a given time  $t_0$  and in Fig. 3.46(a). For the same  $t_0$  at a

higher altitude (roughly 29 mm), the variation of pressure distributed in the plane exhibit a unique bump corresponding to the combined pressure changes of the seven speakers and equivalent to a unique source (see Fig. 3.46(b)).

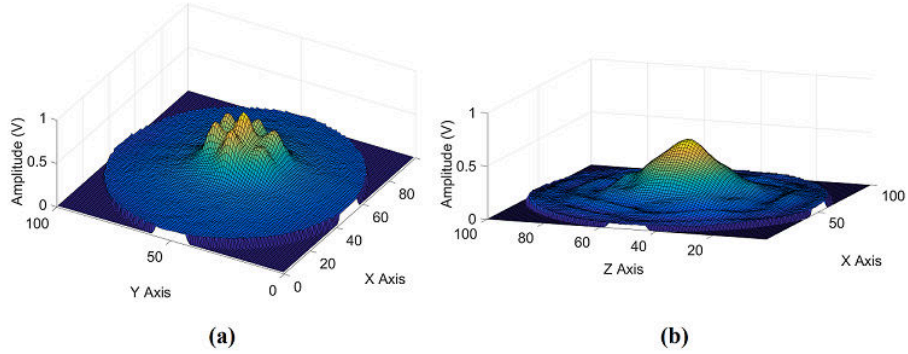


Figure 3.46: Acoustic field in time domain of the seven sources at 40 kHz at different altitude (a) 1 mm and (b) 25 mm

This effect is even more obvious while considering the amplitude of the 40 kHz bin in the FFT for each pixel as plotted in Fig. 3.47(a) and (b) for an altitude of 1 mm and 29 mm respectively. Obviously at the lowest altitude, the acoustic field is in the near field conditions, while at the highest one, a far field condition is achieved and the pressure wave can be considered as emitted by a unique source with large diameter.

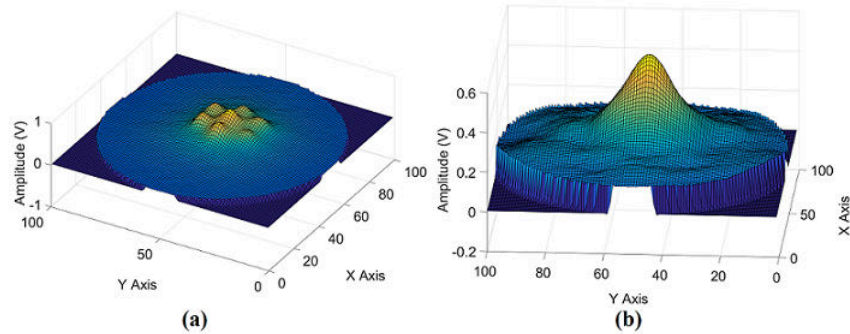


Figure 3.47: Acoustic field in frequency domain of the seven sources at 40 kHz, at (a) altitude = 1 mm and (b) altitude = 29 mm .

In the 3D representation in time domain, the propagation of the acoustic field can be observed as if it was generated by a single sound source Fig. 3.48(a). In

the frequency domain, it is possible to visualize which region of acoustic pressure can be considered as the near field and which is already the far field as shown in Fig. 3.48(b).

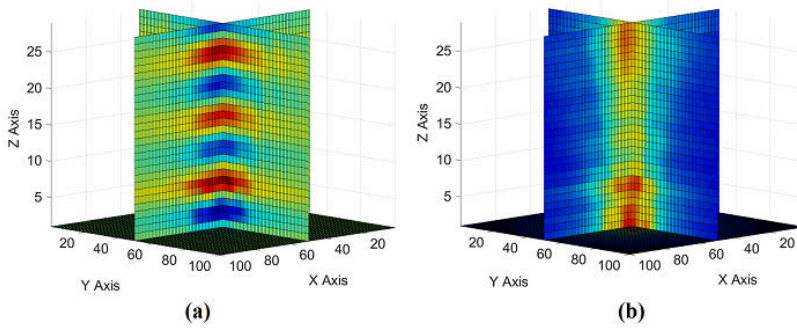


Figure 3.48: Acoustic field of the seven speakers at 40 kHz in 3D, (a) time domain (b) frequency domain.

With the volumetric representation in time domain of Fig. 3.49(a), we can observe the construction of the far field pressure wave passing from the seven distinct sources to a single wave. Using the frequency representation of Fig 3.49(b), one can observe very clearly a waist in the propagated wave at a distance of roughly 10 to 15 mm from the sources plane. This waist defines the limit between far and near fields.

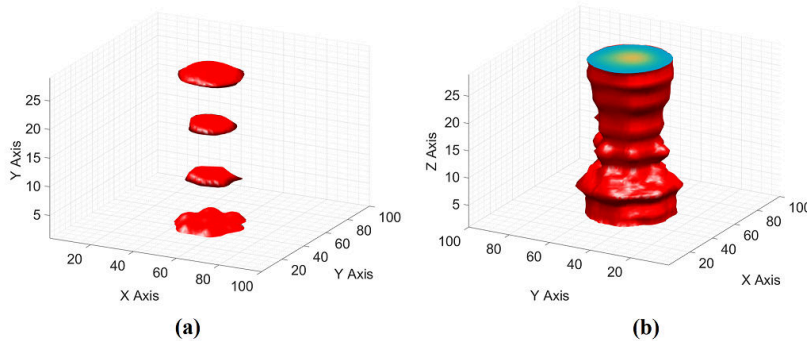


Figure 3.49: Acoustic field of the seven sources at 40 kHz, (a) Visual volumetric representation in time domain (b) Volumetric representation in frequency domain of the acoustic pressure in a volume of 100 x 100 x 25 mm.

Near the acoustic source there are significant fluctuations in the intensity of

the sound due to the constructive and destructive interference of the multiple waves that originate in the face of the source. This region defines the near field of the source. However, at some point the pressure waves combine to form a relatively uniform front. In this region where the beam of the acoustic source is more uniform and extends in a pattern that originates in the center of the transducer, the pressure wave behaviour fits the far field conditions.

The point of transition between the near field and the far field (sometimes called the "natural focus" of an unfocused transducer) can be calculated if the frequency and diameter of the transducer and the speed of sound in the material are known.

The formula for the calculation of the near field is the following

$$z = \frac{D^2 - \lambda^2}{4\lambda}. \quad (3.17)$$

In practice, the diameter of the vibrating surface is much larger than the wavelength of the soundwave and the equation (3.17) can be simplified as,

$$z \approx \frac{D^2}{4\lambda} = N \quad (3.18)$$

where N is the length of near-field extension.

Due to the fact that the arrangement of the seven speakers does not fill all the effective area of the equivalent circle of an ideal source, we have considered two different diameters for the equivalent acoustic source. The first one consider the ideal circle as the one that connect the most excentered points of the six external speakers. These points realize a perfect hexagone, and the second circle is the circumscribed circle in the hexagone. Both circles and the hexagone are plotted in Fig. 3.50 with regard to the speaker arrangement.

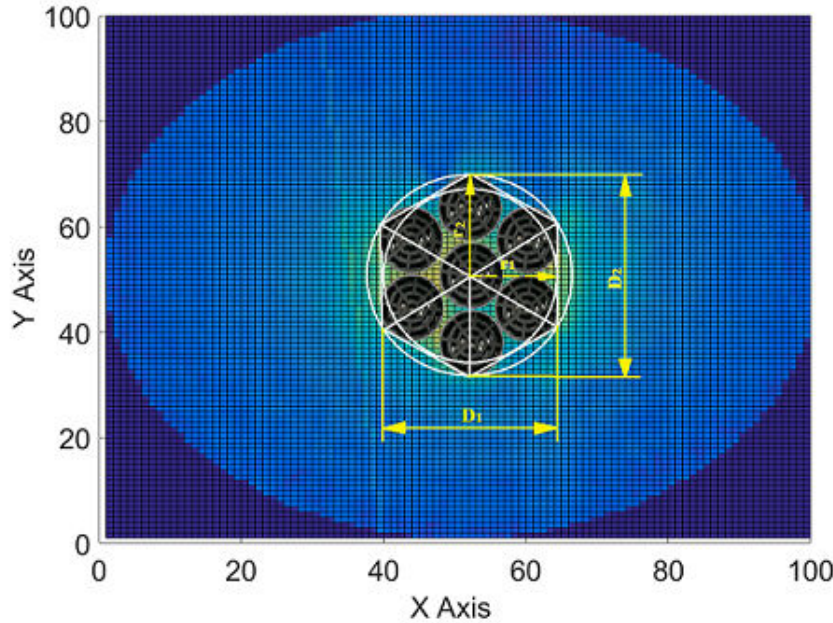


Figure 3.50: Estimation of the diameter of Acoustic Source by seven Speakers.

Considering that the external diameter of the MA40S4S speakers package is 10 mm and applying the Eq. (3.18) the following results are obtained. With:

- $D_1=30$  mm the near field  $N=26.47$  mm,
- $D_2=26$  mm the near field  $N=19.88$  mm.

Taking the Fig. 3.49 (b) as a reference and using the Matlab tool for volumetric representation, a cut was made in the middle of the Y axis, obtaining in this way a two-dimensional image of the acoustic field propagation along the Z axis with respect to the X axis. After having calculated the near field, we proceeded to locate it in the field of propagation, either with an acoustic source with a diameter of 30 mm and 26 mm, as explained in the previous point. What can be observed is that in the calculated region of the near field the acoustic pressure is contracted, possibly due to the chaos caused by the interference of the different acoustic sources (MA40S4S), and then, when forming a single acoustic source, the acoustic pressure extends forming a projection cone in this way

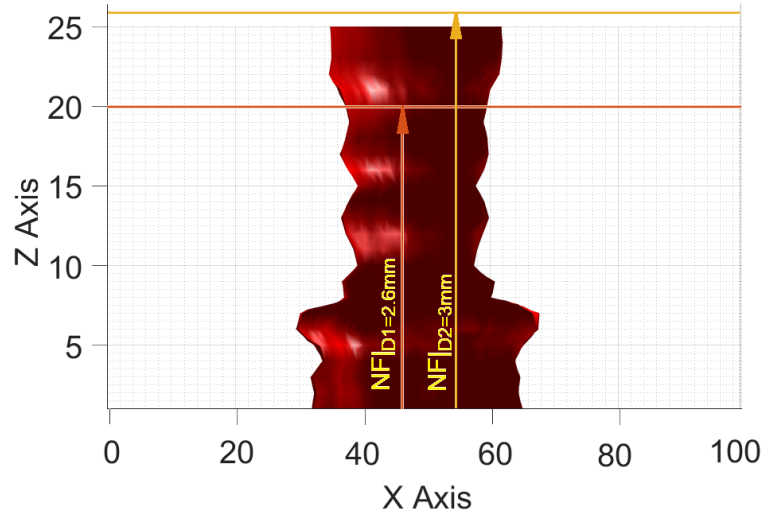


Figure 3.51: Near field in Acoustic propagation by frequency domain of the seven sources at 40 kHz in Y Axis.

### 3.6 Resume

Throughout this chapter it has been demonstrated the feasibility of imaging reconstruction of acoustic waves in three dimensions  $(x,y,z)$  and 4D  $(x,y,z,t)$  by association of the OFI acoustic pressure sensing approach with a technique based on the inverse Radon Transform. This method uses the parallel lines of response of the OFI sensor and projection functions at different measurement angles. Its principle has been explained in detail and the equation have been conditioned to be applied to the opto-acoustic effect through the OFI.

The reconstruction of acoustic fields based on tomography by OFI has been implemented with an algorithm based on the algebraic reconstruction technique (ART) because the data obtained in the acquisition of the acoustic signal are discretized when the response lines (LOR) are applied in a parallel. The resolution of the images obtained in the different experiments visualized in images in three dimensions has been possible thanks to the robust design of the tomographic acquisition system designed in the laboratories of the OSE team of the LAAS-CNRS. These results have made possible to verify some very well know phenomenon encountered with propagating waves (interferences, stationary wave, Huygens-Fresnel,...) but that were extremely difficult to observe in the case of pressure waves through a non-intrusive method. These results and the extreme simplicity of the sensig method reveals promissing applications in the case of more complex acoustic systems as for example the study of acoustic metamaterials [90].

# Conclusion

The development in the field of optics since the invention of the laser has allowed the deployment of optical technology in different research areas. This doctoral thesis first explored the use of optical methods to characterize acoustic fields as a mean to improve the current state of the art in sound measurement. The increasing capacities of computer systems have allowed the development of new measurement techniques to study propagating pressure waves in transparent media such as air and water. Thus, the traditional microphone arrays that are still in use in industrial applications start to be challenged by optical methods. Noteworthy is the spatial and temporal resolution with which optical methods can be used to measure various acoustic phenomena. In comparison, conventional microphones spatial resolution is linked to the dimensions of the microphone membrane. This means that, to improve spatial resolution, the membrane needs to be reduced, resulting in a loss of sensitivity. Schlieren imaging and shadowgraphy have been depicted in the first chapter, but more promising is the development of interferometric methods. In the recent years the Laser Doppler Vibrometry (LDV) has proven to be of major interest for imaging acoustics phenomenon. 2D images in the ultrasonic and audio frequency range first and then, by means of a tomographic imaging approach, in 3D.

Optical feedback interferometry (OFI) is a measurement technique whose implementation for the visualization of acoustic phenomena is quite recent. The measurement principle is based on the disturbance of the laser emission parameters induced by the reinjection in the laser cavity of the back-scattered light through a variation in the round-trip time of the laser light in the external cavity that is established between the laser diode and a distant reflector.

In this thesis, the principle of optical feedback interferometry based on the three mirror model of Fabry-Perot is analyzed by the formal equations of Lang and Kobayashi in which the feedback parameter  $C$  plays an important role in measuring the variations of the refractive index. The measurement principle by optical feedback interferometry with a laser diode employs a detection scheme using the photocurrent of an integrated photodiode, which allowed a non-intrusive measurement of acoustic radiation patterns by means of sensing the refractive index of the medium that it is altered by a mechanical wave produced by an acoustic source. This phenomenon produces a change of the round-trip time of the light when it travels in the section of the outer cavity of the setup of three mirrors, as it was clearly demonstrated in chapter two of this

thesis.

The experimental setup is very simple, and a set of experiments has shown that its operation does not require specific conditions such as an anechoic chamber. Only an anti-vibratory work table was used in all measurement conducted in this thesis. As a first evaluation of the sensing technique, an arrangement of the setup dedicated to the characterization of the radiation pattern of acoustic sources and the experiment in which the tests were established had as a result which was published in paper 1 of this thesis “Characterization of Acoustic Sources by Optical Feedback Interferometry”. In a second step, we have imaged the propagation of acoustic sources in two dimensions .

We have interrogated the way that the integration of refractive index variations along the optical axis of the laser impacts the quality of the 2D image. For that we have designed a simulation of acoustic wave propagation in volume and computed the linear integration of pressure change. With this model, we have been able to confirm that alteration due to the projection along the optical axis induces low alteration of the pressure wave image.

This imaging approach was first used to determine the location of the origin of a spherical wave. With the same experimental setup it is possible to analyze acoustic fields produced by one or more acoustic sources as we explored the case of a stationary wave resulting from a single source facing an acoustic reflector, as well as the case of two identical sources facing each other. This work was published in the peer reviewed journal *Optical Engineering* and in the proceedings of the international conference SPIE Photonics Europe under the titles “Visualization of an acoustic stationary wave by optical feedback interferometry” and “Optical Feedback Interferometry Applied to Visualize an Acoustic Stationary Wave” respectively. In both cases, nodes and belly of the stationary waves were observed without any ambiguity.

These results obtained in the 2D imaging configuration are not presented in this manuscript since in a second time we have managed to images these two stationary waves using the 3D imaging method that is presented in the third chapter of this thesis. The prominent achievement of this thesis was the reconstruction of a three-dimensional image of the propagation of the acoustic field. It has been possible thanks to the robustness that is inherent to the system that we have developed. As compared to the 2D imaging method, the system was modified by the addition of a rotating stage that was remotely controlled and that allows to apply the computed tomography (CT) technique which reconstructs transverse images of the propagation of sounds in a perfectly non-invasive way. The data processing is based on the inverse Radon Transform (RT), which provides cross-sectional images at different levels. The imaging setup achieves a volumetric image that can reach up to  $100 \times 100 \times 100$  voxels with a spatial resolution of 1 millimeter, which gives us a  $10^6$  voxels in total. In order to ensure that the acquisition is performed without vibrations induced by the translation/rotations, rest time of the displacement have been added and a minimum time of 1 hour was required for each slice.

In the chapter three we present several experiments with different resolutions in which different acoustic phenomena can be visualized. We mostly focused our

investigations in the observation of interferences between two or more acoustic sources. Apart for the stationary waves that were discussed in the previous paragraph, we have observed the constructive and destructive interferences produced by two sources located in the same plane and that can be driven in phase or out of phase. Eventually, we also have observed the Huygens Fresnel principle in the acoustic domain by displaying seven sources in the same plane producing a unique wave in the far field that is equivalent to the one that would have produced a large vibrating membrane. In this case, the image of the acoustic propagation in 3D can be used to determine the extension of the near-field propagation domain. It was also possible to determine the focus location of the propagation produced by the association of a spherical source with a concave acoustic reflector. A reflexion was carried out on the best way to represent the 3D images that were computed. We decided that the best solution was to propose two displays: one with two vertical perpendicular sections of the data, and another using the volume rendering tool of Matlab. With the latest, images of the destructive interference produced by the two coplanar acoustic sources in phase opposition are quite impressive in our point of view.

Therefore, the tool developed in this thesis can obtain images of the acoustic field in 2 or 3 dimensions, which allows to have a unique insight of the phenomenon related to the waves either resulting from a unique source or from the interferences between several sources.

It should be noted that the mechanical system designed, control design, data acquisition and processing, necessary to achieve the 3D imaging has been patented. Generally speaking, the work that has been done in this PhD and that is described in the present manuscript has attracted attention in the scientific community as well as in the industrial domain. Currently, a PhD is in progress that applies the acoustic detection using OFI sensor with opto-acoustic effect in the context of a LabCom ANR between the OASIS team and the company ACOEM that is devoted to non-destructive testing of industrial machinery. In the mean time, a collaboration has been established with the Institut Fresnel in Marseille, which objective is to deploy acoustic imaging in acoustic metamaterials. In the context of a joint laboratory called LICUR, the OASIS team of the LAAS-CNRS and the CEA Gramat are starting to investigate the potential of OFI sensors for detection of pressure shock waves generated by explosives. Eventually, the contribution of OFI sensing in acoustic could be of interest in the domain of biology where researcher are investigating the auditory systems of animals and plants. This interest is at the origin of the present PhD after the contact we initially had with researchers in bio-mechanics of the University of Bristol that has trigger our research in the acoustic domain.



# Recommendations

The prototype was developed for 40 KHz waves so if you want to work with audible frequencies you need to modify its design since at low frequencies the wavelength of the sound increases, which should make new analyzes of the environment and the laboratory because it will work with sound waves that will have spatial lengths in the order of decimetres, therefore these waves being large could cause reflection in a laboratory of small dimensions creating interference in the wave to be analyzed. The acquisition time for the image acquisition in 2 and 3 D, can be reduced if more than one laser diode is used, however the calibration of these will be a research topic since they must have the same characteristics for the same environment. to be analyzed, subject that is complex due to the position of the third mirror in the Fabry-Pérot model.



# Future work

The results obtained with the OFI system based on the structure of three mirrors with a laser diode show that there is a potential development of projects to evaluate metamaterials, being able to analyze even their unique characteristics such as negative refractive indices, as well as the behavior of an acoustics when it crosses these elements. Another future work will be through this system to analyze the internal cracks caused by manufacturing defects in high voltage insulators, which are imperceptible to the naked eye and can only be detected when they are in operation, because when an insulator has a factory defect emits an approximate wave at 40KHz. Another work could be focused on the visualization of the acoustic wave that produces a high-cost musical instrument with a low-cost one.



# Bibliography

- [1] E. S. Holmes and S. Chang, "Visualization of 3-dimensional beam patterns using the sgi workstation," in Proceedings of OCEANS '93, pp. III353–III358 vol.3, Oct 1993.
- [2] L. Brillouin, "Diffusion of light and x-rays by a transparent homogeneous body ," Annalen der Physik, vol. 17, pp. 88–95, 1922.
- [3] P. Debye and F. W. Sears, "On the Scattering of Light by Supersonic Waves," Proceedings of the National Academy of Sciences of the United States of America, vol. 18, pp. 409–414, 1932.
- [4] R. Lucas and P. Biquard, "Optical properties of solid and liquid medias subjected to high-frequency elastic vibrations," Journal de Physique et le Radium, vol. 3, pp. 464–477, 1932.
- [5] C. V. Raman and N. S. N. Nath, "The diffraction of light by high frequency sound waves : Part I," Proceedings of the Indian Academy of Sciences - Section A, vol. 2, pp. 406–412, 1935.
- [6] C. V. Raman and N. S. N. Nath, "The diffraction of light by high frequency sound waves : Part II," Proceedings of the Indian Academy of Sciences - Section A, vol. 2, pp. 413–420, 1935.
- [7] C. V. Raman and N. S. N. Nath, "The diffraction of light by high frequency sound waves : Part III," Proceedings of the Indian Academy of Sciences - Section A, vol. 3, pp. 75–84, 1936.
- [8] C. V. Raman and N. S. N. Nath, "The diffraction of light by high frequency sound waves : Part IV," Proceedings of the Indian Academy of Sciences - Section A, vol. 3, pp. 119–125, 1936.
- [9] C. V. Raman and N. S. N. Nath, "The diffraction of light by high frequency sound waves : Part V," Proceedings of the Indian Academy of Sciences - Section A, vol. 3, pp. 459–465, 1936.
- [10] J. H. Barrell, J. E. Sears and W. L. Bragg, "The refraction and dispersion of air and dispersion of air for the visible spectrum," 238 Philosophical Transactions of the Royal Society of London. Series A, Mathematical and Physical Sciences, 1939.

- [11] B. Edlén, “The Dispersion of Standard Air\*,” J. Opt. Soc. Am., vol. 43, pp. 339–344, May 1953.
- [12] J. C. Owens, “Optical Refractive Index of Air: Dependence on Pressure, Temperature and Composition,” Appl. Opt., vol. 6, pp. 51–59, Jan 1967.
- [13] E. R. Peck and K. Reeder, “Dispersion of Air\*,” J. Opt. Soc. Am., vol. 62, pp. 958–962, Aug 1972.
- [14] K. P. Birch and M. J. Downs, “An Updated Edlén Equation for the Refractive Index of Air,” Metrología, vol. 30, pp. 155–162, 1993.
- [15] P. E. Ciddor, “Refractive index of air: new equations for the visible and near infrared,” Appl. Opt., vol. 35, pp. 1566–1573, Mar 1996.
- [16] P. E. Ciddor and R. J. Hill, “Refractive index of air. 2. Group index,” Appl. Opt., vol. 38, pp. 1663–1667, Mar 1999.
- [17] P. E. Ciddor, “Refractive index of air: 3. The roles of CO<sub>2</sub>, H<sub>2</sub>O, and refractivity virials,” Appl. Opt., vol. 41, pp. 2292–2298, Apr 2002.
- [18] J. Muelaner, “ciddor equation for refractive index of air,” 2015.
- [19] C. H. Hansen, Occupational exposure to noise: evaluation, prevention and control. WHO, 06 2001.
- [20] D. Bies, C. Hansen, and C. Howard, Engineering Noise Control, Fifth Edition. CRC Press, 11 2017.
- [21] J. L. Flanagan, J. D. Johnston, R. Zahn, and G. W. Elko, “Computer-steered microphone arrays for sound transduction in large rooms,” J. Acoust. Soc., vol. 78, pp. 1508–1518, 01 1985.
- [22] J. L. Flanagan, R. Mammone, and G. W. Elko, “Autodirective Microphone Systems for Natural Communication with Speech Recognizers,” in Proceedings of the Workshop on Speech and Natural Language, HLT '91, (Stroudsburg, PA, USA), pp. 170–175, Association for Computational Linguistics, 1991.
- [23] H. F. Silverman, W. R. Patterson, and J. L. Flanagan, “The huge microphone array,” IEEE Concurrency, vol. 6, pp. 36–46, Oct 1998.
- [24] E. Weinstein, K. Steele, A. Agarwal, and J. Glass, “A 1200 - Node Modular Microphone Array and Beamformer for Intelligent Computing Spaces,” tech. rep., Massachusetts Institute of Technology Computer Science and Artificial Intelligence Laboratory, 12 2004.
- [25] R. Groschup and C. U. Grosse, “MEMS Microphone Array Sensor for Air-Coupled Impact-Echo,” Sensors, vol. 15, no. 7, pp. 14932–14945, 2015.

- [26] J. Tiete, F. Domínguez, B. d. Silva, L. Segers, K. Steenhaut, and A. Touhafi, “Sound Compass: A Distributed MEMS Microphone Array-Based Sensor for Sound Source Localization,” Sensors, vol. 14, no. 2, pp. 1918–1949, 2014.
- [27] I. Hafizovic, C.-I. C. Nilsen, M. Kjølervbakken, and V. Jahr, “Design and implementation of a MEMS microphone array system for real-time speech acquisition,” Applied Acoustics, vol. 73, no. 2, pp. 132–143, 2012.
- [28] R. White, J. Krause, R. De Jong, G. Holup, J. Gallman, and M. Moeller, “MEMS Microphone Array on a Chip for Turbulent Boundary Layer Measurements,” 50th AIAA Aerospace Sciences Meeting including the New Horizons Forum and Aerospace Exposition, 01 2012.
- [29] C. Vanwynsberghe, R. Marchiano, F. Ollivier, P. Challande, H. Moingeon, and J. Marchal, “Design and implementation of a multi-octave-band audio camera for realtime diagnosis,” Applied Acoustics, vol. 89, pp. 281 – 287, 2015.
- [30] J. J. V. Lara del Val, Alberto Izquierdo and L. Suárez, “Using a Planar Array of MEMS Microphones to Obtain Acoustic Images of a Fan Matrix,” Journal of Sensors, 2017.
- [31] W. L. Bragg, “The diffraction of short electromagnetic waves by a crystal,” Scientia, vol. 23, no. 45, p. 153, 1929.
- [32] N. S. N. Nath, “The diffraction of light by high frequency sound waves: generalised theory,” Proceedings of the Indian Academy of Sciences - Section A, vol. 4, pp. 222–242, Aug 1936.
- [33] R. Adler, “Interaction between light and sound,” IEEE Spectrum, vol. 4, pp. 42–54, May 1967.
- [34] E. I. Gordon, “A review of acoustooptical deflection and modulation devices,” Proceedings of the IEEE, vol. 54, pp. 1391–1401, Oct 1966.
- [35] C. F. Quate, C. D. W. Wilkinson, and D. K. Winslow, “Interaction of light and microwave sound,” Proceedings of the IEEE, vol. 53, pp. 1604–1623, Oct 1965.
- [36] L. Brillouin, “Diffusion de la lumidre et des rayons x par un corps transparent homogdne,” Ann. Phys, 1922.
- [37] R. Lucas and P. Biquard, “Propriétéb optiques des milieux solides et liquides soumis aux vibration glastiques ultra sonores,” J. Phys.Rad., vol. 3, pp. 464–477, 1932.
- [38] P. Debye and F. W. Sears, “On the scattering of light by supersonic waves,” Proc. Nut. Acad. Sci. (US.), vol. 18, pp. 409–414, 1932.

- [39] H. Schardin, "Schlieren methods and their applications.," Ergeb. Exakten Naturewiss, vol. 20, no. 303, 1942.
- [40] G. S. Settles, Schlieren and Shadowgraph Techniques: Visualizing Phenomena in Transparent Media, vol. 21. springer, 12 2002.
- [41] S. Frank and J. Schell, "Sound field simulation and visualization based on laser doppler vibrometer measurement," Proc Forum Acust, pp. 91–97, 1988.
- [42] G. Meier, "Computerized background-oriented schlieren," Experiments in Fluids, vol. 33, pp. 181–187, Jul 2002.
- [43] H. Richard and M. Raffel, "Principle and applications of the background oriented schlieren (BOS) method," Measurement Science and Technology, vol. 12, no. 9, p. 1576, 2001.
- [44] H. G. Taylor and J. M. Waldram, "Improvements in the Schlieren method," Journal of Scientific Instruments, vol. 10, no. 12, p. 378, 1933.
- [45] A. Mazumdar, "Principles and Techniques of Schlieren Imaging Systems," tech. rep., Columbia University Computer Science Technical Reports, 2013.
- [46] G. Wetzstein, R. Raskar, and W. Heidrich, "Hand-Held Schlieren Photography with Light Field Probes," in IEEE International Conference on Computational Photography (ICCP), 2011.
- [47] B. Atcheson, W. Heidrich, and I. Ihrke, "An evaluation of optical flow algorithms for background oriented schlieren imaging," Experiments in Fluids, vol. 46, pp. 467–476, Mar 2009.
- [48] M. Hargather and G. Settles, "Natural-background-oriented schlieren imaging," Experiments in Fluids, vol. 48, pp. 59–68, 01 2010.
- [49] R. J. Goldstein, Fluid mechanics measurements. New York: Taylor and Francis, 1996.
- [50] K. M. Pradipta Kumar Panigrahi, schlieren and shadowgraph methods in heat and mass transfer. Springer, 2012.
- [51] Settles, "Schlieren and shadowgraph techniques: visualizing phenomena in transparent media: g.s. settles (springer-verlag, berlin, germany, 2001)," European Journal of Mechanics - B/Fluids, vol. 21, p. 493, 12 2001.
- [52] D. Kikuchi and M. Sun, "Numerical analysis of optical systems for compressible flow visualization," in Computational Fluid Dynamics 2008 (H. Choi, H. G. Choi, and J. Y. Yoo, eds.), (Berlin, Heidelberg), pp. 801–804, Springer Berlin Heidelberg, 2009.

- [53] G. S. Settles and M. J. Hargather, “A review of recent developments in schlieren and shadowgraph techniques,” Measurement Science and Technology, vol. 28, p. 042001, Apr. 2017.
- [54] D. R. Jonassen, G. S. Settles, and M. D. Tronosky, “Schlieren PIV for turbulent flows,” Optics and Lasers in Engineering, vol. 44, no. 3, pp. 190 – 207, 2006. Optical Methods in Heat Transfer and Fluid Flow.
- [55] C. T. Johansen and G. Ciccarelli, “Visualization of the unburned gas flow field ahead of an accelerating flame in an obstructed square channel,” Combustion and Flame, vol. 156, no. 2, pp. 405 – 416, 2009.
- [56] J. Bucaro and H. D. Dardy, “Visualization of ultrasonic waves in air,” The Journal of the Acoustical Society of America, vol. 62, pp. 1506–1507, 12 1977.
- [57] D. Bershader, S. G. Prakash, and G. Huhn, “Improved flow visualization by use of resonant refractivity,” in 14th Aerospace Sciences Meeting, 01 1976.
- [58] M. J. Hargather, G. S. Settles, and M. J. Madalis, “Schlieren imaging of loud sounds and weak shock waves in air near the limit of visibility,” Shock Waves, vol. 20, pp. 9–17, Feb 2010.
- [59] D. J. Heeger, “Optical flow using spatiotemporal filters,” International Journal of Computer Vision, vol. 1, pp. 279–302, Jan 1988.
- [60] N. Chitanont, K. Yaginuma, K. Yatabe, and Y. Oikawa, “Visualization of sound field by means of Schlieren method with spatio-temporal filtering,” in 2015 IEEE International Conference on Acoustics, Speech and Signal Processing (ICASSP), pp. 509–513, April 2015.
- [61] N. Kudo, H. Ouchi, K. Yamamoto, and H. Sekimizu, “A simple Schlieren system for visualizing a sound field of pulsed ultrasound,” Journal of Physics: Conference Series, vol. 1, no. 1, p. 146, 2004.
- [62] D. Havelock, S. Kuwano, and M. Vorländer, Handbook of Signal Processing in Acoustics. Springer-Verlag New York, 1st ed., 2008.
- [63] M. Schroeder, T. D. Rossing, F. Dunn, W. M. Hartmann, D. M. Campbell, and N. H. Fletcher, Springer Handbook of Acoustics. Springer Publishing Company, Incorporated, 1st ed., 2007.
- [64] K. Tatar, E. Olsson, and F. Forsberg, “Tomographic Reconstruction of 3D Ultrasound Fields Measured Using Laser Vibrometry,” in Experimental Analysis of Nano and Engineering Materials and Structures (E. E. Gdoutos, ed.), (Dordrecht), pp. 337–338, Springer Netherlands, 2007.

- [65] F. F. Erik Olsson, “Three-dimensional selective imaging of sound sources,” Optical Engineering, vol. 48, no. 3, pp. 1 – 8 – 8, 2009.
- [66] S. Frank and J. Schell, “Sound field simulation and visualization based on laser doppler vibrometer measurement,” Proc Forum Acust, pp. 91–5, 2005.
- [67] Y. Oikawa, M. Goto, Y. Ikeda, T. Takizawa, and Y. Yamasaki, “Sound field measurements based on reconstruction from laser projections,” in Proceedings. (ICASSP '05). IEEE International Conference on Acoustics, Speech, and Signal Processing, 2005., vol. 4, pp. iv/661–iv/664 Vol. 4, March 2005.
- [68] Y. Oikawa, T. Hasegawa, Y. Ouchi, Y. Yamasaki, and Y. Ikeda, “Visualization of sound field and sound source vibration using laser measurement method,” in 20th International Congress on Acoustics 2010, ICA 2010 - Incorporating Proceedings of the 2010 Annual Conference of the Australian Acoustical Society, vol. 2, pp. 992–996, 2010.
- [69] R. Malkin, T. Todd, and D. Robert, “A simple method for quantitative imaging of 2D acoustic fields using refracto-vibrometry,” Journal of Sound and Vibration, vol. 333, no. 19, pp. 4473 – 4482, 2014.
- [70] K. Nakamura, M. Hirayama, and S. Ueha, “Measurements of air-borne ultrasound by detecting the modulation in optical refractive index of air,” in 2002 IEEE Ultrasonics Symposium, 2002. Proceedings., vol. 1, pp. 609–612 vol.1, Oct 2002.
- [71] K. Ishikawa, Y. Oikawa, and Y. Yamasaki, “Non-intrusive sound pressure measurement using light scattering,” Acoustical Science and Technology, vol. 36, no. 5, pp. 408–418, 2015.
- [72] Y. Oikawa, K. Yatabe, K. Ishikawa, and Y. Ikeda, “Optical sound field measurement and imaging using laser and high-speed camera,” in Proceedings of the INTER-NOISE 2016 - 45th International Congress and Exposition on Noise Control Engineering: Towards a Quieter Future, pp. 258–266, German Acoustical Society (DEGA), 8 2016.
- [73] A. Torras Rosell, S. Barrera Figueroa, and F. Jacobsen, “Sound field reconstruction using acousto-optic tomography,” Acoustical Society of America. Journal, vol. 131, no. 5, pp. 3786–3793, 2012.
- [74] K. Petermann, Laser Diode Modulation and Noise. Springer Science & Business Media, Dec. 2012.
- [75] R. Lang and K. Kobayashi, “External optical feedback effects on semiconductor injection laser properties,” IEEE Journal of Quantum Electronics, vol. 16, pp. 347–355, Mar 1980.
- [76] T. Taimre and A. D. Rakić, “characteristic parameter C in semiconductor lasers,” Appl. Opt., vol. 53, pp. 1001–1006, Feb 2014.

- [77] S. Donati, G. Giuliani, and S. Merlo, “Laser diode feedback interferometer for measurement of displacements without ambiguity,” IEEE Journal of Quantum Electronics, vol. 31, pp. 113–119, Jan 1995.
- [78] R. Kliese, T. Taimre, A. A. A. Bakar, Y. L. Lim, K. Bertling, M. Nikolić, J. Perchoux, T. Bosch, and A. D. Rakić, “Solving self-mixing equations for arbitrary feedback levels: a concise algorithm,” Appl. Opt., vol. 53, pp. 3723–3736, Jun 2014.
- [79] Y. Yu, J. Xi, J. F. Chicharo, and T. M. Bosch, “Optical Feedback Self-Mixing Interferometry With a Large Feedback Factor  $C$  : Behavior Studies,” IEEE Journal of Quantum Electronics, vol. 45, pp. 840–848, July 2009.
- [80] K. Bertling, J. Perchoux, T. Taimre, R. Malkin, D. Robert, A. D. Rakić, and T. Bosch, “Imaging of acoustic fields using optical feedback interferometry,” Opt. Express, vol. 22, pp. 30346–30356, Dec 2014.
- [81] F. E. Jones, “Simplified equation for calculating the refractivity of air,” Appl. Opt., vol. 19, pp. 4129–4130, Dec 1980.
- [82] F. Depasse, M. A. Paesler, D. Courjon, and J. M. Vigoureux, “Huygens–Fresnel principle in the near field,” Opt. Lett., vol. 20, pp. 234–236, Feb 1995.
- [83] P. B. Johns, “A new mathematical model to the physics of propagation,” Radio and Electronic Engineer, vol. 44, pp. 657–666, December 1974.
- [84] S. Nonogaki, “A Rigorous Solution of Two-Dimensional Diffraction Based on the Huygens-Fresnel Principle,” Japanese Journal of Applied Physics, vol. 28, no. 5R, p. 786, 1989.
- [85] B. Shoelson, “Fitting a Circle, easily.” <https://blogs.mathworks.com/pick/2008/03/14/fitting-a-circle-easily/#>, 2008 (accessed March 14, 2008).
- [86] K. Yatabe, K. Ishikawa, and Y. Oikawa, “Acousto-optic back-projection: Physical-model-based sound field reconstruction from optical projections,” Journal of Sound and Vibration, vol. 394, pp. 171 – 184, 2017.
- [87] A. C. Kak and M. Slaney, Principles of computerized tomographic imaging. Philadelphia: Society for Industrial and Applied Mathematics, 2001.
- [88] S. R. Deans, The Radon Transform and Some of Its Applications. Dover Books on Mathematics Series, Dover Publications, 2007.
- [89] F. Kharfi, “Mathematics and physics of computed tomography (ct): Demonstrations and practical examples,” in Imaging and Radioanalytical Techniques in Interdisciplinary Research (F. Kharfi, ed.), ch. 4, Rijeka: IntechOpen, 2013.

- [90] M. Dubois, J. Perchoux, A. L. Vanel, C. Tronche, Y. Achaoui, G. Dupont, K. Bertling, A. D. Rakić, T. Antonakakis, S. Enoch, R. Abdeddaim, R. V. Craster, and S. Guenneau, “Acoustic flat lensing using an indefinite medium,” Phys. Rev. B, vol. 99, p. 100301, Mar 2019.
- [91] B. G. Stuttgart, “The Mathematics of Computerized Tomography. ,” ZAMM - Journal of Applied Mathematics and Mechanics, vol. 67, no. 11, pp. 580–580, 1986.

## Appendix A

# Radon Transform Properties

In this section, we describe some of the important properties of the RT. Let's assume any function  $f$  so that  $f(x, y) \xleftrightarrow{Radon} p(r, \theta)$

- Linearity: If  $g \xleftrightarrow{Radon} q(r, \theta)$ , then

$$\alpha f + \beta g \xleftrightarrow{Radon} \alpha p + \beta q \quad (\text{A.1})$$

- Shift/Translation:

$$f(x - x_0, z - z_0) \xleftrightarrow{Radon} p(\theta, r - x_0 \cos \theta - z_0 \sin \theta) \quad (\text{A.2})$$

- Rotation:

$$f(x \cos \theta' + z \sin \theta', -x \sin \theta' + z \cos \theta') \xleftrightarrow{Radon} p(\theta - \theta', r) \quad (\text{A.3})$$

- Simetry/Periodicity:

$$p(r, \theta) = p(\theta \pm \pi, -r) = p(\theta \pm k\pi, (-1)^k r), \forall k \in \mathbb{Z} \quad (\text{A.4})$$

Affine Scaling special cases of affine scale property.

$$f(\alpha x, \beta z) \xleftrightarrow{Radon} \frac{p_{\angle\pi}(\beta \cos \theta, \alpha \sin \theta) \left( \frac{r|\alpha|\beta}{\sqrt{(\beta \cos \theta)^2 + (\alpha \sin \theta)^2}} \right)}{\sqrt{(\beta \cos \theta)^2 + (\alpha \sin \theta)^2}} \theta \quad (\text{A.5})$$

For  $\alpha, \beta \neq 0$ , where  $r_{\pm}(\alpha a, \beta b) = \alpha r \pm (a, b)$  and  $\angle_{\pi}(\alpha a, \beta b) = \angle_{\pi}(a, b)$

- Magnification/Minification

$$f(x, -z) \xleftrightarrow{Radon} p(\pi - \theta, -r) \quad (\text{A.6})$$

- Flips

$$f(-x, z) \xleftrightarrow{Radon} p(\pi - \theta, r) \quad (\text{A.7})$$

- The Projection Integral Theorem: with  $h$  a scalar function:  $h : \mathbb{R} \rightarrow \mathbb{R}$  :

$$\int p(r, \theta) h(r) dr = \iint f(x, z) h(x \cos \theta + z \sin \theta) dx dz \quad (\text{A.8})$$

Volume Conservation: The volume conservation property is one of many consistency conditions of the RT [91].

$$\iint_{-\infty}^{\infty} f(x, z) dx dz = \int_{-\infty}^{\infty} p(r, \theta) dr d\theta \quad (\text{A.9})$$

## Appendix B

# Publishers



Proceedings

# Characterization of Acoustic Sources by Optical Feedback Interferometry <sup>†</sup>

Fernando Urgiles <sup>1,2</sup>, Julien Perchoux <sup>1,\*</sup> and Thierry Bosch <sup>1</sup>

<sup>1</sup> Laboratory for Analysis and Architecture of Systems (LAAS-CNRS), Université de Toulouse, CNRS, INP, Toulouse, France; patriciofernando.urgilesortiz@enseeiht.fr (F.U.); thierry.bosch@laas.fr (T.B.)

<sup>2</sup> Universidad Politécnica Salesiana, Cuenca, Ecuador

\* Correspondence: julien.perchoux@laas.fr; Tel.: +33-5-3432-2560

<sup>†</sup> Presented at the EuroSensors 2017 Conference, Paris, France, 3–6 September 2017.

Published: 23 August 2017

**Abstract:** Sound can be described as the propagation of pressure variations in compressible media that involves compression and expansion and induces a change in the density of the medium. This change in acoustic pressure as it induces a change of the refractive index can be measured by optical methods, the most recent being the optical feedback interferometry. With this technique, a laser diode is beaming on a reflective surface thus creating a cavity where the acoustic wave propagates. This paper presents a novel experimental technique to measure radiation pattern of acoustic sources based on optical feedback interferometry in a laser diode.

**Keywords:** optical feedback interferometry; acoustic; ultrasound; radiation pattern

## 1. Introduction

In the present research, we have elaborated a novel system to measure the sound pressure level emitted by an acoustic source. The measurement principle stands on the impact of the acoustic pressure on the transparent medium refractive index [1–5]. The experimental arrangement is as follows: the laser and the reflective surface are set in a fixed position while the acoustic wave crosses the laser beam and the change in refractive index induces changes of the optical path of the cavity (Figure 1). The variation of the laser emitted power  $P_F$  is given by [2]:

$$P_F = P_0[1 + m \cos(\omega_F \tau)] \quad (1)$$

where  $P_0$  is the laser emitted power without optical feedback,  $m$  is the modulation index that depends mostly on the reflectivity of the cavity and  $\omega_F$  is the angular frequency of the laser electric field. Eventually,  $\tau$  is the round-trip time of flight in the external cavity. In the present situation  $\tau = \tau_0 + \delta\tau$ , where  $\tau_0$  is the round-trip time in absence of pressure variations that is equal to  $2n_0L/c$  with  $L$  the length of the laser-target cavity,  $c$  is the velocity of light in vacuum and  $n_0$  is the refractive index of the external cavity medium. The variation induced by the medium compression  $\delta\tau$  can be defined by

$$\delta\tau = \int_0^L \frac{2\delta n(z)}{c} dz \quad (2)$$

where  $\delta n(z)$  is the change of the refractive index along the Z axis where the laser propagates.

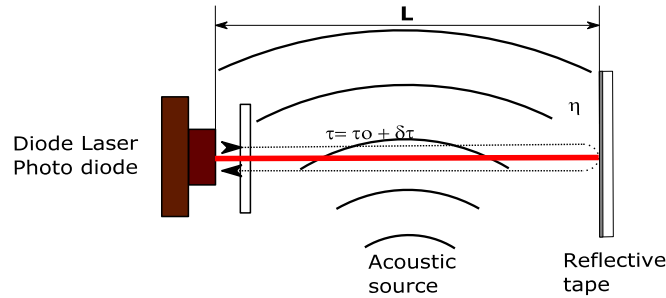


**Figure 1.** Principle of acoustic pressure sensing using optical feedback interferometry. The distance between the laser and the mirror is fixed; the laser diode and the monitoring photodiode are in the same package.

## 2. Experimental Setup

The acoustic source is an ultrasonic piezoelectric transmitter (MA40B8S) driven by a sinusoidal voltage at 40 kHz. It is mounted on a rotating stage controlled by a step motor. The optical feedback interferometer consists in a laser diode ML725B11F emitting at 1310 nm and a microspheres reflective tape glued on the target. The distance between the laser and the target is 200 mm and the sound wave propagates in a perpendicular plane to the laser propagation axis (Figure 2a). The distance between the laser beam and the acoustic source is set to 100mm.

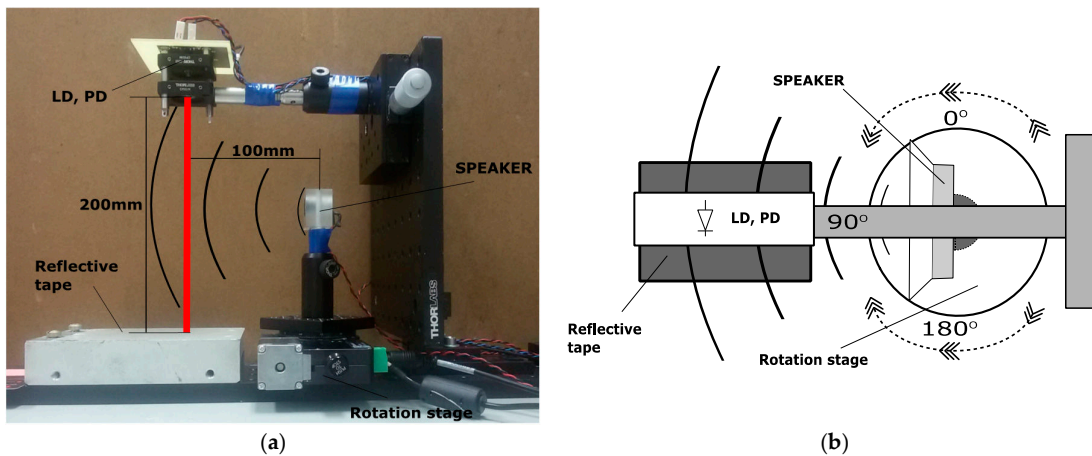


**Figure 2.** (a) Side view of the setup that includes an ultrasonic piezoelectric transmitter (MA40B8S) driven by a sinusoidal voltage at 40kHz, 10 V and the optical feedback interferometer consisting in a laser diode ML725B11F emitting at 1310 nm associated to a microspheres reflective tape; (b) Top view of the setup, showing the rotating stage position from 0° to +180° with clockwise and counter clockwise movement.

Laser power variations are acquired through the monitoring photodiode included in the laser package, then using an acquisition card (NI-USB-6251) with a 1MHz sampling frequency. A Labview program controls the acquisition as well as the rotating stage position from 0° to +180° with a step of 1 degree. At each angular position 4096 samples of the amplified photodiode current are acquired then Fast Fourier Transform is performed (Figure 3).

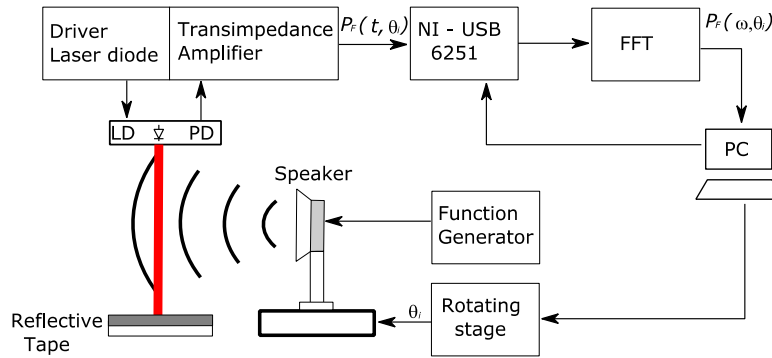


Figure 3. System of measure the sound pressure level of the sound emitted by an acoustic source.

### 3. Results

Figure 4a presents the OFI sensor signal for 0°, 90° and 180° and it can be seen that as expected the acoustic pressure is much stronger in the normal direction of propagation (90°) than on the lateral directions. Figure 4b is the FFT of the sensor signal when the speaker emits towards the laser and a peak at the speaker excitation frequency can clearly be observed that rises by 30 dB from the noise floor. The amplitude of the 40 kHz peak in the FFT is stored and a polar plot is computed that represents the radiation pattern of the source. Figure 4c shows the normalized radiation pattern that was measured for the MA40B8S ultrasonic source.

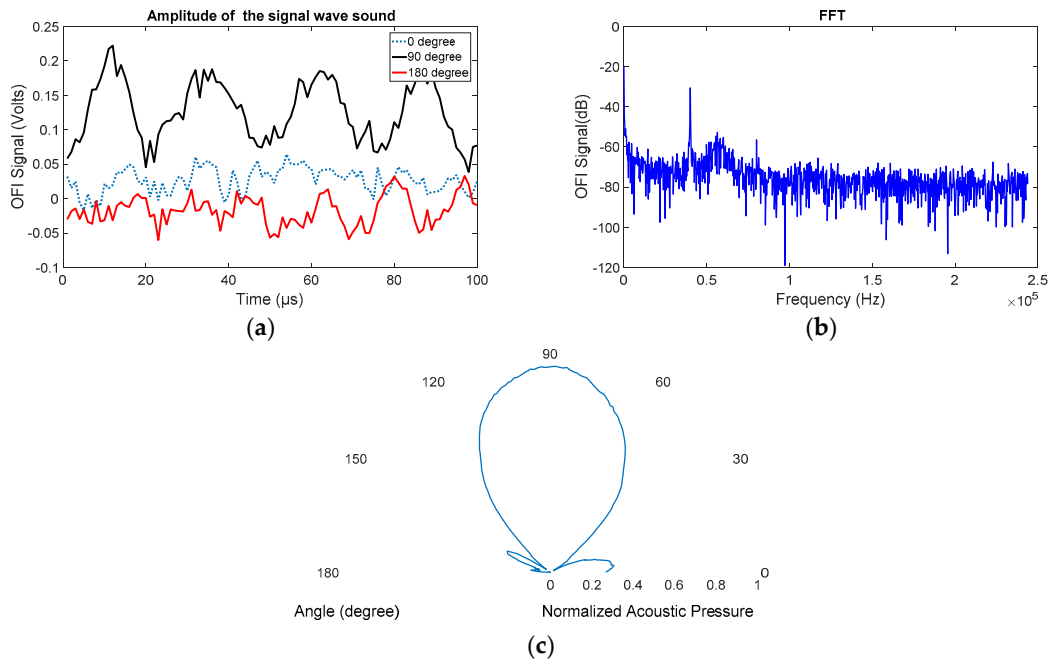


Figure 4. Measurement results. (a) Time domain signals at 0° (blue dashedline), 90° (black line) and 180° (red line); (b) Frequency domain signal when the sound propagation is done towards the laser beam (corresponding to 90°); (c) Normalized acoustic pressure radiation pattern of the MA40B8S ultrasonic piezoelectric transmitter.

### 4. Conclusions

In this work, we have proposed and demonstrated a simple and reliable instrument that can be used for characterization of acoustic sources such as loudspeakers. The measurement principle based on the optical feedback in a laser diode allows for a nonintrusive measurement of acoustic radiation patterns with a very simple arrangement. In particular, no vibration controlled is required

and all measurements have been performed on standard boards. Experimental results have been obtained with a piezoelectric transducer but the system can easily be extended to any type of acoustic source over a large frequency range only constrained by the electronic bandwidth.

**Acknowledgments:** This work was supported by the Instituto de Fomento al Talento Humano of the Ecuadorian Government.

**Conflicts of Interest:** The authors declare no conflict of interest.

## References

1. Bertling, K.; Perchoux, J.; Taimre, T.; Malkin, R.; Robert, D.; Rakić, A.D.; Bosch, T. Imaging of acoustic fields using optical feedback interferometry. *Opt. Express* **2014**, *22*, 30346–30356.
2. Taimre, T.; Nikolić, M.; Bertling, K.; Lim, Y.L.; Bosch, T.; Rakić, A.D. Laser feedback interferometry: a tutorial on the self-mixing effect for coherent sensing. *Adv. Opt. Photonics* **2015**, *7*, 570–631.
3. Malkin, R.; Todd, T.; Robert, D. A simple method for quantitative imaging of 2D acoustic fields using refracto-vibrometry. *J. Sound Vib.* **2014**, *333*, 4473–4482.
4. Nakamura, K.; Hirayama, M.; Ueha, S. Measurements of air-borne ultrasound by detecting the modulation in optical refractive index of air. In Proceedings of the 2002 IEEE Ultrasonics Symposium, Munich, Germany, 8–11 October 2002; Volume 1, pp. 609–612.
5. Hargather, M.J.; Settles, G.S.; Madalis, M.J. Schlieren imaging of loud sounds and weak shock waves in air near the limit of visibility. *Shock Waves* **2010**, *20*, 9–17.



© 2017 by the authors. Licensee MDPI, Basel, Switzerland. This article is an open access article distributed under the terms and conditions of the Creative Commons Attribution (CC BY) license (<http://creativecommons.org/licenses/by/4.0/>).

# Optical Engineering

OpticalEngineering.SPIEDigitalLibrary.org

## Visualization of an acoustic stationary wave by optical feedback interferometry

Patricio Fernando Urgiles Ortiz  
Julien Perchoux  
Antonio Luna Arriaga  
Francis Jayat  
Thierry Bosch

**SPIE**

Patricio Fernando Urgiles Ortiz, Julien Perchoux, Antonio Luna Arriaga, Francis Jayat, Thierry Bosch, "Visualization of an acoustic stationary wave by optical feedback interferometry," *Opt. Eng.* **57**(5), 051502 (2018), doi: 10.1117/1.OE.57.5.051502.

# Visualization of an acoustic stationary wave by optical feedback interferometry

Patricio Fernando Urgiles Ortiz,<sup>a,b</sup> Julien Perchoux,<sup>a</sup> Antonio Luna Arriaga,<sup>a</sup> Francis Jayat,<sup>a</sup> and Thierry Bosch<sup>a</sup>

<sup>a</sup>Université de Toulouse, LAAS-CNRS, CNRS, INPT, Toulouse, France

<sup>b</sup>Universidad Politécnica Salesiana, Cuenca, Ecuador

**Abstract.** This paper presents an experimental technique for two-dimensional imaging of dynamic acoustic pressure changes that is applied to visualize a stationary acoustic wave. This technique uses the optical feedback interferometry sensing scheme with a near-infrared laser diode and a two-axis scanning system. The stationary acoustic wave is generated by using a 40 kHz piezoelectric transducer pointing toward a concave acoustic reflector. The acoustic pressure dynamic changes are measured due to its impact on the propagating medium refractive index, which variation is integrated along the laser optical path from the laser diode to a distant mirror and back. The imaging system records a  $100 \times 50$  pixels image of the acoustic pressure in 66 min. © 2018 Society of Photo-Optical Instrumentation Engineers (SPIE) [DOI: [10.1117/1.OE.57.5.051502](https://doi.org/10.1117/1.OE.57.5.051502)]

Keywords: acoustic imaging; optical feedback interferometry; acousto-optic sensing.

Paper 171932SS received Dec. 6, 2017; accepted for publication Jan. 16, 2018; published online Feb. 7, 2018.

## 1 Introduction

The visualization of sound propagation has been a great challenge for researchers in recent years, leading to the development of new systems to measure and reconstruct images of acoustic pressure waves. The tools that are normally used to detect and measure the acoustic field are microphones that have a high sensitivity but need to be inserted inside the acoustic field, which causes alterations in the measurements of complex fields and in the case of imaging an acoustic wave requires a matrix of several microphones.<sup>1</sup> The detection of acoustic waves can be carried out by optical methods<sup>2-4</sup> and particularly using interferometry-based solutions without disturbing the pressure field. The weak changes of the refractive index in the transparent medium where the light propagates produce a modulation of the optical path along the trajectory of the laser beam. The phase shift induced by this modulation, which can be measured using interferometers,<sup>5-7</sup> represents the integration of pressure changes over the laser trajectory.

However, the laser beam being of very small dimension with regards to the laser wavelength, producing an image of the acoustic waves requires to perform a raster scan so that the measurement at each position represent a pixel of the reconstructed image. While using traditional interferometric methods such as laser Doppler velocimetry,<sup>8</sup> bulkiness of the optical systems and sensitivity to mechanical perturbations drastically limits the range of operation.

The method presented in this paper is based on optical feedback interferometry (OFI), which is based on the beating effect between the emitted and the backreflected wave from a distant reflector. OFI systems have previously been used to detect sound waves by monitoring the vibration of an exposed membrane<sup>9</sup> and recently by sensing the acousto-optic effect.<sup>10</sup> In this seminal work, Bertling et al. have demonstrated the possibility for OFI sensors to image acoustic

waves propagating in free-space. In this work, we apply a similar method for the imaging of a stationary wave generated by coupling the acoustic source to a concave acoustic reflector.

## 2 Principle of Operation

An interferometric modulation of the laser power is generated when a phase-shifted portion of the laser beam is retro injected into the cavity from which it was originally emitted.<sup>11</sup> While re-entering the laser cavity, the electric field of the backscattered light interferes with the laser cavity inner field, which affects its phase and amplitude. The latest directly impacts the laser power emission, where variations are measured by the laser in-package monitoring photodiode. The laser power fluctuations therefore provide an image of the information on the optical path variations that have followed the returning photons.

When applying OFI to the measurement of acoustic fields, one measures the changes in the optical path between the laser source and a distant mirror (as shown in Fig. 1) that are due to the modulation of the refractive index induced by the pressure wave. Solving the laser rate equations under feedback conditions leads to the following expression of the laser emitted power  $P_F$ :<sup>12</sup>

$$P_F = P_0[1 + m \cos(\omega_F \tau)], \quad (1)$$

where  $P_0$  is the laser power without optical feedback,  $m$  is a modulation index that depends mainly on the reflectivity of the mirror,  $\omega_F$  is the angular frequency of the laser electric field, and  $\tau$  is the round-trip time of photons in the external cavity. In the case of pressure induced variation of the round-trip time  $\tau$ , this one can be described by  $\tau = \tau_0 + \delta\tau$  where  $\tau_0$  is the round-trip time in absence of pressure change and  $\delta\tau$  is the variation due to the pressure-induced compression of the medium.<sup>13</sup>

\*Address all correspondence to: Julien Perchoux, E-mail: [julien.perchoux@laas.fr](mailto:julien.perchoux@laas.fr)

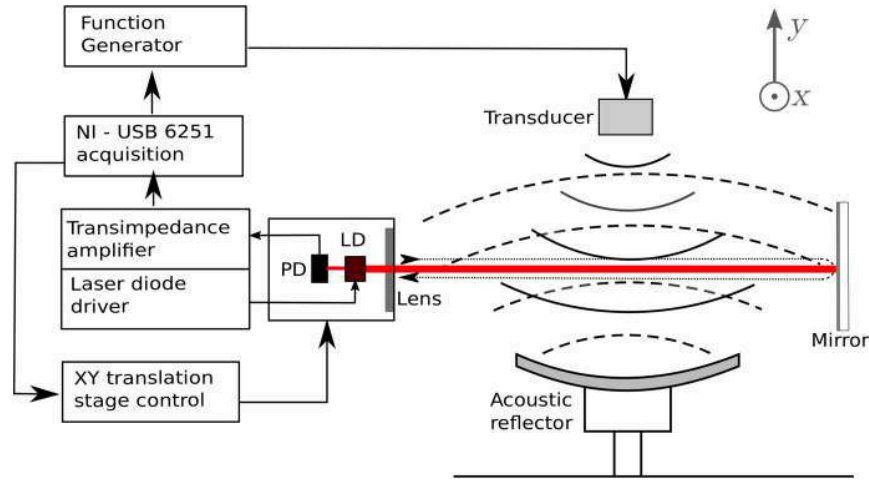


**Fig. 1** Schematic of the imager setup. The incident acoustic wave is represented in concentric solid line arcs, while the reflected acoustic is represented as dashed line arcs. LD and PD stand for laser diode and photodiode, respectively.

$$\delta\tau = \int_0^L \frac{2\delta n(z)}{c} dz, \tag{2}$$

where  $\delta n$  is the refractive index change over the external cavity length  $L$  and  $c$  is the speed of light in vacuum.

Thus, with this technique, the acoustic pressure variations over an integration line are measured. In order to produce an image of the acoustic wave, it is required to move the sensor in each pixel position and to synchronize the signal acquisition in each position with the acoustic source excitation signal.

### 3 Experimental Setup

The optical feedback interferometer consists of a distributed feedback laser diode L1320P5DFB with a transverse and longitudinal single-mode emission at 1310 nm. The laser is beaming onto an aluminium coated mirror of diameter 25.4 mm through a collimating lens (Thorlabs C240TME-C). The external cavity length  $L$  between the laser and mirror is set to 200 mm and both are mounted on U-shaped rigid holder so that the optical path is not affected by any other perturbation than the acoustic wave propagation while performing the scan. The OFI set is associated to a translation system with two motorized linear stage of 100 mm travel range for the  $X$  axis and 50 mm travel range for the  $Y$  axis.

The acoustic source is an ultrasonic piezoelectric transmitter KPUS-40T-16T-K768 driven by a sinusoidal voltage of 10-V peak-to-peak amplitude at 40 kHz. Under these conditions, 30 cm away from the transducer, the acoustic pressure is expected to reach 117 dB. It is displayed (see Fig. 1) so that the propagation axis is perpendicular to the optical propagation direction and facing a parabolic reflector of 110 mm diameter leading to a focal distance of 40 mm. The distance between the transducer and the reflector is 60 mm in order to obtain the stationary wave.

The amplitude of the signal variations is acquired through the in-package monitoring photodiode of the laser, where current is amplified by a custom-made transimpedance amplifier then fed into a National Instrument acquisition card (NI-USB-6251) with a sampling frequency of 1 MHz. A Labview program controls the position of the linear

translation stages in both axes ( $x, y$ ), and at each pixel the photodiode amplified current is acquired as shown in Fig. 2 in the case of pixel (60,45), by windows of 1000 samples length. The acquisition of the signal at each pixel takes about 0.8 s, and a time budget of  $Y$  s is allowed for the displacement of the sensor and mechanical stabilization, all together leading to a global time of 66 min to perform the full image.

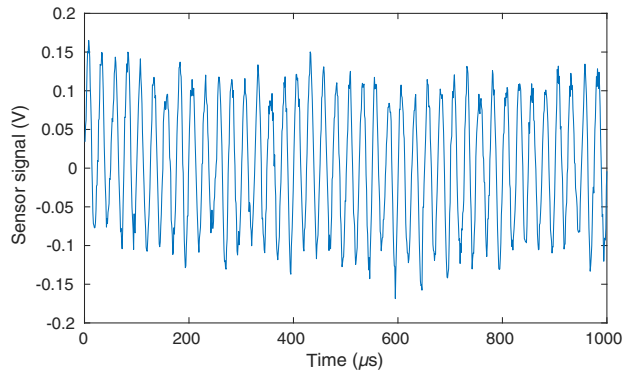


**Fig. 2** Time-domain sensor signal acquisition for pixel (60,45).

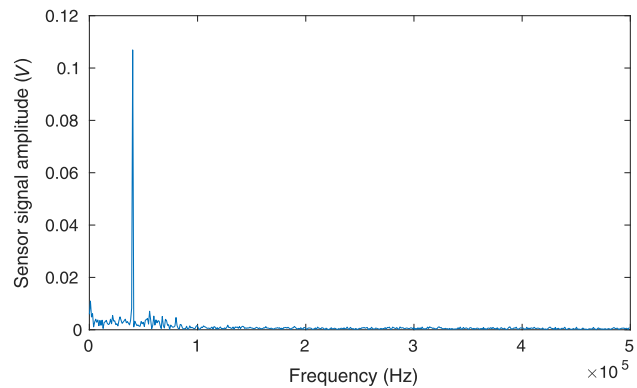


**Fig. 3** Fast Fourier transform of the signal plotted in Fig. 2 corresponding to pixel (60,45).

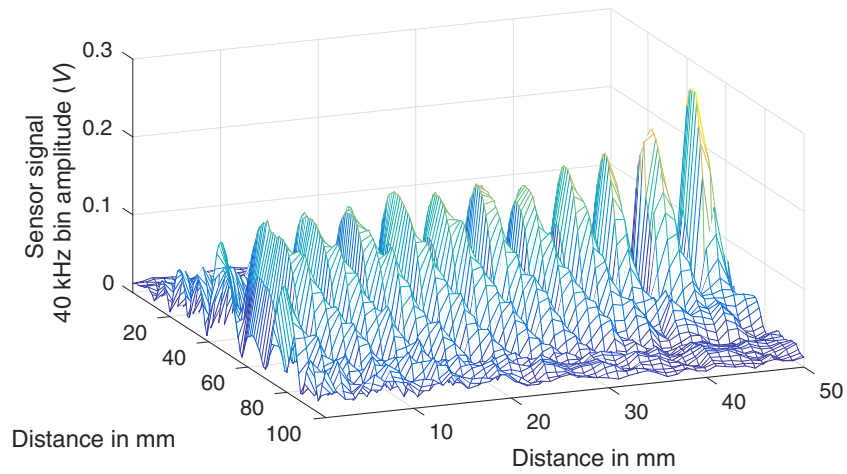


**Fig. 4** 100 × 50 pixels image of the stationary pressure wave reconstructed from the 40 kHz peak of the sensor signal spectrum at each pixel.

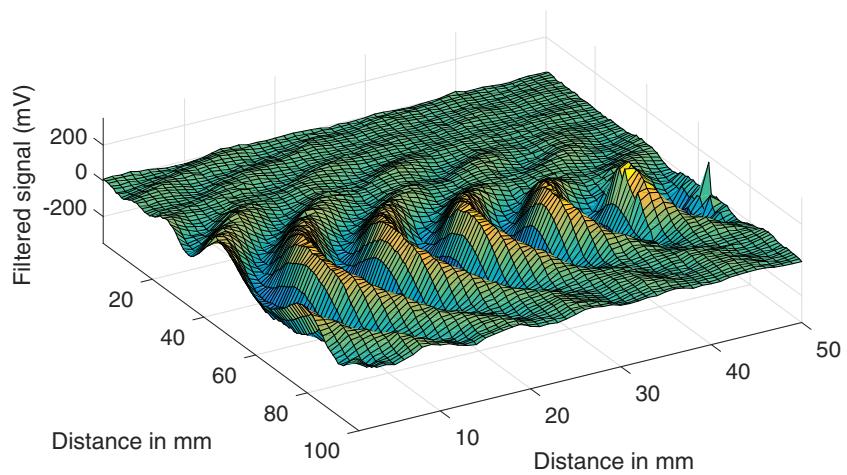


**Fig. 5** 100 × 50 pixels instantaneous image of the stationary pressure wave after band-pass filtering of signals. Still image from Video [\[1\]](http://dx.doi.org/10.1117/1.OE.57.5.051504) (MP4, 5.8 MB [URL: <http://dx.doi.org/10.1117/1.OE.57.5.051504>]).

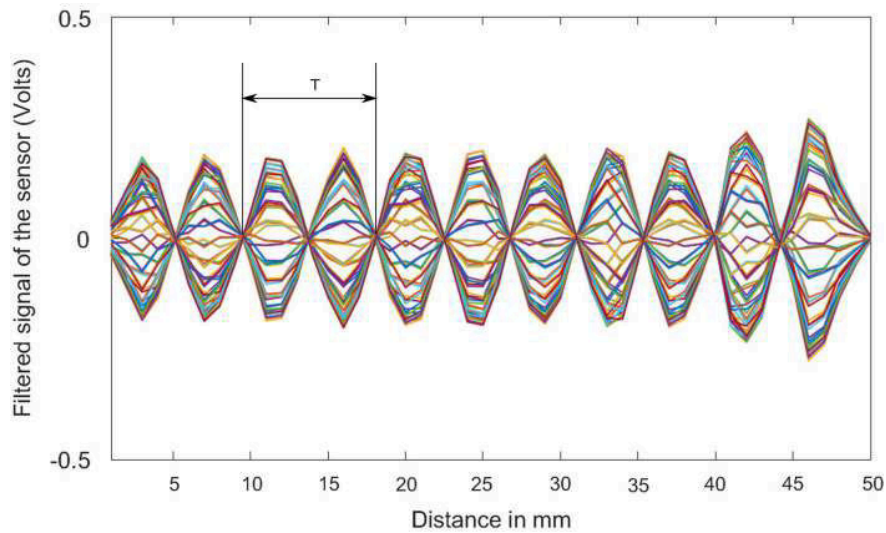


**Fig. 6** Acoustic propagation axis stored time-domain signals showing nodes and antinodes of the pressure wave.

## 4 Results and Discussion

Figures 2 and 3 show the sensor signal and its fast Fourier transform (FFT), respectively, for a given  $(x, y)$  position. In Fig. 3, the 40-kHz peak amplitude has been demonstrated to be proportional to the acoustic field pressure.<sup>14</sup>

While saving the amplitude information of the FFT signal at 40 kHz in each  $(x, y)$  position, the image of the acoustic pressure distribution in  $(x, y)$  plane is reconstructed, showing a very clear behavior of a stationary wave. Figure 4 shows this image in the case of a  $100 \times 50$  mm with a resolution 1 mm.

In addition, the image of the stationary wave can be plotted using the instantaneous amplitude of the signal. In order to improve the image quality, we applied a digital filter pass-band Butterworth two-order with central frequency 40 kHz and band-pass from 38 to 42 kHz to each acquired signal. Figure 5 shows such a reconstructed image, and media 1 presents the evolution in time of this acoustic wave representation.

In order to clearly appreciate the position of the nodes and antinodes of the stationary wave, we have acquired and stored the time domain variations of the sensor signal over the 50 positions along the acoustic propagation axis. Figure 6 shows the sensor signals along the  $x$ -axis at  $y = 60$  mm at 50 consecutive acquisition over a generator signal period. In this image, where the transducer location corresponds to the 50 abscissa, it is possible to observe the acoustic wavelength of 8 mm that corresponds to the frequency of 40 kHz in the air.

## 5 Conclusion

Due to the use of an imaging system based on OFI, we demonstrated the visualization of pressure variations of an acoustic stationary wave produced by the reflection of the emitted wave by a concave reflector. The image that was produced has a resolution of 1 mm and it allows clear observation of the nodes and antinodes positions. Further extensions of this work consist of observing acoustic wave shaping as, for example, focalization by means of acoustic reflectors and improving the acquisition time of the imager with the objective to obtain the image in less than 66 min.

## Acknowledgments

This work was supported by the Instituto de Fomento al Talento Humano of the Ecuadorian Government.

## References

1. S. Siltanen et al., "Acoustic visualizations using surface mapping," *J. Acoust. Soc. Am.* **135**(6), EL344–EL349 (2014).
2. K. Hall, "Observing ultrasonic wave propagation by stroboscopic visualization methods," *Ultrasonics* **20**(4), 159–167 (1982).
3. D. F. Comesaña et al., "Scan and paint: theory and practice of a sound field visualization method," *SRN Mech. Eng.* **2013**, 1–11 (2013).
4. N. Chitanont et al., "Visualization of sound field by means of Schlieren method with spatio-temporal filtering," in *IEEE Int. Conf. on Acoustics, Speech and Signal Processing (ICASSP)*, pp. 509–513, IEEE (2015).
5. R. Malkin, T. Todd, and D. Robert, "A simple method for quantitative imaging of 2D acoustic fields using refracto-vibrometry," *J. Sound Vib.* **333**(19), 4473–4482 (2014).

6. Y. Oikawa et al., "Sound field measurements based on reconstruction from laser projections," in *IEEE Int. Conf. on Acoustics, Speech, and Signal Processing, Proc. (ICASSP)*, Vol. 4, pp. iv/661–iv/664, IEEE (2005).
7. K. Ishikawa et al., "High-speed imaging of sound using parallel phase-shifting interferometry," *Opt. Express* **24**(12), 12922–12932 (2016).
8. L. Zipser et al., "Reconstructing two-dimensional acoustic object fields by use of digital phase conjugation of scanning laser vibrometry recordings," *Appl. Opt.* **42**(29), 5831–5838 (2003).
9. E. Olsson et al., "Scattered ultrasound fields measured by scanning laser vibrometry," *Proc. SPIE* **5144**, 717–727 (2003).
10. Y. Oikawa et al., "Visualization of sound field and sound source vibration using laser measurement method," in *Proc. Int. Congress Acoustics (ICA)*, p. 898 (2010).
11. K. Bertling et al., "Imaging of acoustic fields using optical feedback interferometry," *Opt. Express* **22**(24), 30346–30356 (2014).
12. G. Giuliani et al., "Laser diode self-mixing technique for sensing applications," *J. Opt. A* **4**, S283–S294 (2002).
13. T. Bosch et al., "Optical feedback interferometry," in *Encyclopedia of Sensors*, C. A. Grimes, E. C. Dickey, and M. V. Pishko, Eds., Vol. X, pp. 1–20, American Scientific Publishers, Valencia, California (2005).
14. F. Urgiles, J. Perchoux, and T. Bosch, "Characterization of acoustic sources by optical feedback interferometry," *Proceedings* **1**(4), 348 (2017).

**Patricio Fernando Urgiles Ortiz** completed his secondary studies in the Salesian Technical Superior Institute. He graduated from the Universidad Politecnica Salesiana as an electronics engineer in 2003. He received his specialist degree in the university teaching in 2005 from the Universidad del Azuay, in 2012, he received his master's degree in electronic engineering from Pontificia Universidad Javeriana in Bogota Colombia. He is currently studying in the third year of the doctoral program at the Institut National Polytechnique de Toulouse on the topic of acoustic images by optical feedback interferometry.

**Julien Perchoux** received his BSc degree in applied physics from the University of Montpellier, France, in 1999, his MSc and PhD degrees in microwave and photonics from the University of Toulouse, ISAE, in 2002 and 2005, respectively. He graduated from the École Normale Supérieure, Cachan, France, in 2001. He is with the Optoelectronics for Embedded System (OSE) team of the LAAS-CNRS (Toulouse, France) as an associate professor since 2005. His current research interests include semiconductor laser physics, biomedical imaging, flowmetry, acoustic imaging, and design of embedded sensing systems.

**Antonio Luna Arriaga** received his MS degree in instrumentation from the INSA-Lyon, France, in 2007. He completed his doctoral studies with the Group of Optoelectronics for Embedded Systems (LAAS-CNRS), INP-Toulouse, France, in 2014. His current research focuses on real-time signal processing and architectures to enable the development of smart sensing devices.

**Francis Jayat** studied at the University of Limoges and the Xlim Laboratory in Electronics Microwaves Optics and Photonics. He is currently with the group of OSE of the LAAS-CNRS as an engineer dedicated to system automation and signal acquisition for optical sensors.

**Thierry Bosch** is currently a full professor at Toulouse INP, and he is leading the group of OSE of the LAAS-CNRS. His scientific interests are related to laser industrial instrumentation development. He has coauthored around 50 papers in archival journals, and he has been invited to author the chapter dedicated to self-mixing sensors published in the Encyclopedia of Sensors. He has been guest coeditor for several peer reviewed journals on *Laser Sensors for Displacement, Distance, Flow, Velocity, and Vibrations Measurements*.

# Optical Feedback Interferometry Applied to Visualize an Acoustic Stationary Wave

Fernando Urgiles<sup>a,b</sup>, Julien Perchoux<sup>a</sup>, Francis Jayat<sup>a</sup>, Clement Tronche<sup>a</sup>, and Thierry Bosch<sup>a</sup>

<sup>a</sup>LAAS-CNRS, Universit de Toulouse, CNRS, INPT, Toulouse, France

<sup>b</sup>Universidad Politecnica Salesiana Cuenca, Ecuador

## ABSTRACT

This article presents a novel technique to acquire and visualize two-dimensional images of dynamic changes of acoustic pressure in the case of a stationary acoustic wave. This method uses optical feedback interferometry sensing with a near-infrared laser diode. The stationary acoustic wave is generated using two piezoelectric transducers of 40 kHz facing each other, dynamic changes in acoustic pressure are measured in a 100 mm × 100 mm acoustic propagation field whose refractive index is variable along the optical path of the laser from the laser diode to a distant mirror and vice-versa. The image system records an image of 100 × 100 pixels of the acoustic pressure variation.

**Keywords:** Acoustic imaging, Optical Feedback Interferometry, Acousto-Optic sensing

## 1. INTRODUCTION

A great challenge in recent years has been the visualization of sound propagation<sup>1</sup> leading to the development of new systems to measure and reconstruct images of acoustic pressure waves. For measuring the acoustic field in air, microphones are commonly used as sensors<sup>2,3</sup>. They have a high sensitivity but the microphone's body need to be inserted into the field which causes extra reflection and diffraction. The measured quantity is contaminated by the microphone itself. Furthermore a matrix of several microphones is required when imaging an acoustic wave. The detection of acoustic waves can be carried out by optical methods.<sup>4</sup> Since light does not affect the behavior of sound, then interferometry-based device is a solution for detecting the pressure field without altering it<sup>5,6</sup>. Therefore, the measurement error caused by the existence of equipments inside the field can be avoided. The non-contact method permits to observe sound fields where microphones cannot be applied. The variation of the refractive index<sup>7</sup> in the transparent medium where light propagates produces variations in the speed of light along the trajectory of the laser beam. The phase shift induced by this modulation can be measured by using interferometers.

Since the laser wavelength is very small compared to acoustic wavelength, a raster scan is required to produce an image of the acoustic waves. The measurement at each position represents a pixel in the reconstructed image. While using traditional interferometric methods such as Laser Doppler velocimetry (LDV), bulkiness of the optical systems and sensitivity to mechanical perturbations drastically limits the domains of operation.<sup>8</sup>

The method presented in this paper is based on optical feedback interferometry (OFI)<sup>10,11,12,13,14</sup> which has previously been used to detect sound waves by monitoring the vibration of an exposed membrane and recently by sensing the acousto-optic effect.<sup>9</sup> Bertling<sup>15</sup> has exhibited the likelihood for OFI sensors to picture acoustic waves engendering in free-space. In the present work, we apply a comparable technique for the imaging of a stationary wave<sup>16,17</sup> produced by coupling the two acoustic source in opposite<sup>18,19</sup>. A standing wave is a stationary pattern produced by the interference of waves bouncing back and forth in a confined space. Waves moving down and up form an interference pattern that can be constructive or destructive. When the interference is constructive, we can hear a significant increase in sound volume. This increase in the amplitude of the sound is called resonance.

## 2. PRINCIPLE OF OPERATION

An interferometric modulation of the laser power is generated when a phase-shifted portion of the laser beam is retro-injected into the cavity from which it was originally emitted after reflection or retro-diffusion from a distant object<sup>12</sup> While re-entering the laser cavity, the electric field of the backscattered light interferes with the laser cavity inner field, and thus affects its phase and amplitude. The latest directly impacts the laser power emission, where variations are measured by the laser in-package monitoring photodiode. The laser power fluctuations therefore provide an image of the information on the optical path variations that have followed the returning photons.

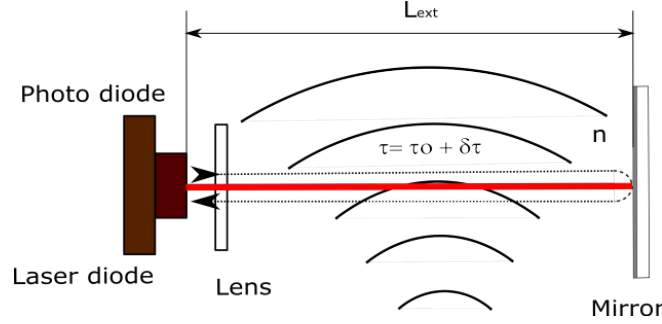


Figure 1. Set-up optical feedback interferometry.

When applying OFI to the measurement of acoustic fields, the changes in the optical path between the laser and a distant mirror (as shown in Fig. 1) are due to the modulation of the refractive index induced by the pressure wave. Solving the laser rate equations under feedback conditions leads to the following expression of the laser emitted  $P_F$ :<sup>20</sup>

$$P_F = P_0[1 + m \cos(\omega_F \tau)] \quad (1)$$

where  $P_0$  is the laser power without optical feedback,  $m$  is the modulation index that depends mainly on the reflectivity of the mirror,  $\omega_F$  is the angular frequency of the lasers electric field, and  $\tau$  is the round-trip time of photons in the external cavity.

The pressure induced variations of the roundtrip time  $\tau$ , can be described by  $\tau = \tau_0 + \delta\tau$  where  $\tau_0$  is the round-trip time in absence of pressure change and  $\delta\tau$  is the variation due to the compression of the medium and can be explicated as

$$\delta\tau = \int_0^{L_{ext}} \frac{2\delta n(z)}{c} \quad (2)$$

where  $\delta n$  is the variation of refractive index,  $L_{ext}$  is the external cavity length, and  $c$  represents the speed of light in vacuum.

With this technique, the acoustic pressure variations along an integration line are measured in one point in the acoustic field. In order to produce an image of the interferences of two acoustic waves, it is required to move the sensor in each pixel position and to synchronize the signal acquisition in each position with the acoustic source excitation signal.

## 3. EXPERIMENTAL SETUP

The optical feedback interferometer consists in a laser diode L1320P5DFB with a transverse and longitudinal single-mode emission at 1310 nm. The external cavity length  $L_{ext}$  between the laser and mirror is set to 200 mm and both are mounted on U-shaped rigid holder so that the optical path is not affected by any other perturbations than the acoustic wave propagation while performing the scan. The laser beam is reflected by a

25.4 mm diameter aluminium coated mirror through a collimation lens (Thorlabs C240TME-C). The OFI set is associated to a translation system with two motorized linear stages of 100 mm travel range for the X axis and 50 mm travel range for the Y axis. The acoustic source is two ultrasonic piezoelectric transmitters KPUS-40T-16T-K768 driven by a sinusoidal voltage of 10 V peak-to-peak amplitude at 40 kHz. Under these conditions, the propagation axis is perpendicular to the optical propagation direction as shown in Fig. 2.

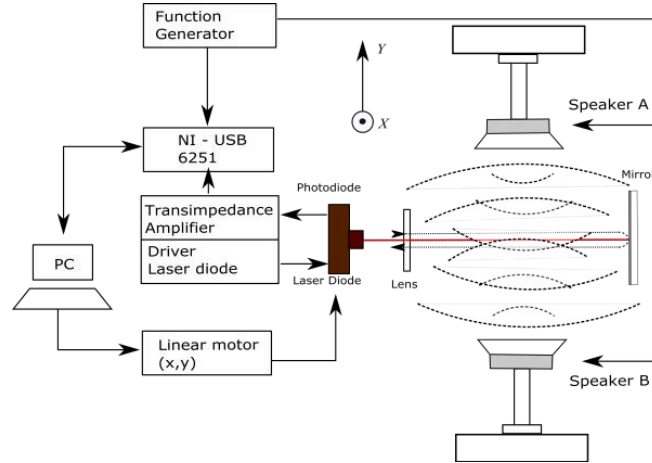
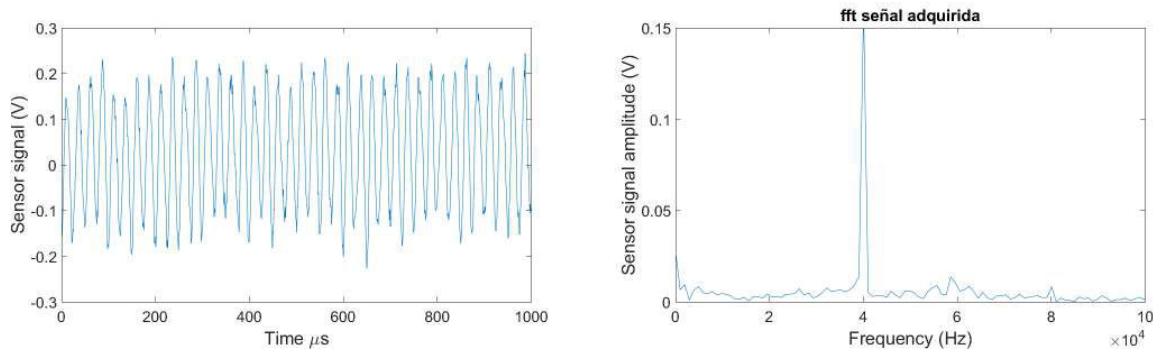


Figure 2. Schematic of the OFI set-up.

The variations in the signal are acquired through the monitoring photodiode integrated in the laser package, where the current is amplified by a custom made transimpedance amplifier and then the signal is digitized by an acquisition card (NI- USB-6251) with a sample rate of 1 MHz. This reading is done through a dedicated Labview program which also controls the linear motors for the displacement of both axes (x,y). At each pixel, 1000 samples of the photodiode amplified current are acquired as shown in Fig.3(a) for the pixel (30,5). The acquisition of the signal for each pixel takes approximately 0.4 s. A Fast Fourier Transform is then applied on this signal in order to achieve a considerable magnitude at the frequency of stimulation of the piezoelectric device.



(a) Time-domain sensor signal acquisition for pixel(35,35) (b) Fast Fourier transform of the signal plotted to pixel (35,35).

Figure 3. Signal sensor in time domain and frequency

To improve the signal it is necessary to implement a Band-Pass filter Butterworth which central frequency is 40 kHz with a windows equal a 4 kHz, with a time of response of the filter of 250  $\mu$ s to obtain the next signal.

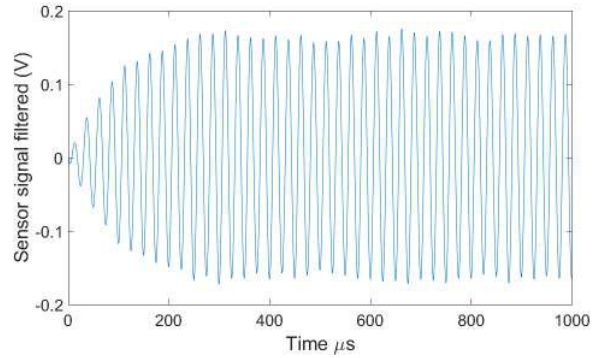


Figure 4. Time-domain sensor signal after Band-pass filtering of signal for pixel(35,35).

#### 4. RESULT AND DISCUSSION

The procedure for scanning the area is obtained by moving the system as a grid of 100 points for 100 points with a separation 1 mm between 2 pixels. With the values of each pixel at the same time, we can observe an image in the time domain of the behavior of the acoustic pressure. However, the image is noisy.

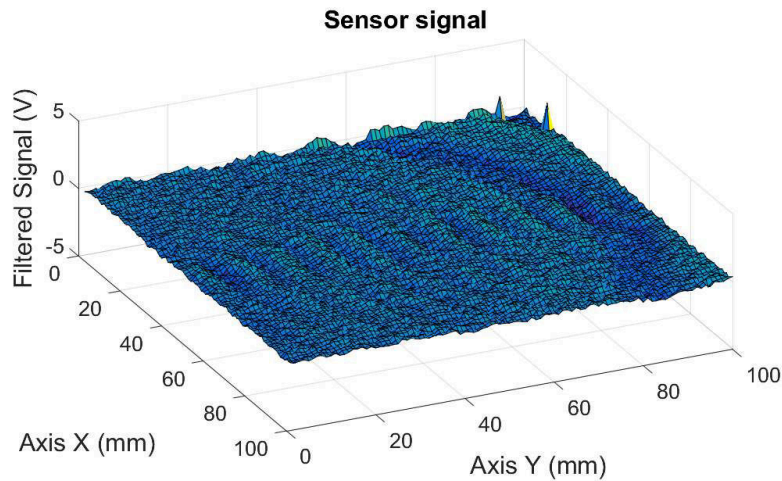


Figure 5. 100x100 pixels instantaneous image of standing pressure wave from the sensor signal.

The Butterworth digital Band-Pass filter is then implemented (Fig. 5) in order to obtain a smoother image. The standing waveform due to both speakers in the time domain can then be observed. By considering that the length of sound wave at 40 kHz is 8.5 mm and the scan length is 100 mm, we get the length approximately to 11 acoustic wavelengths.

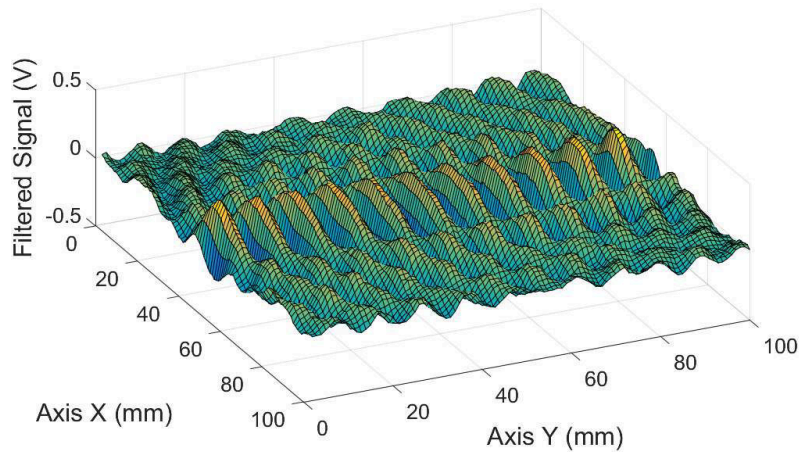


Figure 6. 100x100 pixels instantaneous image of standing pressure wave after band-pass filtering of signal.

In Fig. 7, we can observe the evolution in time of this acoustic wave along the Y axis and the position 50 in X axis of the sensor signal in different time in order to clearly appreciate the position of the nodes and antinodes of the stationary wave. Thus it is possible to appreciate the standing wave along of Y axis.

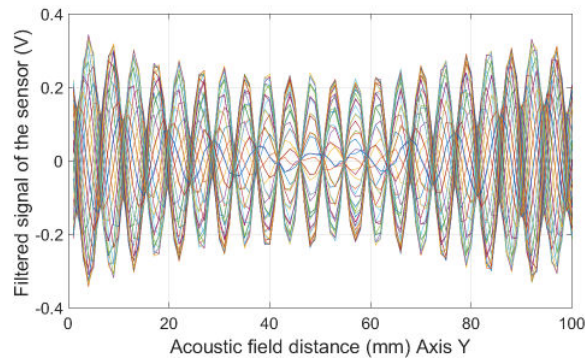


Figure 7. Acoustic propagation axis stored time-domain signals showing nodes and anti-nodes of the pressure wave.

A Fast Fourier Transform (FFT) of the sensor signal is computed for a given position (35, 35) and plotted in Fig. 3(b). The 40 kHz peak has been demonstrated to be proportional to the acoustic field pressure.<sup>19</sup>

The amplitude of the FFT signal at 40 kHz in each position (x,y) is recorded and plotted to obtain the image of the acoustic pressure distribution in the (x,y) plane, and thus it shows the behavior of the acoustic field of the standing wave due to the interaction of two acoustic sources in space. Fig. 8(b) shows the image with a size of 100 mm 100 mm and a resolution of 1 mm.

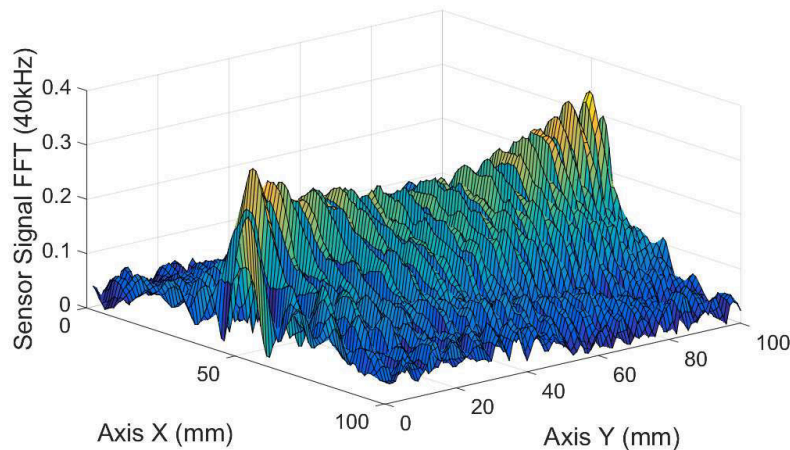


Figure 8. Acoustic pressure wave by FFT signal

## 5. CONCLUSION

With the imaging system based on Optical Feedback Interferometry, we visualize of acoustic pressure variations in time domain and in FFT of a standing wave produced by two opposite acoustic wave sources. The image obtained sizes 100 X 100 pixel with a resolution of 1 mm, allows us to observe in the time domain the nodes and anti-nodes positions along the Y axis. The acquisition time has been improved, obtaining a bigger image comparing to the previous works in just 66 minutes. The developed setup has great expectations for analysis in different fields of the industry.

## ACKNOWLEDGMENTS

This work was supported by the Instituto de Fomento al Talento Humano of the Ecuadorian Government.

## REFERENCES

- [1] Chitanont, N., Yatabe, K., Ishikawa, K., and Oikawa, Y., "Spatio-temporal filter bank for visualizing audible sound field by schlieren method," *Applied Acoustics* **115**, 109 – 120 (2017).
- [2] Koyano, Y., Yatabe, K., and Oikawa, Y., "Infinite-dimensional svd for revealing microphone arrays characteristics," *Applied Acoustics* **129**, 116 – 125 (2018).
- [3] Herold, G. and Sarradj, E., "Performance analysis of microphone array methods," *Journal of Sound and Vibration* **401**, 152 – 168 (2017).
- [4] Yatabe, K., Ishikawa, K., and Oikawa, Y., "Acousto-optic back-projection: Physical-model-based sound field reconstruction from optical projections," *Journal of Sound and Vibration* **394**, 171 – 184 (2017).
- [5] Oikawa, Y., Yatabe, K., Ishikawa, K., and Ikeda, Y., "Optical sound field measurement and imaging using laser and high-speed camera," in [*Proceedings of the INTER-NOISE 2016 - 45th International Congress and Exposition on Noise Control Engineering: Towards a Quieter Future*], 258–266, German Acoustical Society (DEGA) (8 2016).
- [6] Zipser, L., Franke, H., Olsson, E., Molin, N.-E., and Sjdahl, M., "Reconstructing two-dimensional acoustic object fields by use of digital phase conjugation of scanning laser vibrometry recordings," *Applied optics* **42**, 58315838 (October 2003).
- [7] Jones, F. E., "Simplified equation for calculating the refractivity of air," *Appl. Opt.* **19**, 4129–4130 (Dec 1980).
- [8] Malkin, R., Todd, T., and Robert, D., "A simple method for quantitative imaging of 2d acoustic fields using refracto-vibrometry," *Journal of Sound Vibration* **333**, 4473–4482 (Sept. 2014).

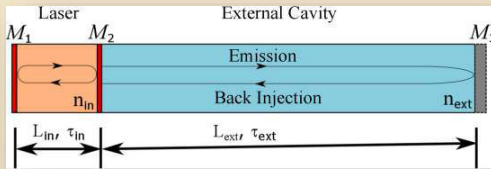
- [9] Nakamura, K., “Sound field measurement through the acousto-optic effect of air by using laser doppler velocimeter,” in [*Technical Digest. CLEO/Pacific Rim 2001. 4th Pacific Rim Conference on Lasers and Electro-Optics (Cat. No.01TH8557)*], **1**, I–I (July 2001).
- [10] Tromborg, B., Osmundsen, J., and Olesen, H., “Stability analysis for a semiconductor laser in an external cavity,” *IEEE Journal of Quantum Electronics* **20**, 1023–1032 (Sep 1984).
- [11] Taimre, T., Nikolić, M., Bertling, K., Lim, Y. L., Bosch, T., and Rakić, A. D., “Laser feedback interferometry: a tutorial on the self-mixing effect for coherent sensing,” *Adv. Opt. Photon.* **7**, 570–631 (Sep 2015).
- [12] Giuliani, G., Norgia, M., Donati, S., and Bosch, T., “Laser diode self-mixing technique for sensing applications,” *Journal of Optics A: Pure and Applied Optics* **4**(6), S283 (2002).
- [13] Donati, S., Giuliani, G., and Merlo, S., “Laser diode feedback interferometer for measurement of displacements without ambiguity,” *IEEE Journal of Quantum Electronics* **31**, 113–119 (Jan 1995).
- [14] Agrawal, G., “Line narrowing in a single-mode injection laser due to external optical feedback,” *IEEE Journal of Quantum Electronics* **20**, 468–471 (May 1984).
- [15] Bertling, K., Perchoux, J., Taimre, T., Malkin, R., Robert, D., Rakić, A. D., and Bosch, T., “Imaging of acoustic fields using optical feedback interferometry,” *Opt. Express* **22**, 30346–30356 (Dec 2014).
- [16] Siddiqui, K. and Nabavi, M., “Measurement of the acoustic velocity characteristics in a standing-wave tube using out of phase piv,” *Flow Measurement and Instrumentation* **19**(6), 364 – 369 (2008).
- [17] Ellier, E. S., Kdous, W., Bailly, Y., Girardot, L., Ramel, D., and Nika, P., “Acoustic streaming measurements in standing wave resonator using particle image velocimetry,” *Wave Motion* **51**(8), 1288 – 1297 (2014).
- [18] Urgiles, F., Perchoux, J., and Bosch, T., “Characterization of acoustic sources by optical feedback interferometry,” *Proceedings* **1**(4) (2017).
- [19] Patricio Fernando Urgiles Ortiz, Julien Perchoux, A. L. A. F. J. T. B., “Visualization of an acoustic stationary wave by optical feedback interferometry,” *Optical Engineering* **57**, 57 – 57 – 4 (2018).
- [20] Taimre, T., Nikolić, M., Bertling, K., Lim, Y. L., Bosch, T., and Rakić, A. D., “Laser feedback interferometry: a tutorial on the self-mixing effect for coherent sensing,” *Adv. Opt. Photon.* **7**, 570–631 (Sep 2015).

## Abstract:

Sound as the propagation of pressure variations in compressible media involves compression and expansion and thus induces changes of the refractive index that can be measured by optical methods. The most recent proposed method is the optical feedback interferometry. With this technique, a laser diode is beaming on a reflective surface thus creating an optical cavity where the acoustic wave propagates. This paper presents a novel experimental technique to measure radiation pattern of acoustic sources based on optical feedback interferometry in a laser diode.

## Principle of the OFI sensing scheme

The coherent light that is generated inside the laser is emitted through the mirror  $M_2$ , is transmitted through an external cavity of physical length  $L_{ext}$  and refractive index  $n_{ext}$  to a distant mirror  $M_3$  and thus reflected and re-injected into the laser cavity.



Schematic of the OFI sensing scheme : laser cavity ( $M_1, M_2$ ), external cavity ( $M_2, M_3$ )

The reinjected light interferes with the laser cavity light and impacts the laser emitted power ( $P_F$ ) so that :

$$P_F = P_0 [1 + m \cos(\omega_F \tau_{ext})]$$

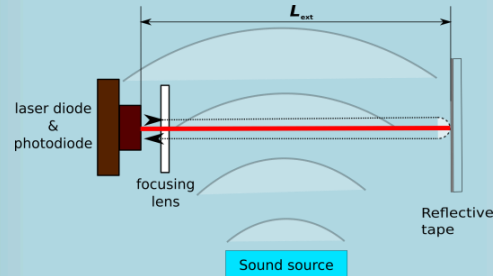
Where:

$P_0$  is the laser power without optical feedback,  
 $m$  is the modulation index (signal strength),  
 $\omega_F$  is the angular frequency of the laser electric field,  
 $\tau_{ext}$  is the round-trip time inside the external cavity.

## Application to acoustics

The acoustic wave propagates through the external cavity inducing modulations of :  
 the **local pressure**

- the refractive index
- the round-trip time  $\tau_{ext}$
- the **laser power**



Acoustic sensing scheme with OFI principle

The round-trip time of flight is  $\tau_{ext} = \tau_0 + \delta\tau$

$$\text{with } \delta\tau = \int_0^{L_{ext}} \frac{2\delta n(z)}{c} dz$$

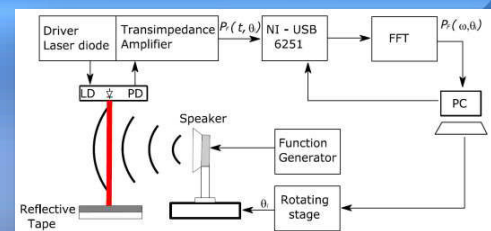
## Experimental setup

The **optical feedback interferometer** consists in a DFB laser diode (ML725B11F –  $\lambda=1310\text{nm}$ ) and a microsphere reflective tape glued on a solid metallic target located 200mm away from the laser.

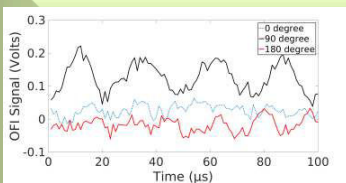
The **acoustic source** is a piezoelectric actuator (MA40B8S) driven by a sinusoidal signal at 40kHz that is mounted on a motor controlled rotating stage.

The distance between the laser beam and the actuator is 100mm.

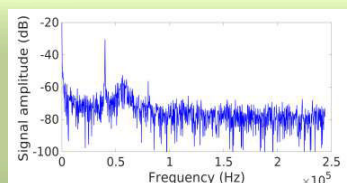
A Labview VI controls the acquisition and the position on the source.



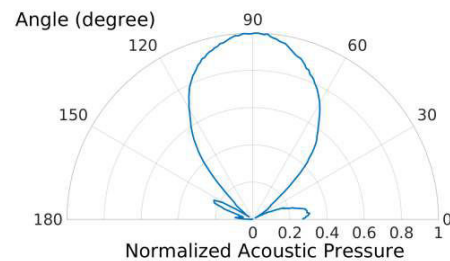
## Results



Time domain signal of the OFI sensor at 0, 90 and 180°



Frequency domain signal of the OFI sensor at 0°



Normalized radiation pattern of the MA40B8S piezoelectric actuator

**Acknowledgment:** This work has been supported by the Instituto de Fomento al Talento Humano of the Ecuadorian Government.

# LAURIERS DE L'INP

## Demande de brevet d'invention

Toulouse INP encourage la démarche de protection des inventions et félicite

Julien PERCHOUX

Fernando URGILES ORTIZ

### Pour la demande de brevet d'invention

Imageur 3D d'ondes de pression acoustique par un  
capteur interférométrique associé aux techniques de tomographie  
déposé le 24/11/2017 sous le n° FR 1761141

Déposants : Toulouse INP / CNRS

Fait à TOULOUSE, le 13 juin 2019

Professeur Olivier SIMONIN



LÉOPOLD ESCANDE

Président de Toulouse INP

